

PARTICLE SENSORS IN IONOSPHERIC PLASMA:
STUDY OF LANGMUIR PROBES WITH KINETIC
SIMULATIONS

BY

PEDRO ALBERTO RESENDIZ LIRA

A THESIS SUBMITTED IN PARTIAL FULFILLMENT OF THE REQUIREMENTS FOR
THE DEGREE OF

DOCTOR OF PHILOSOPHY

DEPARTMENT OF PHYSICS
UNIVERSITY OF ALBERTA

© PEDRO ALBERTO RESENDIZ LIRA, 2019

ABSTRACT

Particle collection by Swarm spherical probes, and front plate when used as a planar Langmuir probe, is studied for representative ionospheric plasma conditions. The objective is to assess uncertainties in the plasma parameters inferred from probe measurements using analytic models. Probe in situ measurements are generally interpreted in terms of plasma parameters on the basis of theoretical approaches. Swarm spherical probe measurements are interpreted in the Orbital Motion Limited (OML) approximation, while the front plate has assumed the following relation between the measured collected current I , e the elementary charge, the ion density n , the plasma flow velocity to the plate v_{ram} , and the known geometrical surface of the plate, $I = env_{ram}A_{geo}$. In such models, several assumptions or asymptotic limits are considered in order to obtain analytical solutions. Probe collected currents are calculated numerically and interpreted as in actual Swarm in situ measurements. Kinetic simulations are done while accounting for more physical effects than can be accounted for analytically. For the spherical probes, simulations also account for the main aspects of the probe geometry and its proximity to the Swarm bus. By comparing inferred parameters from simulated probe measurements with the known ones used as input in the simulations, it is possible to assess relative errors resulting from the use of analytic expressions. OML predictions of the electron temperature inferred from spherical probe measurements are found to be moderately accurate, with relative errors not exceeding 12%, when the satellite floating is moderate negative. As the spacecraft floating potential becomes more negative, more electron are repelled and the electron currents collected by the probes are reduced, impacting then the estimates of the inferred temperatures by up to 48%. The maximum errors are mainly

caused by the neglect of magnetic field and satellite sheath effects in the OML theory. The estimates of the plasma density on the other hand, are significantly less accurate, with relative errors up to 76%. Here, discrepancies are attributed mostly to the neglect of minority light ions, and the satellite electric sheath, which can extend to, and include the tip of the spherical Langmuir probes. Simulation results of the Swarm front plate led to the conclusion that the effective cross section A_{eff} is generally larger than the geometrical A_{geo} which is consistent with observations. The current collected by the plate is enhanced from 2.8 to 23.4% with respect to the one collected by the geometrical cross-section, where this enhancement is attributed to fringe effects. Simulation results from the front plate are used then to construct an empirical model for the collected current by the plate accounting for the enhancements, and in turn enable improvements in the accuracy of inferred plasma parameters.

PREFACE

Chapter 4 is based in part on an article published by Pedro Alberto Resendiz Lira, Richard Marchand, Johnathan Burchill, and Matthias Förster. “Determination of Swarm front plate’s effective cross section from kinetic simulations”. *IEEE Transactions on Plasma Science*, 2019. I was responsible for choosing the cases to simulate, for carrying out simulations, analyzing, and constructing empirical models to fit simulation results. Richard Marchand assisted in the data analysis and contributed to the composition and edition of the manuscript. Johnathan Burchill and Matthias Förster contributed information on the front plate measurements and how these were used to infer plasma parameters, as well as providing feedback in the writing of the manuscript.

ACKNOWLEDGMENTS

Acknowledgments to my thesis supervisor Richard Marchand, for his guidance and support. I also thank to Johnathan Burchill, Matthias Förster, Stephan Buchert, and Thomas Nilsson for their valuable input and discussions.

This work was supported in part by the Consejo Nacional de Ciencia y Tecnología de México, and by the Natural Sciences and Engineering Research Council of Canada. Simulation results presented in this thesis were obtained with Compute Canada computing facilities.

TABLE OF CONTENTS

TABLE OF CONTENTS	vi
LIST OF TABLES	viii
LIST OF FIGURES	x
1 INTRODUCTION	1
2 NUMERICAL SELF-FORCE	15
2.1 PARTICLE-IN-CELL APPROACH	16
2.2 SELF-FORCE SUPPRESSION	22
2.3 EXAMPLE RESULTS	23
2.3.1 SINGLE ELECTRON IN AN OTHERWISE HOLLOW SPHERE	24
2.3.2 ELECTRON ORBITING A FIXED ION AT THE SPHERE CENTRE	25
2.3.3 TEST ELECTRON IN A PLASMA	30
3 SWARM FRONT-PLATE AS A PLANAR LANGMUIR PROBE	35
3.1 INTRODUCTION	35
3.2 METHODOLOGY	37
3.3 PHYSICAL MODEL FOR THE COLLECTED CURRENT	43
3.4 DISCUSSION	48
3.5 SUMMARY	52
4 SWARM SPHERICAL LANGMUIR PROBES	54
4.1 INTRODUCTION	54
4.2 METHODOLOGY	55
4.2.1 ORBITAL MOTION LIMITED THEORY (OML)	55
4.2.2 SWARM PROBE MEASUREMENTS INTERPRETATION	60
4.2.3 SIMULATIONS SETUP	61
4.2.4 RIPPLE TECHNIQUE	65
4.3 ION SATURATION REGION. PLASMA DENSITY	71
4.3.1 ION CURRENTS. ISOLATED PROBE	72
4.3.2 ION CURRENTS. SWARM PROBES	79
4.4 ELECTRON TEMPERATURE	88
4.4.1 ELECTRON CURRENTS. ISOLATED PROBE	90
4.4.2 ELECTRON CURRENTS. SWARM PROBES	93

4.4.3	RETARDATION REGION	97
4.4.4	INFERRED ELECTRON TEMPERATURE	98
5	SUMMARY AND CONCLUSIONS	103
	REFERENCES	110
A	APPENDIX A	124
B	APPENDIX B	130

LIST OF TABLES

3.1	FRONT PLATE SIMULATED COLLECTED CURRENTS.	42
3.2	RELATIVE ERRORS IN THE DENSITY INFERRED FROM THE SWARM FP COLLECTED CURRENTS.	52
B.1	SIMULATED ION CURRENTS COLLECTED BY THE ISOLATED PROBE. . .	131
B.2	RELATIVE ERRORS IN THE DENSITY INFERRED FROM THE ISOLATED PROBE COLLECTED CURRENTS.	132
B.3	FLOATING POTENTIAL.	132
B.4	SIMULATED ION CURRENTS COLLECTED BY THE SWARM PROBES. CASE 01.	133
B.5	SIMULATED ION CURRENTS COLLECTED BY THE SWARM PROBES. CASE 02.	134
B.6	SIMULATED ION CURRENTS COLLECTED BY THE SWARM PROBES. CASE 03.	135
B.7	SIMULATED ION CURRENTS COLLECTED BY THE SWARM PROBES. CASE 04.	136
B.8	SIMULATED ION CURRENTS COLLECTED BY THE SWARM PROBES. CASE 05.	137
B.9	SIMULATED ION CURRENTS COLLECTED BY THE SWARM PROBES. CASE 06.	138
B.10	SIMULATED ION CURRENTS COLLECTED BY THE SWARM PROBES. CASE 07.	139
B.11	SIMULATED ION CURRENTS COLLECTED BY THE SWARM PROBES. CASE 08.	140
B.12	SIMULATED ION CURRENTS COLLECTED BY THE SWARM PROBES. CASE 09.	141
B.13	SIMULATED ION CURRENTS COLLECTED BY THE SWARM PROBES. CASE 10.	142
B.14	SIMULATED ION CURRENTS COLLECTED BY THE SWARM PROBES. CASE 11.	143
B.15	SIMULATED ION CURRENTS COLLECTED BY THE SWARM PROBES. CASE 12.	144
B.16	SIMULATED ION CURRENTS COLLECTED BY THE SWARM PROBES. CASE 13.	144
B.17	SIMULATED ION CURRENTS COLLECTED BY THE SWARM PROBES. CASE 14.	145

B.18	SIMULATED ION CURRENTS COLLECTED BY THE SWARM PROBES. CASE 15.	145
B.19	SIMULATED ION CURRENTS COLLECTED BY THE SWARM PROBES. CASE 16.	146
B.20	SIMULATED ION CURRENTS COLLECTED BY THE SWARM PROBES. CASE 17.	146
B.21	SIMULATED ION CURRENTS COLLECTED BY THE SWARM PROBES. CASE 18.	147
B.22	SIMULATED ION CURRENTS COLLECTED BY THE SWARM PROBES. CASE 19.	147
B.23	RELATIVE ERRORS IN THE DENSITY INFERRED FROM SWARM PROBE COLLECTED CURRENTS.	150
B.24	SIMULATED ELECTRON CURRENTS COLLECTED BY THE SWARM PROBES. CASE 05.	154
B.25	SIMULATED ELECTRON CURRENTS COLLECTED BY THE SWARM PROBES. CASE 11.	156
B.26	RELATIVE ERRORS IN THE TEMPERATURE INFERRED FROM SWARM PROBE COLLECTED CURRENTS.	157

LIST OF FIGURES

1.1	PROBE CHARACTERISTIC EXAMPLE	6
1.2	PHYSICAL PROCESSES INVOLVED IN THE PARTICLE COLLECTION . .	11
1.3	PARTICLE COLLECTION IN THE OML APPROXIMATION	12
2.1	SELF-ACCELERATION WITHOUT THE SELF-ELECTRIC FIELD SUBTRAC- TION.	25
2.2	SELF-ACCELERATION WITH THE SELF-ELECTRIC FIELD REMOVED. . .	26
2.3	ELECTRON TRAJECTORY WITHOUT THE SELF-ELECTRIC FIELD SUB- TRACTION.	27
2.4	ELECTRON TRAJECTORY WITH THE SELF-ELECTRIC FIELD REMOVED.	28
2.5	ELECTRON TRAJECTORY IN VELOCITY SPACE WITH THE SELF-ELECTRIC FIELD REMOVED.	29
2.6	ELECTRON KINETIC ENERGY AS FUNCTION OF TIME.	32
2.7	ELECTRON ANGULAR MOMENTUM AS A FUNCTION OF TIME.	33
2.8	SELF-ACCELERATION AS FUNCTION OF THE NUMBER OF SIMULATION PARTICLES.	34
3.1	FRONT PLATE GEOMETRY USED IN THE SIMULATIONS.	38
3.2	CURVED EQUIPOTENTIALS AROUND THE FRONT PLATE.	44
3.3	ION TRAJECTORIES DEFLECTED NEAR THE FRONT PLATE. CASE 1. .	45
3.4	ION TRAJECTORIES DEFLECTED NEAR THE FRONT PLATE. CASE 2. .	46
3.5	CORRELATION BETWEEN THE RELATIVE ENHANCEMENT COMPUTED AND THE PREDICTED BY THE MODEL.	47
4.1	PLASMA PARAMETERS CONSIDERED IN THE SIMULATIONS.	61
4.2	SWARM SPHERICAL PROBES GEOMETRY USED IN THE SIMULATIONS.	63
4.3	RIPPLE TECHNIQUE USED IN SWARM.	66
4.4	CURRENT RESPONSE TO THE APPLIED TIME VARYING VOLTAGE OF THE SPHERICAL PROBE IN THE ION SATURATION REGION	69
4.5	CURRENT RESPONSE TO THE APPLIED TIME VARYING VOLTAGE OF THE SPHERICAL PROBE IN THE RETARDATION REGION.	70
4.6	SAMPLE OF CURRENTS COLLECTED BY THE TWO SWARM SPHERICAL PROBES AS A FUNCTION OF TIME.	74
4.7	CROSS-SECTION OF ELECTRIC EQUIPOTENTIALS WHEN THE ISOLATED PROBE IS OPERATED IN THE ION SATURATION REGION.	75
4.8	ION TRAJECTORIES DEFLECTED BY THE ISOLATED PROBE SHEATH. .	76

4.9	RELATIVE DIFFERENCES IN THE COLLECTED CURRENTS AND INFERRED DENSITIES FROM THE ISOLATED PROBE.	78
4.10	CROSS-SECTION OF ELECTRIC EQUIPOTENTIALS WHEN THE SWARM PROBES ARE OPERATED IN THE ION SATURATION REGION.	80
4.11	ION TRAJECTORIES DEFLECTED BY THE SATELLITE SHEATH. CASE 1.	81
4.12	ION TRAJECTORIES DEFLECTED BY THE SATELLITE SHEATH. CASE 2	83
4.13	RELATIVE DIFFERENCES IN THE COLLECTED CURRENTS AND INFERRED DENSITIES FROM THE SWARM PROBES.	85
4.14	ION SATURATION REGION OF THE PROBE CHARACTERISTIC.	87
4.15	CROSS-SECTION OF ELECTRIC EQUIPOTENTIALS WHEN THE ISOLATED PROBE IS OPERATED IN THE ELECTRON LINEAR REGION. $\vec{B} = 0$	91
4.16	ELECTRON TRAJECTORIES DEFLECTED BY THE ISOLATED PROBE SHEATH. $\vec{B} = 0$	92
4.17	CROSS-SECTION OF ELECTRIC EQUIPOTENTIALS WHEN THE ISOLATED PROBE IS OPERATED IN THE ELECTRON LINEAR REGION. $\vec{B} \neq 0$	93
4.18	ELECTRON TRAJECTORIES DEFLECTED BY THE ISOLATED PROBE SHEATH. $\vec{B} \neq 0$	94
4.19	CROSS-SECTION OF ELECTRIC EQUIPOTENTIALS WHEN THE SWARM PROBES ARE OPERATED IN THE ELECTRON LINEAR REGION. $\vec{B} = 0$	95
4.20	ELECTRON TRAJECTORIES DEFLECTED BY THE SATELLITE SHEATH. $\vec{B} = 0$	96
4.21	ELECTRON TRAJECTORIES DEFLECTED BY THE SATELLITE SHEATH. $\vec{B} \neq 0$	97
4.22	RELATIVE ERRORS IN THE TEMPERATURE INFERRED FROM COLLECTED CURRENTS.	99
4.23	RETARDATION REGION OF THE PROBE CHARACTERISTIC.	101

CHAPTER 1.

INTRODUCTION

The understanding of the physics inside the ionosphere, including its properties and dynamics, has become essential for space exploration, plasma physics research, and for the performance of thousand of satellites orbiting the Earth with research and commercial applications, including communications, GPS positioning and remote sensing. The upper atmosphere is partially ionized mainly by solar UV radiation and energetic particle impact [1, 2, 3]. As a result, the space above the neutral atmosphere consists of a large fraction of plasma. A plasma is an ionized gas in which the interaction between particles is collective. The ionosphere is a conductive layer where free charges can reflect, refract, attenuate or change the polarization of electromagnetic waves [4, 5]. The state of a plasma is characterized by several parameters including its density, temperature and ion composition. These parameters in turn determine the interaction of the space plasma with electromagnetic waves and spacecraft.

The properties of the ionospheric plasma vary with altitude, longitude, and latitude. An essential condition in the understanding of physical processes occurring in is to know the state of the plasma. Ionospheric density profiles are measured with ground-base observations including ionosondes [6, 7], and Incoherent Scatter Radars (ISRs) [8, 9, 10]. In addition to density, ISRs are also used to monitor ionospheric electron and ion temperatures [11]. Remote sensing techniques used to estimate the ionosphere density include the use Global Positioning System (GPS) receivers data [12, 13]. From Langmuir Probe (LP) in situ measurements, the electron density [14] and temperature

can be inferred as well [15, 16]. In laboratory, these plasma parameters can also be inferred using techniques such as the Thomson scattering, Faraday rotation, and the interferometry [17, 18, 19].

With the development of space technology, in situ exploration has become available. Particle sensors such as Langmuir probes have been widely used in multiple space missions [20, 21, 22] and in the laboratory [23] to infer the plasma density and temperature. Because such plasma parameters cannot be measured directly, probe measurements need to be interpreted on the basis of a theoretical model. Several approaches aimed to predict the collection of particles by a Langmuir probe have been developed for different plasma conditions and probe geometries [24, 25, 26, 27, 28, 29, 30, 31]. However, such interpretations generally come with significant uncertainties as a result of the approximations that are needed in order to solve the problem analytically [32, 33].

The Swarm constellation was deployed in 2013 by the European Space Agency (ESA) with the main mission to study the Earth magnetic field. In addition to the magnetometers which measure magnetic field with a sensitivity of approximately 50 pT, Swarm carries instruments to measure the Earth gravitational field, the ion velocity distributions, the plasma density and temperature. Lomidze et al. [34] have shown that the electron density and temperature measured on Swarm are generally underestimated and overestimated respectively, when compared with measurements made from independent sources such as the ISRs, the low-latitude ionosondes, the Constellation Observing System for Metrology, Ionosphere, and Climate (COSMIC) satellites [35, 36], and the International Reference Ionosphere (IRI) 2016 [37, 38]. The validation and correction of Swarm data done by Lomidze et al. stress the necessity of more comprehensive studies to explain the observed discrepancies.

The objective of this thesis is to study space plasma interaction with Swarm satellites

and particle sensors using kinetic simulations, so as to assess uncertainties resulting from the interpretation of probe measurements, based on the analytical models used in Swarm data processing. Specifically, the instruments considered are part of the Electric Field Instrument (EFI), which consists of two thermal ion imagers embedded in the front plate, and two spherical Langmuir probes, mounted on each satellite. When the ion imagers are not in operation, the front plate can be used as a planar Langmuir probe for additional diagnostics. The spherical probes are used primarily to infer the plasma density and temperature from collected currents as a function of bias voltages. The specific objectives are to:

1. Assess qualitatively and quantitatively, the relative enhancements in the ion collection currents associated with fringe effects around the front plate, when it is used as a planar Langmuir probe. These relative enhancements are then fitted and parameterized in terms of environmental plasma parameters.
2. Assess the methodology used to interpret the spherical probe measurements based on the Orbital Motion Limited (OML) theory and identify physical causes of uncertainties. These objectives are achieved by following this approach:
 - (a) By using kinetic simulations, currents collected by the Swarm probes are calculated under a sample of ionospheric plasma conditions while accounting for, the plasma ion mass composition, the geomagnetic field (in some cases) and the presence/absence of the satellite.
 - (b) Plasma parameters are inferred from calculated currents interpreted on the basis of OML approximation as in actual Swarm data processing.
 - (c) The inferred plasma parameters are then compared to those used as input in the simulations allowing an estimate of the uncertainty and its sources.

- (d) Associating sources of uncertainties in the inferred parameters with plasma conditions, is a first step in the development of an improved methodology to interpret probe measurements.

In the remainder of this chapter, kinetic simulations approaches are briefly reviewed. The physical processes involved in the collection of plasma particles by a spherical probe are reviewed. For reference, the Orbital Motion Limited (OML) theory used in the interpretation of Swarm spherical probes measurements is also presented.

KINETIC SIMULATIONS

Kinetic simulations provide a detailed description of plasma particles in configuration and velocity space.

In the Vlasov approach, this is accomplished by directly solving for the Vlasov equation in phase space with electromagnetic fields calculated self-consistently [39, 40, 41, 42].

In the Particle-In-Cell (PIC) approach, particle positions and velocities, are obtained by solving particle equations of motion in self-consistently computed fields from solutions of Poisson’s equation and/or Maxwell equations [43, 44, 45]. In this process particle distributions, density, and fields are discretized on a computational grid.

In the hybrid approach, some plasma species are treated kinetically while others are treated in the fluid approximation [46, 47, 48, 49]. In this approach, fields are also computed self-consistently.

In the test particle approach, particle trajectories are calculated using prescribed electric and magnetic fields obtained from other source, e.g. actual measurements, analytic approximations, or from other computer models [50, 51, 52, 53,

54, 55, 56, 57, 58]. This approach, while not fully self-consistent, can provide useful information concerning plasma kinetic properties. Test particle simulations can also be used to check consistency of results obtained with fluid models [59]

PIC simulations have the advantage of being more straightforward to implement and more readily applicable to geometries discretized with unstructured grids. For this reason, the PIC approach, implemented in the PTetra code, is used in this thesis. PTetra is a three-dimensional, electrostatic, fully kinetic PIC code, that utilizes an adaptive, unstructured, tetrahedral mesh to discretize the simulation domain. The use of an electrostatic code is justified by the fact that along Swarm orbits, the magnetic field generated by currents induced by satellite-plasma interactions, are several orders of magnitude smaller than the background magnetic field [60].

LANGMUIR PROBES: THEORY

The Langmuir probe consists of an electrode of a metallic conductor that is immersed in the plasma. The probe is biased to a certain potential resulting in current collection. The relation between current collected, and applied voltage is known as the probe characteristic. Figure 1.1 shows an example of a probe characteristic. A combination of physical processes and plasma conditions determine the current collection in the different regions of the probe characteristic. The key parameters used to infer the state of the plasma are:

The plasma potential V_{plasma} is the electric potential in absence of a probe or satellite. It could be seen as the space potential. If the probe is set to a sufficiently larger voltage V than the plasma potential, the collected current increases linearly with the applied voltage. In the probe characteristic example in Fig. 1.1, the plasma potential is at zero voltage.

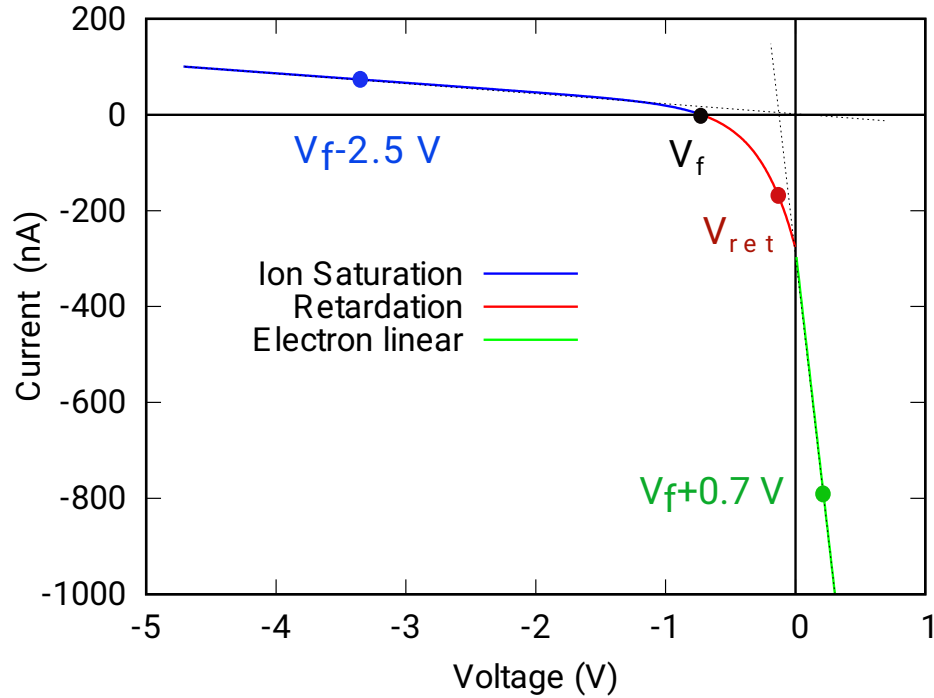


Figure 1.1: Illustration of a Langmuir Probe ampere-volt characteristic with respect to the plasma potential.

The floating potential V_f is the voltage of an object in a plasma, such that it collects zero net current (dark circle in Fig. 1.1). V_f can have positive as well as negative values depending on the state of the plasma and the nature of the object itself (e.g. spacecraft or probe).

The electron linear region or electron saturation region (green line in Fig. 1.1), is the region of the characteristic where $V > V_{plasma}$, and where electrons contribute most of the collected current, and where the collected current varies linearly with the probe voltage. In this region electrons contribute practically to all the current collected, which depends linearly on the probe bias voltage.

The retardation region is the transition region where the probe potential is at $V_f < V < V_{plasma}$, as illustrated in red line in Fig. 1.1. The width of the

retardation region is related to the electron temperature since that determines the voltage (floating potential) that is required to cut off the thermal electron contribution to the collected current.

The ion saturation region is the region of the characteristic where the potential is sufficient negative for the collected current to come mainly from positive ions. In this region, the current collected by a spherical probe is approximately proportional to the applied voltage, as illustrated with the blue line in Fig. 1.1.

DEBYE SHIELDING

The challenge in probe theory is to understand plasma perturbations due to the presence of the probe in the observed collected current, and how these perturbations are related to the parameters of the unperturbed plasma far from the probe. Perturbations in the electric potential due to the presence of the probe are short-ranged compared to those in vacuum. That is because plasma particles, particularly electrons, can quickly redistribute to shield and smooth out any perturbation to the plasma potential. Perturbations on the charge distribution have an effect on the electric potential only at distances comparable to the Debye length defined as

$$\lambda_{De} = \sqrt{\frac{\epsilon_0 k T_e}{e^2 n}}. \quad (1.1)$$

In Eq. 1.1, ϵ_0 is the permittivity of free space, k is the Boltzmann constant, T_e is the electron temperature, e is the elementary charge, and n is the plasma density. In a stationary plasma, electric field perturbations at a point only extend to a few Debye lengths from the perturbations. At larger distances, potential perturbations are attenuated exponentially in a process referred to as Debye shielding.

PHYSICAL PROCESSES IN THE CHARGED PARTICLE COLLECTION

The charged particle collection by a Langmuir probe is a complex phenomenon because it involves several processes and diverse plasma conditions.

Supersonic flow. A probe immersed in drifting plasma, would collect particles due to plasma flow as illustrated in Fig. 1.2 (left). In the ionosphere, low Earth orbit (LEO) satellites travel with velocities of several km/s (Swarm ram speed $v_s \simeq 7673$ m/s). Ion thermal speeds for a typical temperature of order 0.1 eV, are 1 and 4 km/s for Oxygen and Hydrogen ions respectively. This implies that, in the probe rest frame, incoming ions reach the probe with a velocity approximately equal to the satellite ram velocity plus their respective thermal velocity and possible ionospheric wind velocities. Moreover, because LEO satellites ram speeds are generally larger than their thermal speed, incoming ions reach the probe with supersonic speeds. Electrons on the other hand, have much higher thermal speeds (of order of 230 km/s) in comparison to which, satellite ram velocities can neglected to first approximation.

Thermal motion. The thermal motion of plasma particles is another process from which the probe collects particles, Fig. 1.2 (center). Because plasma particles have random thermal velocities, electrons and ions reach the probe from all directions if the plasma is at rest. In a supersonic plasma however, the ion current is primarily on the ram face of the probe, while for electrons, owing to their much larger thermal speed, are collected nearly isotropically.

Attractive/repulsive electric field. A third contribution to the current collection comes from considering the probe bias voltage, Fig. 1.2 (right). The electric field associated with gradients in the equipotentials surrounding the probe, deflects

incoming particles, by either attracting or repelling them. Lighter particles are deflected more than heavier ones. When the probe is biased to a certain voltage, the collection of the attracted species is enhanced due to an increase in the collection area associated with the probe sheath. It is the opposite for repelled species, for which the collection effective area decreases, and only particles with sufficient energy can reach the probe.

Magnetic field. Particle collection in a magnetized plasma depends on the ratio between the magnetic gyroradius of the particles and the dimension of the probe. If this ratio is large, the plasma is effectively unmagnetized. However, if this ratio is close to 1 or less, particle collection is affected by the magnetization of the plasma [61]. Typical values of the magnetic field in the ionosphere result in a gyroradius of several meters for ions, and a few centimeters for electrons. As a result, depending of the dimension of the probe and the species being collected, the magnetization of the plasma is relevant in the collection of the particles or not.

Presence of nearby objects. The position of the probe relative to the satellite bus may affect particle collection. Other instruments on-board and the satellite itself may represent an obstacle between the incoming particle and the probe. Moreover, in space satellites charge to a certain voltage (floating potential) with respect to the background plasma. The probe could then be in the vicinity of the satellite electric sheath which, and depending on the separation length between probe and satellite, may have an effect on the particle collection. Additionally, depending on the orientation of the geomagnetic field with respect to the satellite, field lines can connect the probe with other satellite components, thus, blocking magnetized species traveling in flux tubes along magnetic field lines.

Multiple ion species. Another important consideration in the collection of particles is the presence of multiple ion species in the plasma. The four ion species predominant in the ionosphere are singly ionized Hydrogen H^+ , Helium He^+ , Nitrogen N^+ and Oxygen O^+ , with concentration varying with altitude, latitude, longitude. Lighter ion species are attracted or repelled more efficiently by electric sheaths (probe or satellite) than heavier ones. As a result, for a given attractive voltage, the collection of lighter ions is larger than for the heavier ones.

Photoelectron emission. LEO satellites are exposed to solar radiation, thus, photoelectrons are emitted. Photons impacting the satellite surface with energy larger than the work function of the satellite material can extract electrons from it. Photoelectron emission has an effect on the collected current since every electron emitted is equivalent to a collected ion. The magnitude of the photoelectron current depends on the material work function, the illuminated surface area as well as the angle of the solar rays with respect to that surface [62, 63].

Collisions. Collisions between particles in a plasma-probe environment tend to reduce the collected current. When collisions occur, particles diffuse impeding the free travel of particles towards the probe. Ionospheric plasma, above 200 to 300 km altitude, have larger collisional mean free paths than the length scale of satellites (meters), and therefore can be treated as collisionless.

ORBITAL-MOTION-LIMITED THEORY

OML theory predicts an orbital limited particle collection of a Langmuir probe immersed in a plasma. One condition for the OML approximation to be valid is that the Debye length be larger than the probe radius; such a condition generally applies to

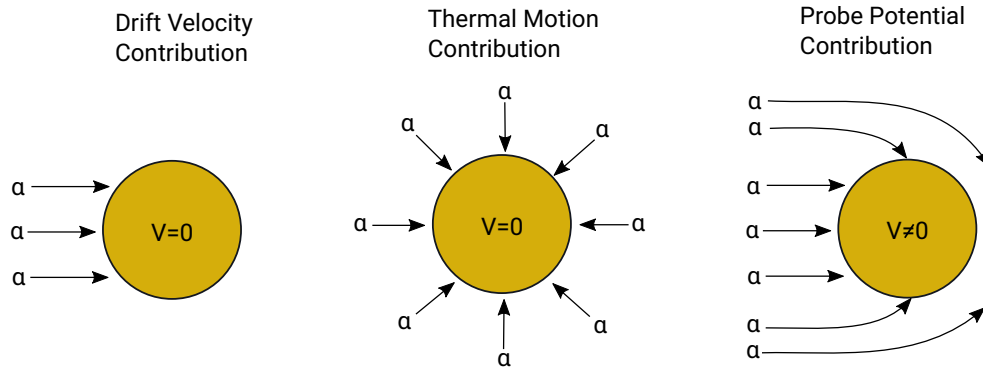


Figure 1.2: Spherical probe particle collection. A probe immersed in a supersonic drifting plasma would collect particles due to ballistic incoming ions, electron thermal motion, and the deflected particles due to the probe bias potential [16].

Swarm's spherical probes. In the derivation of OML equations, as in many other theories, several assumptions have to be made in order to solve the problem analytically.

These assumptions include:

1. Conservation of energy and angular momentum.
2. Particles are collected due to the plasma flow, the thermal motion and the electric field surrounding the probe as illustrated in Fig. 1.2.
3. The contribution to the net current of the different particle species is given by a linear superposition of the currents collected by each specie.
4. All particle species have a Maxwellian distribution function.
5. Magnetic field effects are negligible.
6. There are no nearby objects or obstacles between plasma particles and the probe.

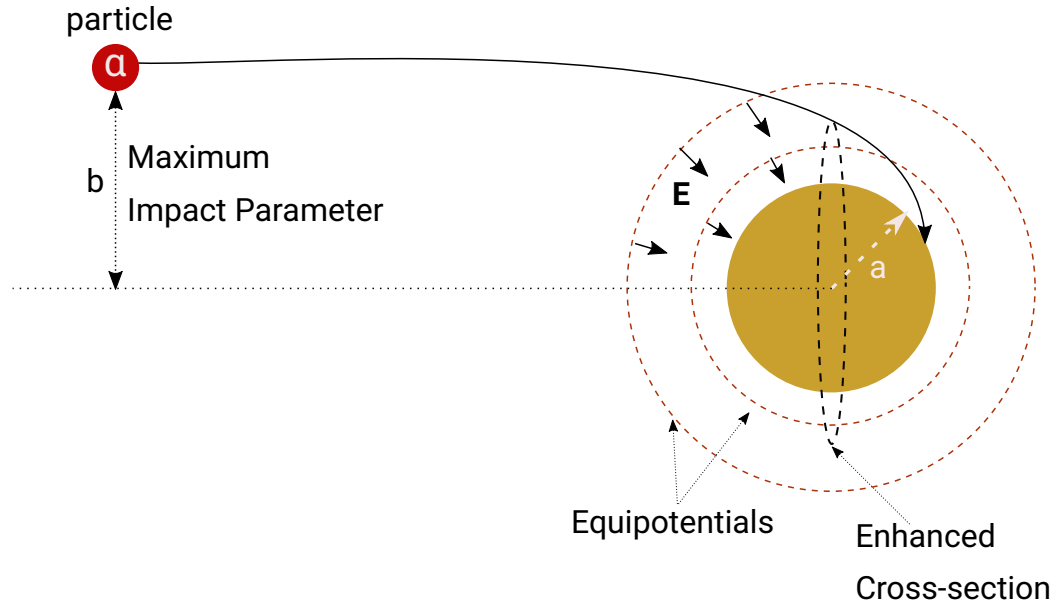


Figure 1.3: Illustration of the collection of an attracted particle in the OML theory.

In Fig. 1.3 an incoming particle α is deflected by the probe sheath electric field that otherwise would miss the probe. Particles with a charge of the opposite sign to that of the probe potential are assumed to be collected if their trajectories fall inside the *maximum impact parameter* b . OML theory then predicts an enhanced cross-section which depends on the ratio between the probe bias voltage and the energy of the particle species. Particles with a charge of the same sign as the probe potential on the other hand, will be deflected and not collected, unless they have sufficient energy to overcome the potential barrier.

A full set of equations for a spherical Langmuir probe in a drifting plasma is derived in Appendix A for reference [64]. In Swarm, under the assumption that the plasma flow which is assumed to be equal to the satellite orbital speed, is much larger than the ion thermal speeds, and owing to the fact that electrons have a much higher thermal speed than the satellite ram speed, a set of equations for the collected current for the

three relevant regions of the probe characteristic is obtained. These equations are

$$I_{lin} = 4\pi a^2 en \sqrt{\frac{kT_e}{2\pi m_e}} \left(1 + \frac{eV}{kT_e}\right), \quad (1.2)$$

for the electron linear region,

$$I_{ret} = \pi a^2 env_d \left(1 - \frac{2eV}{m_e v_d^2}\right) - 4\pi a^2 en \sqrt{\frac{kT_e}{2\pi m_e}} \exp\left(-\frac{eV}{kT_e}\right), \quad (1.3)$$

for the electron retardation region, and

$$I_{ion} = \pi a^2 env_d \left(1 - \frac{2eV}{m_i v_d^2}\right), \quad (1.4)$$

for the ion saturation region. In these equations $m_{e/i}$ represents the electron/ion mass, e is the electron charge, a the radius of the probe, k the Boltzmann constant, T_e the electron temperature, v_d the ion drift velocity (plasma flow velocity), I_x the collected current, and V the probe voltage with respect to the background plasma.

It must be noticed that a contribution to the total current from electrons and ions always exists, however, in the electron linear and ion saturation region, the current collected is dominated by electrons and ions respectively, thus, the contribution of the repelled species is generally neglected in the equations for simplicity. The set of equations presented above are used in Swarm data processing to infer plasma parameters from probe measurements [65]. The plasma density is determined from measurements in the ion saturation region, whereas combining the electron retardation with ion saturation data, the electron temperature is inferred. These equations can easily be incorporated in the processing data algorithm used to infer plasma parameters from continuous streams of probe measurements obtained in space missions.

Outline

The remainder of the thesis consist of the following sections:

1. Particle-in-cell (PIC) simulations are used as the primary tool to study plasma interactions with particle sensors. In the second chapter, the well-established PIC approach is briefly reviewed. Then, a methodology to suppress, to machine accuracy, the self-force that appears in most PIC simulation is presented with examples results.
2. The relative enhancement observed in the collected current by the Swarm front-plate when operated as planar probe is investigated in the third chapter.
3. Swarm spherical Langmuir probes are studied under realistic conditions to test the accuracy of the inferred parameter on the basis of OML theory in the fourth chapter.
4. In the fifth and last chapter, a summary and final conclusions on the Swarm probes are given while open questions and future work are mentioned.
5. Additionally, two appendices are included.
 - (a) Appendix A contains the derivation of the analytic expression for the current collected by a spherical probe immersed in a drifting plasma on the basis of OML theory.
 - (b) In appendix B, simulation results used in the analysis of the Swarm spherical Langmuir probes in the fourth chapter of this thesis, are tabulated.

CHAPTER 2.

NUMERICAL SELF-FORCE

The self-force is a non-physical force that a particle exerts on itself as a result of the discretization of charge density on a computational grid, and the interpolation of electric fields back to particle positions. In this chapter a method is presented to remove the numerical self-force that appears in particle-in-cell (PIC) simulations in computational domains discretized with general meshes and boundary conditions.

In an electrostatic PIC simulation, the volume charge density associated with a distribution of point charges in space, is discretized on a grid with suitable interpolation functions. The resulting charge density is then used to determine the electric potential and electric field at mesh vertices by solving Poisson's equation. In the integration of particle trajectories, the electric field at a given particle position is then obtained similarly by interpolating electric fields from nearby vertices in a given cell. With a structured Cartesian uniform mesh and periodic boundary conditions, Hockney and Eastwood [66] demonstrated that using the same interpolation function for distributing particle charges to grid vertices, as used for interpolating electric fields at particle positions, the self-force is avoided to machine accuracy. This approach to avoid self-forces has been used for example in work by Colella [67], Boris [68], Vondor [69], and Cornet [70]. In non uniform unstructured meshes with multiply connected domains, or more general boundary conditions however, the self-force is unavoidable in the standard PIC approach, which can be a concern in some simulations, and this problem remained unsolved until now. In this study, the first solution to this problem

is presented with a straightforward and efficient method to suppress the self-force for arbitrary meshes and boundary conditions. The method is illustrated with simulation results using an unstructured tetrahedral mesh in spherical geometry. As an introduction to the numerical self-force problem, a brief presentation of the most relevant aspects of the PIC methodology is given. A detailed discussion of the PIC approach based on PTetra, can be found in [71, 72].

2.1 PARTICLE-IN-CELL APPROACH

The particle-in-cell approach is used extensively in computational plasma physics to study a variety of complex processes ranging from magnetic reconnection in laboratory experiments, e.g. Fox [73], to space plasma, e.g. Birn [74], Pritchett [75], Drake [76], and Daughton [77]. The basis of the PIC approach, involving the computation of particle trajectories, with forces computed on a grid and interpolated back to particle positions, was introduced by Harlow [78, 79] and applied to 2D compressible fluids. Harlow’s approach was later applied to plasma simulations by Birdsall and Fuss [80]. Buneman had introduced the second-order time stepping in particle codes [81], two years before Birdsall-Fuss’s work. Another fundamental idea was introduced by Dawson who developed the concept of finite-size particles [82]. Hockney presented a fast solution to Poisson’s equation [83], using Fast Fourier Transforms (first introduced by Cooley and Tukey in late 1960’s), which allowed for multi-dimensional particle-in-cell (2D PIC models by the early 70’s). The method has since been described in detail in a number of articles, including those by Dawson [84] and Verboncoeur [85], along with textbooks, as for example those of Birdsall-Langdon [86] and Hockney-Eastwood [66].

The PIC approach has since been in constant development, extending early one-dimensional electrostatic models to multi-dimensional electromagnetic models as

in the work by Friedman [87], Villasenor [88], Verbouncoeur [89] and Vahedi [90]. Collisions, not accounted for in the early PIC models, have been included for example, in work by Birdsall [43] and Vahedi [91]. High density degenerate plasma has also been simulated with the PIC approach in work for example, by Sentoku [92]. Liewer [93], Briguglio [94] and Di Martino [45], also demonstrated that PIC simulations can use parallel computing to simulate plasma while accounting for complex physical processes under realistic conditions. Results from such comprehensive simulations can be used to plan and interpret laboratory and space plasma experiments as demonstrated by Fahleson [95], Morse-Nielson [96], Tribble [97], and Hosada [98].

THE MESH

In the particle-in-cell (PIC) approach, in order to calculate the physical process involved in the plasma particle interaction, it is necessary to use a mesh to discretize and represent the simulation domain along with all the physical components inside it. Once the particle positions on the mesh are known, physical quantities such as fields and charge density, can be interpolated at particle positions. The mesh used in simulations can be structured or unstructured. In a structured mesh, it is relatively straightforward to determine the position of the particle by knowing its coordinates. In simulations where a structured mesh is used in combination with periodic boundaries, the field equation (Poisson's) can be solved very efficiently by using the fast Fourier transforms. Structured meshes, on the other hand, are less suitable to discretize irregular shapes of objects or boundaries. Unstructured adaptive meshes are an alternative that allows one to represent more complex and realistic simulation domains. In unstructured meshes, the relation between the position of the particle and the mesh, as well as the solution to the field equation, are not as straightforward as in structured ones with periodic boundaries. The use of adaptive unstructured meshes in PIC simulations is generally more complex than using structured ones.

BOUNDARIES

In basic plasma physics problems where simulation domains are rectangular prisms and delimited only by an outer boundary, periodic conditions can be imposed and the physics is determined by the initial conditions and specified driving forces. In cases where internal boundaries are used to represent surfaces of components in the simulation domain, open boundaries for the outer boundary are more suitable. If open boundaries are used, particles leaving the system are lost and they are not necessarily reinjected at a prescribed location as it is done with periodic boundaries. This implies that the total number of particles of a given species may vary in time.

MACROPARTICLES AND STATISTICAL WEIGHT

Because simulate the actual number of plasma particles is impractical, in the PIC approach, macroparticles represent collectives of physical particles to be traced in. Macroparticles have then a *statistical weight* equal to the ratio of the number of physical particles in the volume to the number of macroparticles

$$\omega_\alpha = \frac{V n_\alpha}{N_\alpha}. \quad (2.1)$$

In Eq. 2.1 V is the volume of the simulation domain, n_α is the density of species α , while N_α is the total number of macroparticles of species α . By multiplying moments computed from macroparticles distributions by their respective statistical weight, moments of the distributions of particles, such as the density and particle flux density, can be calculated. In PTetra, simulations can be restarted upon completion. One interesting feature is that a restart can be done with the same, or a different number of macroparticles. This provides a convenient way to verify whether the number of macroparticles is sufficiently large in a given simulation.

PARTICLE INITIALIZATION AND REINJECTION AT BOUNDARIES

It is always necessary to initialize the state of the system at initial time, involving distributing particles in the simulation domain, and charges on components, if there are any. Ideally, the system should be initialized in a state that would approximate the final state, whether one is interested in a steady state, or a time dependent solution. This however, it is usually not possible. The simplest way to initialize the system is to distribute all particles species uniformly in space, with consistent densities and velocity distribution functions. In Ptetra, at initialisation, particles are distributed randomly in each tetrahedron, in numbers proportional to the tetrahedron volume. This initial distribution tends to lower the level of statistical noise when a simulation is started. Once particles are given a position in space, the next step is to assign them velocities consistent with a prescribed normalized probability density function $f(\vec{v})$.

In the case of open boundaries, as particles leave the simulation domain, they are lost, and in order to simulate a realistic plasma conditions, particles must continually be replaced by new particles consistently with the assumed background distribution functions. The outer boundary of the simulation domain should be sufficiently far from any object and associated electric sheath, for electric forces on injected particles to be negligible.

VOLUME CHARGE DENSITY AND OTHER MOMENTS

Once particles have been distributed spatially in the grid, it is necessary to define a space charge density to calculate the electric potential by solving the Poisson's equation. From the electric potential the electric field is calculated and used to solve particle equations of motion. In PTetra, the charge density is assigned at every grid

point by using linear interpolation functions $\psi_j(\vec{r})$ defined such that

$$\psi_j(\vec{r}) = \begin{cases} 1 & \text{when } \vec{r} = \vec{r}_j \\ 0 & \text{at every other vertex} \end{cases} \quad (2.2)$$

and ψ_j varies linearly in any tetrahedron. Given these basis functions ψ_j defined at every mesh vertex, and a distribution of particles with position \vec{r}_i and charges q_i , the charge density at a given grid point r_j is calculated from

$$\rho_j = \frac{1}{\mathcal{V}_j} \sum_{i=1}^N w_i q_i \psi_j(\vec{r}_i) \quad (2.3)$$

where \mathcal{V}_j is the volume of the Voronoi cell at node j . These cells are defined for every grid point \vec{r}_j , and they are delimited by bisector planes perpendicular to every segment of tetrahedra having \vec{r}_j as a vertex. Other moments of phase space particle distribution can be calculated similarly. For example, the particle density of species α at a given mesh point would be given by

$$n_j = \frac{1}{\mathcal{V}_j} \sum_{i=1}^N w_i \psi_j(\vec{r}_i) \quad (2.4)$$

In addition to charge and particle densities, average drift velocity, temperature and stress tensor of particles can be calculated similarly.

INTERPOLATION OF THE ELECTRIC FIELD

The solution to Poisson's equation yields the electrostatic potential ϕ at each grid point. Since in PTetra linear interpolation functions are used, the calculated electric field from the finite-element solution of Poisson's equation is constant at each tetrahedron. This yields a discontinuous field at boundaries between neighbor tetra-

hedrons, and the electric field cannot be defined at vertices. In PTetra, this problem has been addressed by assigning to each vertex the average electric field calculated from all elements to which the vertex belongs. Once the electric field is defined at grid points, the same linear interpolation functions used to distribute the charge into mesh points, can be used to calculate the electric field at any given position inside elements as follows

$$\vec{E}(\vec{r}) = \sum_{j=1}^4 \psi_j(\vec{r}) \vec{E}_j. \quad (2.5)$$

PARTICLE TRACKING

In PTetra, the equations of motion for ions, are solved using a second order leapfrog algorithm, in which the particle positions are known at time steps, while velocities are calculated at half time steps. This algorithm is used for ions whether there is an external magnetic field or not. For electrons, in the absence of a magnetic field, the second order leapfrog is also used. However, if a magnetic field exists, the electron velocities are advanced in time using the Boris algorithm [99, 100], and the time step is set to be smaller than the electron gyroperiod (in PTetra, $\delta t \leq \frac{1}{10} \frac{2\pi}{|\Omega_e|}$, where Ω_e is the electron gyroperiod).

STABILITY

The general criteria for numerical stability of PIC simulations with structured meshes can be extended to unstructured meshes. Self-heating and instabilities can be avoided in PIC simulations by fulfilling the following conditions.

1. The electron Debye length must be resolved by the mesh.
2. The time step must be smaller than the electron plasma wave period $\delta t \omega_p < 1$.
3. In the presence of an external magnetic field, the time step must be smaller than the electron gyroperiod, $\delta t \Omega_e < 1$.

4. 'Most particles' should not cross more than one Voronoi cell in one-time step.

Note that in PTetra, the time step is calculated automatically in order to resolve the plasma and cyclotron frequencies, and to ensure that most particles do not cross more than the linear scale of the smallest Voronoi cell in a single time step.

2.2 SELF-FORCE SUPPRESSION

A straightforward way to suppress the self-force in electrostatic PIC simulations, under general conditions of geometry, computing grid, and boundary conditions, consists of calculating the self-electric field at every particle position, and subtracting it from that calculated from all particles (including the particle itself) in the system. Owing to the linear superposition principle in electrostatics, this can be done by precomputing an array of electric fields at neighboring nodes, associated with a unit charge at every node of a given computing grid. Given a distribution of charges in a simulation, and using the same interpolation scheme as for the charge density at mesh nodes, this array can then be used to interpolate the self-electric field at any particle position and therefore suppress the self-force. To be specific, the removal of self-forces is obtained as follows:

1. In each element l , successively assume a unit charge on every cell node k , with zero charge at all other nodes.
2. In each case, solve Poisson's equation, and determine the electric field \vec{E} at k , and at every other node j in element l , and record these electric fields in an array, say $\vec{E}_{j,k,l}$.
3. In a simulation, solve Poisson's equation in the usual way, accounting for all particles in the system at a given time step.

4. In each cell and for each particle, use the precomputed $\vec{\mathcal{E}}_{j,k,l}$ array to determine the self-electric field \vec{E}_{sf} . For example in an unstructured tetrahedral mesh, the self-electric field on particle i at position \vec{r}_i would be given by

$$\vec{E}_{sf}(\vec{r}_i) = \sum_{j=1}^4 \sum_{k=1}^4 \left(w_{j,l}(\vec{r}_i) q_i \vec{\mathcal{E}}_{j,k,l} \right) w_{k,l}(\vec{r}_i). \quad (2.6)$$

where q_i is the particle charge in unit charge, and the weights are interpolation functions in a given cell, which depend on the particle position \vec{r}_i , such that, for a given cell, their sum equals unity.

5. Finally, subtract the self-electric field from $\vec{E}(\vec{r}_i)$ calculated previously:

$$\vec{E}_{cor}(\vec{r}_i) = \vec{E}(\vec{r}_i) - \vec{E}_{sf}(\vec{r}_i). \quad (2.7)$$

This procedure requires the construction of an extra array, $\vec{\mathcal{E}}_{j,k,l}$ which, for a fixed grid, only needs to be computed once at the beginning of a simulation. This array requires relatively little additional memory, and once computed, the subtraction of the self-electric field at every particle position, at every time step is found empirically to have relative small impact on run time.

2.3 EXAMPLE RESULTS

The self-force subtraction algorithm described above is now illustrated with case studies involving i) a single electron in a sphere, ii) an electron orbiting a fixed nucleus at the sphere centre, and iii) a test electron in a plasma, for various numbers of simulation particles per Voronoi cell. We recall that Voronoi cells are defined at mesh vertices, and therefore the number of Voronoi cells is equal to the number of vertices in the mesh. The spherical domain considered has a radius of 1 m. It is discretized using

a tetrahedral mesh consisting of 1079816 tetrahedra and 179969 vertices. The mesh spatial resolution is uniform through the volume and approximately 0.025 m. The same mesh is used in all cases, and comparisons are made between results obtained without and with subtraction of the self-force.

2.3.1 SINGLE ELECTRON IN AN OTHERWISE HOLLOW SPHERE

We start by considering the components of the acceleration of a single electron in an otherwise empty sphere. The acceleration is obtained by computing the charge distribution associated with the presence of a single electron at varying positions along z , solving Poisson’s equation, obtaining the electric field at each mesh vertex, and interpolating it back to the electron position. In these calculations, the actual electron mass and charge are used to calculate the self-acceleration vector \vec{A} . Figure 2.1 shows the components of the x , y , and z components of the self-acceleration vector obtained in the usual PIC approach, in which the self-force is not subtracted, while Fig. 2.2 shows the residual self-acceleration when the self-force is subtracted. Without subtraction of the self-force, the self-acceleration ranges approximately between $\pm 10^4 \text{m/s}^2$, while with subtraction, the self-acceleration is within approximately $\pm 8 \times 10^{-7} \text{m/s}^2$. This represents a suppression in the self-force by approximately ten orders of magnitude. The residual in the self-force is caused mainly by numerical errors in the solution of Poisson’s equation, and to a lesser extent, roundoff errors in the interpolation and subtraction of the self-electric field at the particle position. Another striking difference between the figures is the absence of the large peak in the acceleration near the boundary, at $z = 1$ m. As noted in [71], this peak is due to the attraction of the electron by its mirror image as it approaches the outer boundary where a fixed potential is imposed. The self-force subtraction algorithm therefore has the additional advantage of removing the unphysical mirror force at the simulation

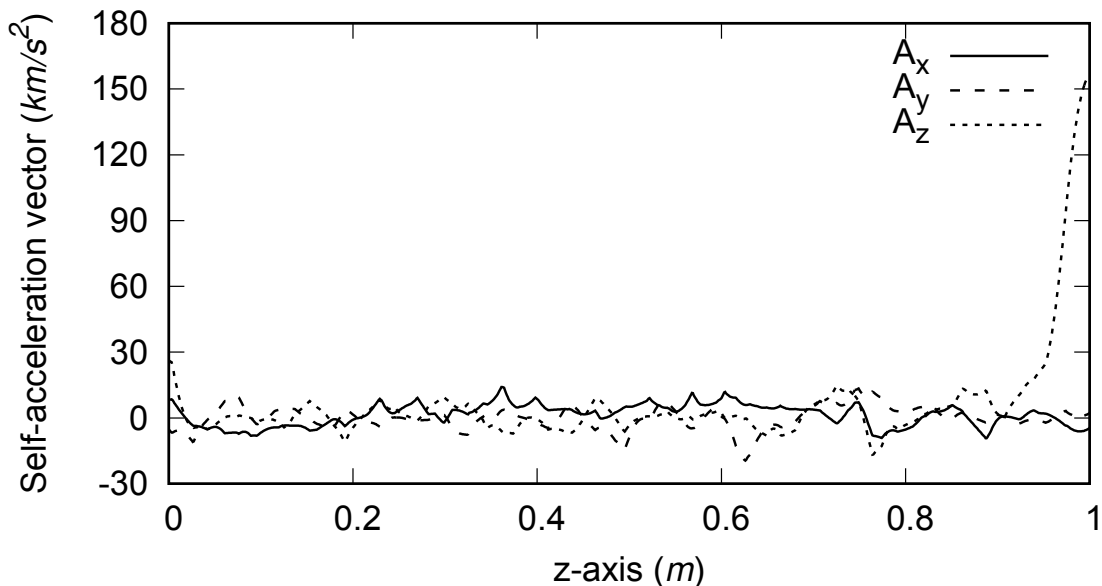


Figure 2.1: Components of the self-acceleration vector of an electron along the z axis computed without self-electric field subtraction. The large peak near the boundary, at $z = 1$ m, is due to the attraction of the electron by its mirror image [71].

domain boundary.

2.3.2 ELECTRON ORBITING A FIXED ION AT THE SPHERE CENTRE

The second example considered is the trajectory of an electron in the presence of a fixed proton at the centre of the sphere. The initial conditions assumed for the electron are such that, in an ideal central electrostatic potential, it would follow a circular orbit in the $x - y$ plane. Without self-force subtraction, Fig. 2.3 shows that the trajectory is erratic, and the electron quickly moves out of the simulation domain without completing a single orbit period. With the self-force subtracted however, the trajectory remains close to a circle for several cycles in both configuration and

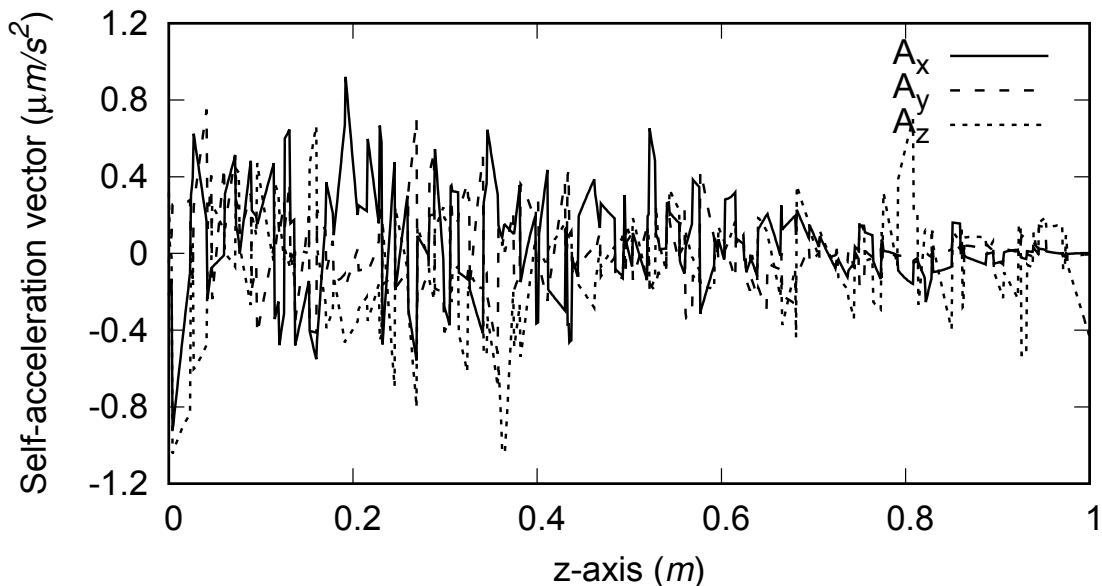


Figure 2.2: Components of the self-acceleration vector \vec{A} computed along the z axis when the self-electric field is removed. The self-acceleration is within approximately $\pm 8 \times 10^{-7} \text{m/s}^2$, which represents a suppression of the self-force by approximately ten orders of magnitude. The unphysical mirror force at the simulation domain boundary is also removed as a result of the self-electric field subtraction.

velocity space, as shown in Figs. 2.4 and 2.5.

In this case, the main cause for the small deviations from a perfect circle, are attributed to discretization errors associated with the finite resolution of the field on the tetrahedral mesh. This discretization results in small errors in the proton electric field along the electron trajectory, compared to an ideal radial $1/r^2$ field. These deviations in turn result in small excursions away from a perfect circular orbit.

Figure 2.6 shows variations in the electron kinetic energy during the first three orbit periods. While increasing in time, the relative deviations from the initial value remain

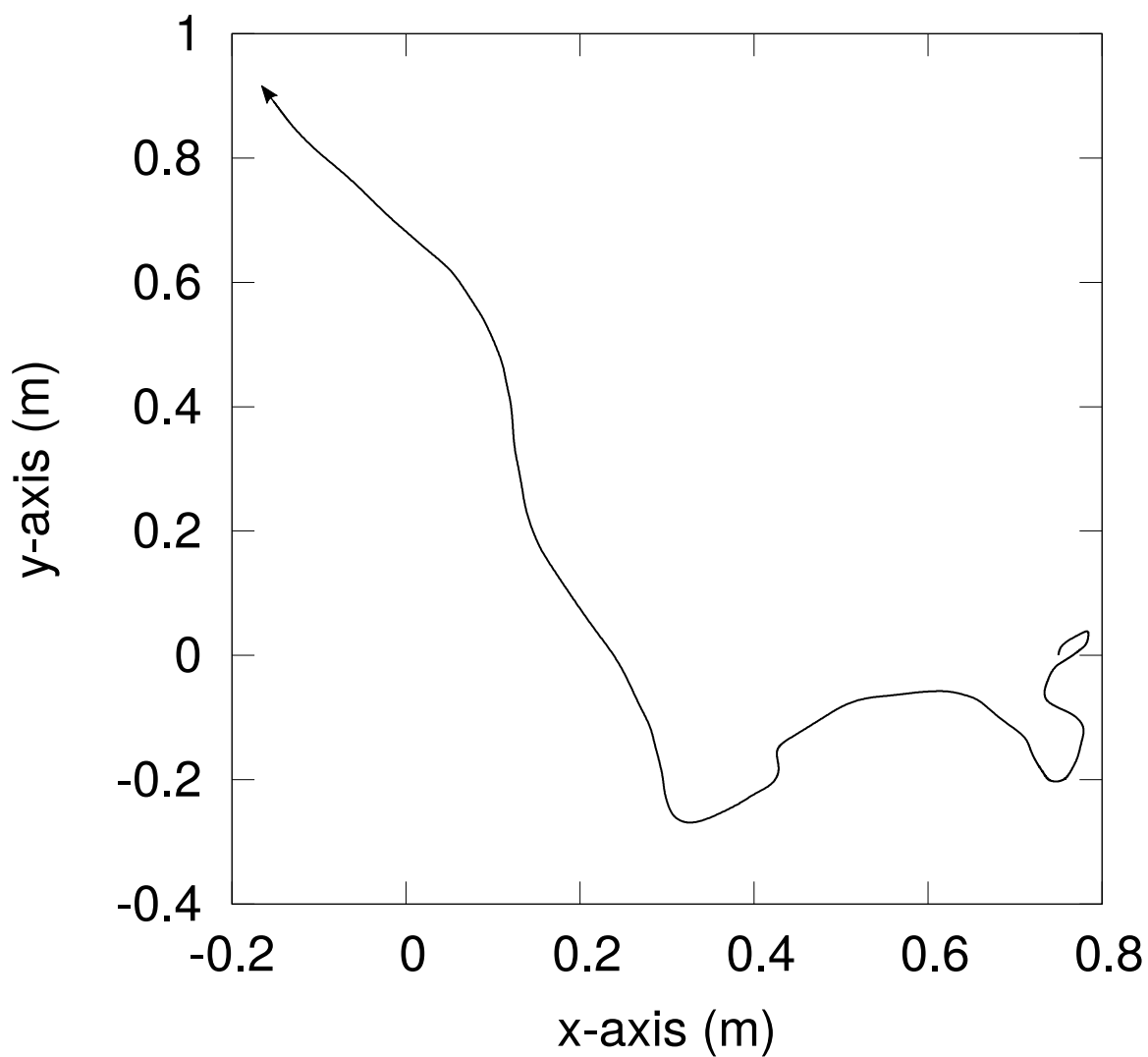


Figure 2.3: Electron trajectory computed without subtracting the self-electric field, with initial conditions such that the orbit should be circular, with a radius 0.75 m. The self-force in this case causes large deviations from the particle ideal circular orbit.

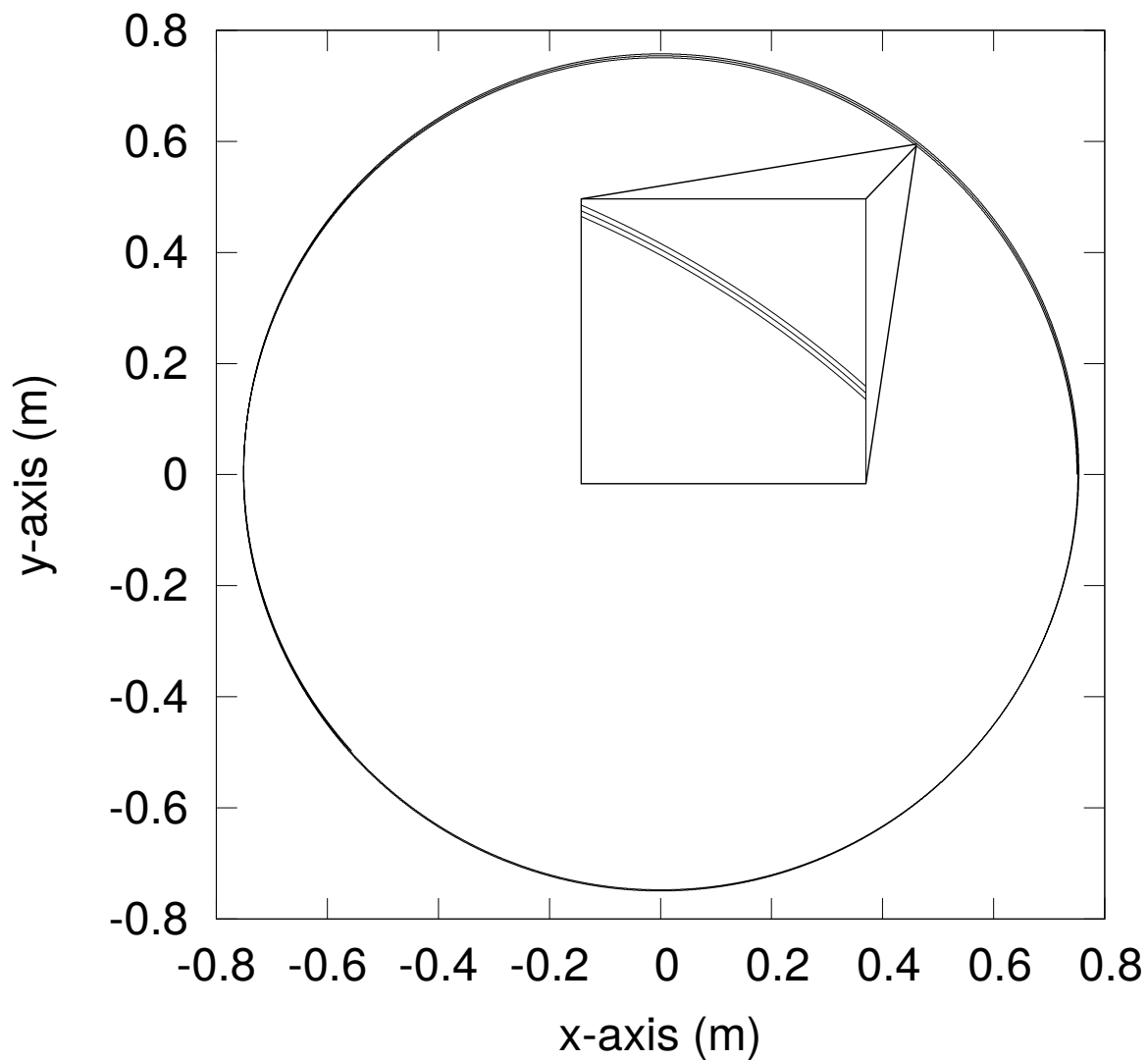


Figure 2.4: Electron trajectory computed with the self-electric field subtracted. The initial conditions are the same as in Fig. 2.3, corresponding to those of a perfectly circular orbit of radius 0.75 m. In this case the suppression of the self-electric field produces a particle trajectory which remains close to the ideal circular trajectory for three orbit periods.

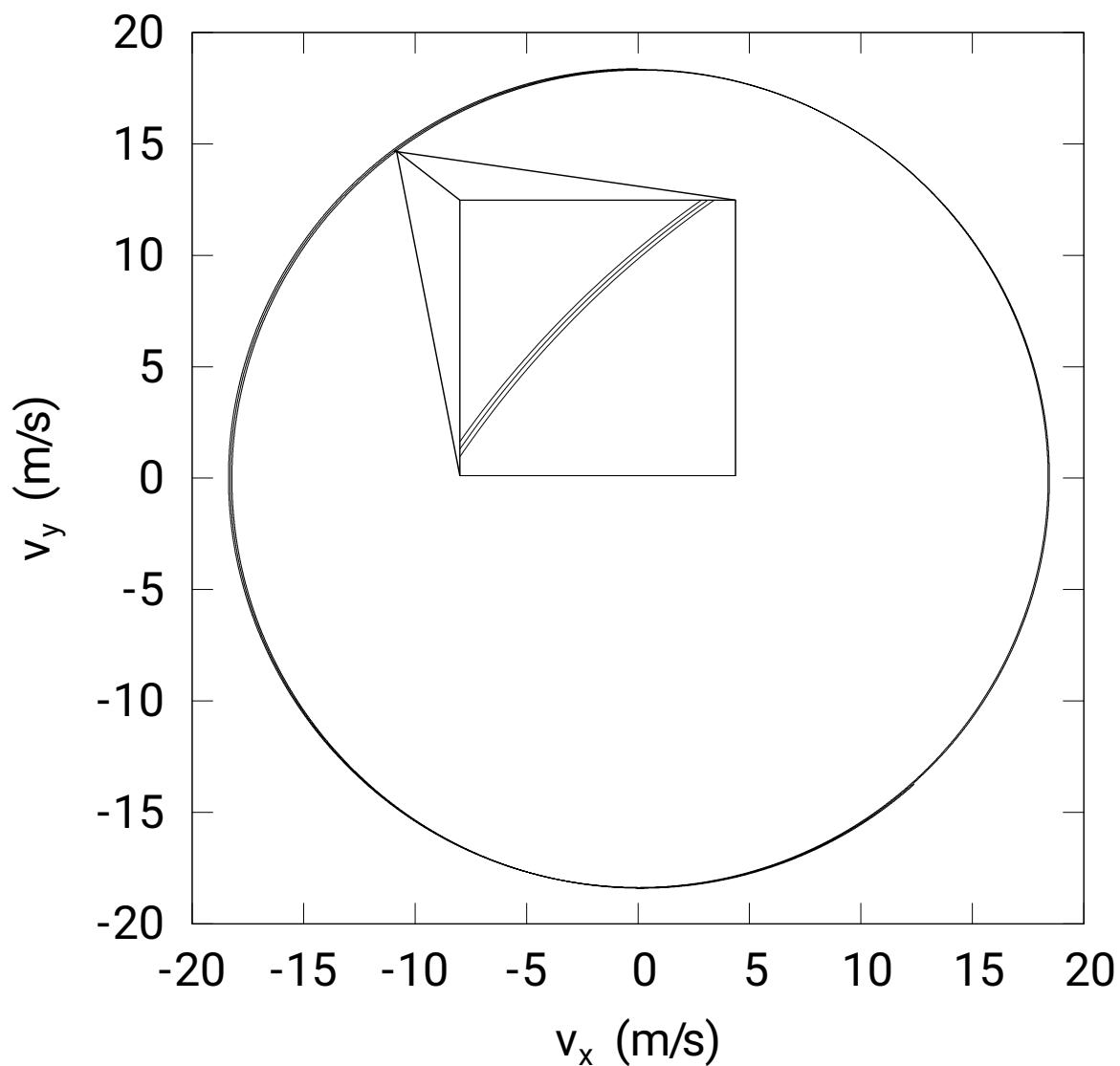


Figure 2.5: Trajectory of the electron in velocity space, with the self-electric field subtracted. As in configuration space (Fig. 2.4), the trajectory remains nearly circular for three complete orbit periods.

below 1.5 %. Variations in the components of the angular momentum vector are shown in Fig. 2.7. The electron kinetic energy should be conserved exactly, the particle trajectory should be perfectly circular, with a constant angular momentum in the z direction. Deviations from these ideal conservation laws result mainly from discretization errors on the simulation grid and, to a lesser extent, from errors in the iterative solution of Poisson’s equation. Compared to the trajectory shown in Fig. 2.3, the removal of the self-field at the electron position results in a considerable improvement in the calculation of the trajectory. Needless to say, that in the presence of the self-force (Fig. 2.3), much stronger variations in the kinetic energy or angular momentum would be found.

2.3.3 TEST ELECTRON IN A PLASMA

We now consider the average magnitude of the acceleration vector experienced by a test electron in a background plasma at different positions along the x axis. A fixed distribution of simulation particles is assumed, resulting from a spatially uniform initialization as described in [86, 72]. That is, simulation particles are distributed randomly in each tetrahedron of the mesh, in numbers proportional to their respective species density and tetrahedron volume. This distribution is then held fixed, and the acceleration of a single electron is calculated along x , as in 2.3.1. We note that the contribution from the test electron is not included in the calculation of volume charge density and resulting electric field, and therefore, there can be no contribution from the self-force in this calculation. The results are plotted in Fig.2.8 for several numbers of simulation particles per Voronoi cell, ranging from 1 to 10^4 , in multiplicative steps of 10. The figure shows a nearly linear decrease in the mean acceleration as a function of the log of the number of particles. In all cases, however, the mean acceleration is well above the self-acceleration of an electron, even when the self-force is

not subtracted. Indeed, even with 10^4 particles per Voronoi cell, accelerations caused by nearby plasma particles are more than four orders of magnitude larger than those associated with the self-force alone. It then follows that in most cases involving many simulation particles per cells self-acceleration should be negligible.

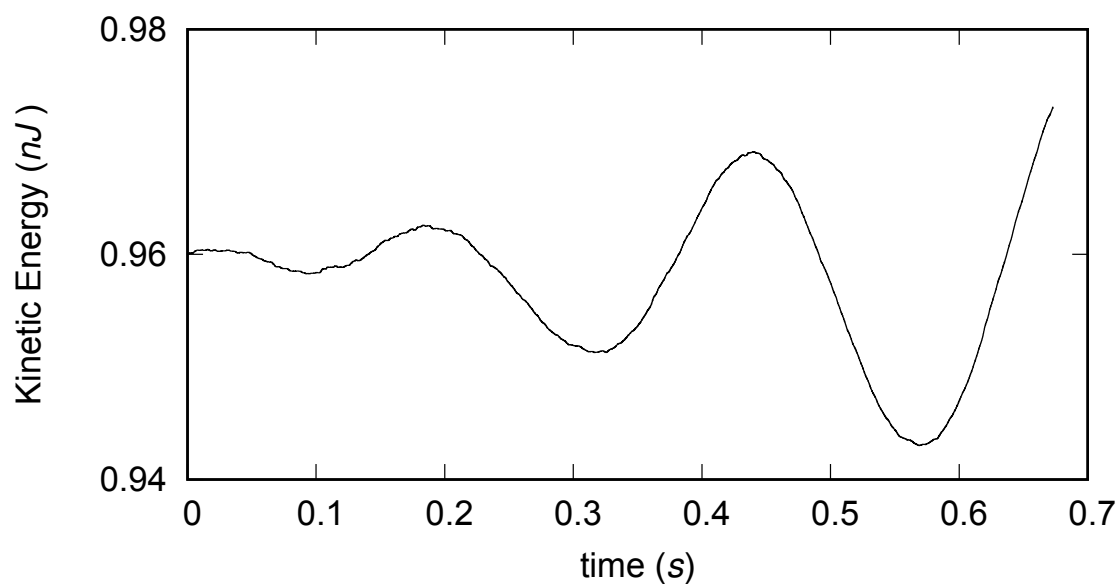


Figure 2.6: Electron kinetic energy computed as a function of time during the electron's first three orbit periods when the self-electric field is subtracted.

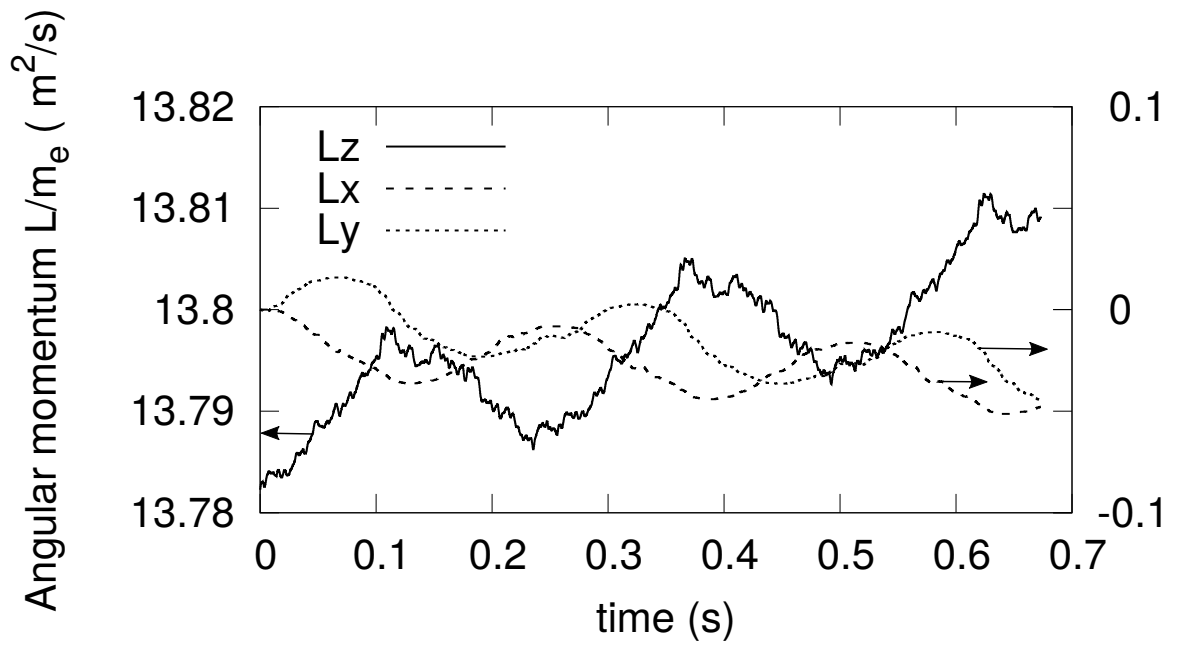


Figure 2.7: Temporal variations in the components of the angular momentum vector during the first three cycles of the electron orbit, when the self-electric field is subtracted. The arrows in the figure point to the ordinates that apply to each curve

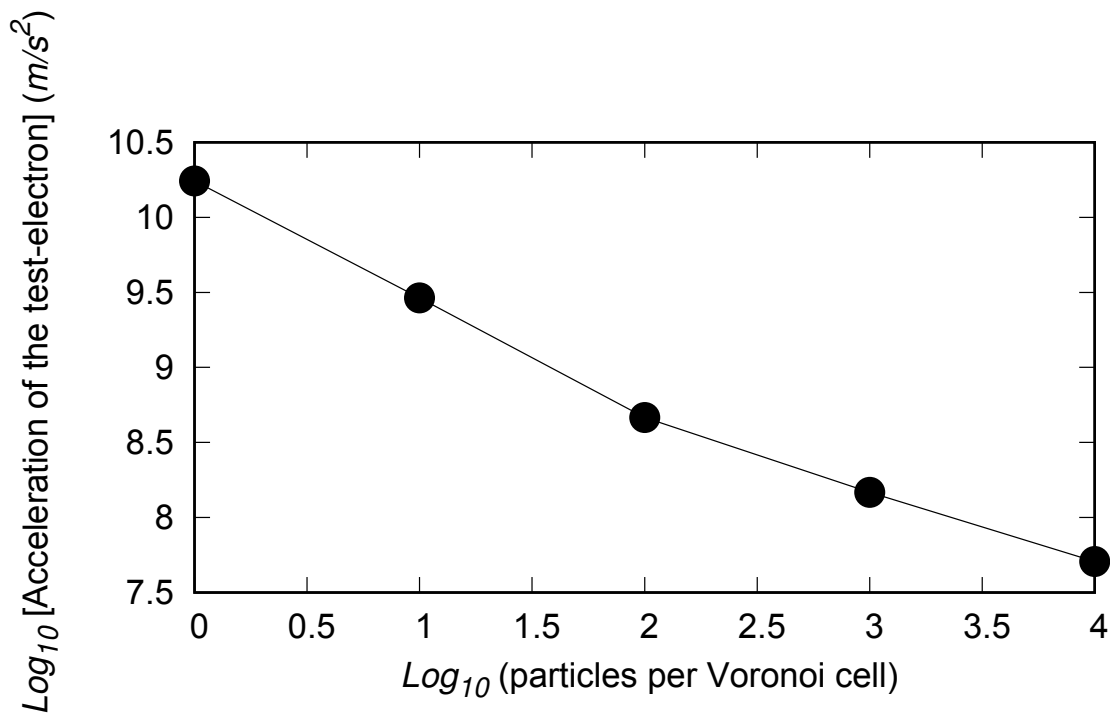


Figure 2.8: Mean magnitude of the acceleration of a test electron in a sphere with plasma, as a function of the logarithm of the number of simulation particles per Voronoi cell. The uncertainty in the mean values of the acceleration is approximately two orders of magnitude lower than the acceleration mean value.

CHAPTER 3.

SWARM FRONT-PLATE AS A PLANAR LANGMUIR PROBE

3.1 INTRODUCTION

The front plates and embedded particle sensor shells that are part of the Electric Field Instrument (EFI) on the Swarm satellites have recently been used as planar Langmuir probes, as an additional diagnostic tool to infer environment parameters. The interpretation of measured currents in terms of the plasma density or incoming flow speed, however, requires a knowledge of the front plate effective cross section A_{eff} . Measurements made under various space plasma conditions have led to the conclusion that this cross section is generally larger than the known geometrical cross section A_{geo} . Interpretations of measurements have thus been made using fixed relative enhancements of A_{geo} ranging from 8 to 17%. In this study results from kinetic simulations are presented, from which the effective cross section can be determined over a range of plasma parameters. These are used to shed light on the physical mechanisms responsible for this enhancement, and construct an empirical fit to the relative enhancement δ , where $A_{eff} = A_{geo}(1 + \delta)$, and in turn enable improvements in the accuracy of inferred plasma parameters

Langmuir probes have been used extensively to diagnose plasma in laboratory and space. The interpretation of probe measurements is based generally on relatively sim-

ple analytic models that cannot account for the many factors affecting measurements. As a result the inference of plasma parameters such as the density and temperature comes with appreciable uncertainties. Indeed many theoretical studies have been made over the years [101, 102, 103, 104, 26, 32], but none is capable to account for all the physical effects affecting probe measurements under realistic conditions. Numerical simulations have been used to compute probe characteristics under increasingly more realistic conditions,[105, 28, 106]. While such simulations can provide useful insight, the computational effort that they require renders them inapplicable for real time interpretation of probe measurements. As a result, probe measurements are generally interpreted using relatively simple analytic expressions, resulting in uncertainties ranging from a few percent, to more than 100 % [33, 107].

The case of interest here is that of the front plate on Swarm when it is used as a planar Langmuir probe. Each of the three Swarm spacecraft is equipped with a front plate in which two Thermal Ion Imagers (TII) are embedded as part of the Electric Field Instrument (EFI) [65]. When the ion imagers are not in operation, the current collected by the front plate and the shells of the TII can be measured at a sample rate of 16 Hz, and the front plate can be used as fixed-bias Langmuir probe [108]. With e being the unit charge and considering that plasma flow is supersonic in the spacecraft reference frame, the relation for the ion current collected when the probe is operated in the ion saturation region (typically $V_{bias} = -3.5$ V)

$$I = env_{\perp}A_{geo} \tag{3.1}$$

provides an approximate relation between the measured current I , the plasma density n and the incoming plasma flow speed v_{\perp} in the direction perpendicular to the plate, given the known geometrical cross section of the plate A_{geo} . Measurements interpreted

on the basis on Eq. 3.1 however, suggest that the geometrical cross section A_{geo} has to be increased by several percent in order to reconcile the results with those of other independent measurements [109]. Indeed increases in the effective front plate cross section by 8 up to 17 % were suggested to reduce the discrepancies with other measurements. While a step in the right direction, these ad hoc increases suggest that a closer look should be given to explain them in terms of underlying physical processes. The goal of this work is therefore to carry out simulations to quantitatively determine the relative enhancement

$$\delta = \frac{A_{eff} - A_{geo}}{A_{geo}} = \frac{I}{env_{\perp}A_{geo}} - 1 \quad (3.2)$$

over a range of relevant ionospheric plasma parameters, and from there, better understand the physical processes at play, and construct an empirical model to approximate δ under different space environment conditions.

The remainder of the study briefly describes the computational approach used to carry out the simulations, followed by a presentation of our results and the construction of an empirical model for calculating the relative enhancement δ . Finally, Section 3.5 contains a summary of our findings and some concluding remarks.

3.2 METHODOLOGY

The current collected by a Swarm front plate is calculated for several ionospheric environment conditions, by carrying out kinetic simulations with PTetra [71, 72]. In the simulations a reduced Swarm geometry shown in Fig. 3.1 is considered, which accounts for a segment of the main spacecraft body, the front plate, the shells covering the thermal ion imagers, and the two spherical Langmuir probes. While greatly simplified, the assumption is that this geometry is sufficient to study the interaction between the front plate and incoming supersonic plasma when the front plate is bi-

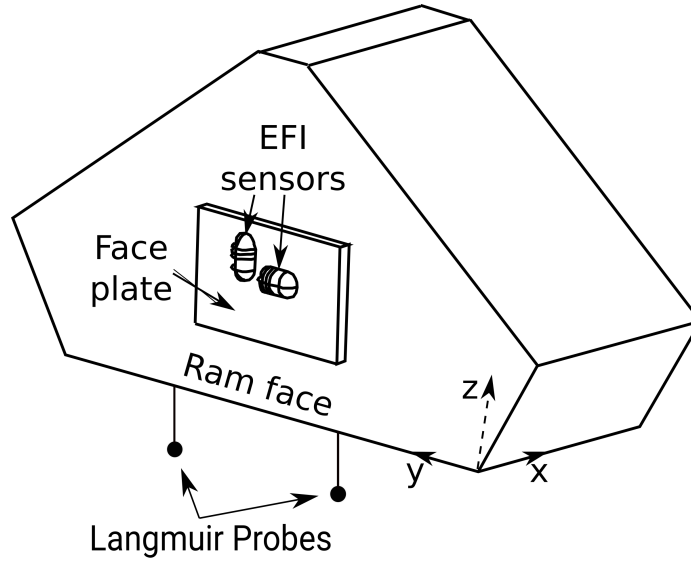


Figure 3.1: Illustration of a simplified Swarm geometry with front plate and TII shells. In the simulations the front plate is a rectangle with an area of $351 \times 229 \text{ mm}^2$. The thickness of the plate is 3.175 mm while the separation between the plate and the satellite bus is 21.825 mm. The Langmuir probe radius is 4 mm. The schematic of the spherical probes in the figure are not to scale.

ased sufficiently negatively with respect to the spacecraft bus. In the simulations, both electron and ion species are treated fully kinetically using the Particle-In-Cell (PIC) approach, and the electric sheath surrounding the front plate and bus are calculated self-consistently. Simulations are made using approximately 163 to 549 million particles in an unstructured adaptive tetrahedral mesh with numbers of elements (tetrahedra) from approximately 2.1 to 4.6 million corresponding to a range of statistical weight from 236 to 8532. The simulation domain is a cylinder of approximately 7 m long, with a radius of approximately 1 m. Several cases are considered in which the temperature, the density, the plasma flow velocity, the ion composition, and the satellite floating potential are varied. In this study, a fixed plasma flow velocity of 7673 m/s from the ram direction is considered in most cases. Simulations have been

made by adding transverse (in directions parallel to the plate) flow velocities up to 1000 m/s, in which the relative enhancement remains the same within two significant figures. For that reason, only simulations with a flow velocity in the direction perpendicular to the plate are considered. Simulations with variations to the plasma flow velocity in the along-track direction associated with ionospheric winds of ± 500 m/s were done in some cases. Different ion compositions have also been considered including pure O^+ plasma and O^+ with representative fractions of lighter minority ions as obtained from the International Reference Ionosphere (IRI) model [110]. The strength and length of the electric sheath surrounding the front plate has an important role in ion collection. The sheath around the front plate depends on the potential of the plate with respect to the background plasma, $V = V_{bias} + V_f$. Here, V_{bias} is the plate bias voltage with respect to the spacecraft. V_f is the spacecraft floating potential with respect to the plasma, and V is then the front plate voltage with respect to the background plasma.

Here and in the remainder of the thesis, the convention is that “voltage” always refers to the background plasma, and “bias voltage”, to the spacecraft ground.

Since the front plate is typically operated at a fixed bias voltage of -3.5 V (V_{bias}), different floating potentials (V_f) were assumed in order to account for different possible plate potentials with respect to surrounding plasma (-2 V, -1 V, and one calculated self-consistently from simulations). Typical values for the spacecraft floating potential estimated from in situ measurements are around -2 V. Simulations have been made with and without the inclusion of a representative geomagnetic field, and it was found that for the supersonic flows ($v \sim 7673$ m/s) considered and the relatively large ion gyroradii (~ 1 m for H^+ ions and ~ 4 m for O^+) the inclusion of magnetic fields had no significant effect. For simplicity, photoelectron emission and secondary

electron emission are not accounted for. This simplification should be valid when the spacecraft is on the night side of their orbit, or in higher density regions of the ionosphere, where collected ion currents exceed those from photoelectron emission. In each case the effective cross section

$$A_{eff} = \frac{I}{env_{\perp}} \quad (3.3)$$

has been calculated, and the relative enhancement δ has been determined from 3.2. Table 3.1 summarizes the cases considered, with the corresponding relative enhancements δ .

The table shows, consistently with suggestions from observations, that the effective plate cross section is indeed larger than the geometrical cross section, corresponding to positive values of δ . We also note that the values of the relative enhancements are in the range 2.84 to 23.42 %, consistent with the empirical values of 8 to 17 % mentioned above, and used when processing front plate collected currents. The next step consists of constructing an empirical analytic expression that can approximate the tabulated values of δ in the range of parameters considered. Referring to Figs. 3.3 and 3.4, the enhancement in the collected ion currents is seen to be caused by electric fringe effects at the plate perimeter, whereby electric fields associated with curved equipotential surfaces near the edge shown in Fig. 3.2, deflect incident ions towards the plate. Variations in the along-track plasma flow velocity modify the kinetic energy of incoming ions. More energetic ions are deflected less by the fringe electric fields at the plate, while less energetic ions are deflected more. This results in lower and higher relative enhancements respectively as can be seen in table 3.1. The electric potential profile shown in Fig. 3.2 corresponds to the case in Table 3.1 for which enhancement is at 21.25 %, and plasma density is at $n = 1 \times 10^{10} \text{m}^{-3}$. The floating potential was

Table 3.1 Part I

n $10^{10}m^{-3}$	T_e eV	T_i eV	m_{eff} amu	λ_D mm	v_{\perp} m/s	V V	I μA	δ_{sim} $\%$	ϵ $\%$
3.16	0.070	0.070	7.35	11.06	7673	-3.70	3.504	12.23	0.8
3.16	0.070	0.070	7.35	11.06	7673	-4.50	3.537	13.28	0.9
3.16	0.070	0.070	7.35	11.06	7673	-5.50	3.575	14.49	0.6
10.00	0.070	0.068	5.85	6.22	7673	-3.70	10.732	8.61	0.5
10.00	0.070	0.068	5.85	6.22	7673	-4.50	10.824	9.54	1.0
10.00	0.070	0.068	5.85	6.22	7673	-5.50	10.903	10.34	1.1
31.6	0.070	0.070	4.10	3.50	7673	-3.70	33.433	7.07	0.8
31.6	0.070	0.070	4.10	3.50	7673	-4.50	33.629	7.70	1.3
31.6	0.070	0.070	4.10	3.50	7673	-5.50	33.879	8.50	1.7
63.2	0.082	0.079	13.71	2.68	7673	-3.73	64.227	2.84	1.7
63.2	0.082	0.079	13.71	2.68	7673	-4.50	64.549	3.36	1.0
63.2	0.082	0.079	13.71	2.68	7673	-5.50	64.936	3.98	0.3
1.00	0.156	0.116	8.29	29.36	7673	-4.01	1.182	19.58	1.3
1.00	0.156	0.116	8.29	29.36	7673	-4.50	1.187	20.15	0.6
1.00	0.156	0.116	8.29	29.36	7673	-5.50	1.198	21.25	1.0
3.16	0.140	0.113	11.40	15.65	7673	-3.95	3.451	10.53	0.0
3.16	0.140	0.113	11.40	15.65	7673	-4.50	3.477	11.35	0.4
3.16	0.140	0.113	11.40	15.65	7673	-5.50	3.519	12.70	0.7
10.0	0.140	0.112	12.99	8.80	7673	-3.94	10.488	6.14	0.8
10.0	0.140	0.112	12.99	8.80	7673	-4.50	10.551	6.78	0.3
10.0	0.140	0.112	12.99	8.80	7673	-5.50	10.656	7.84	0.4
31.6	0.140	0.089	15.88	4.95	7673	-3.94	32.355	3.61	1.4
31.6	0.140	0.089	15.88	4.95	7673	-4.50	32.490	4.05	0.9
31.6	0.140	0.089	15.88	4.95	7673	-5.50	32.710	4.75	0.1
3.16	0.210	0.120	12.57	19.16	7673	-4.22	3.461	10.83	0.2
3.16	0.210	0.120	12.57	19.16	7673	-4.50	3.473	11.23	0.4
3.16	0.210	0.120	12.57	19.16	7673	-5.50	3.513	12.52	0.7
10.0	0.220	0.107	11.28	11.03	7673	-4.25	10.579	7.06	0.4
10.0	0.220	0.107	11.28	11.03	7673	-4.50	10.604	7.31	0.2
10.0	0.220	0.107	11.28	11.03	7673	-5.50	10.699	8.27	0.4
10.0	0.280	0.121	15.96	12.44	7673	-4.49	10.535	6.61	0.3
10.0	0.280	0.121	15.96	12.44	7673	-5.50	10.635	7.63	0.4

Table 3.1 Part II									
n	T_e	T_i	m_{eff}	λ_D	v_{\perp}	V	I	δ_{sim}	ϵ
$10^{10}m^{-3}$	eV	eV	amu	mm	m/s	V	μA	$\%$	$\%$
3.16	0.070	0.070	7.35	11.06	8173	-4.50	3.730	12.16	1.0
3.16	0.070	0.070	7.35	11.06	8173	-5.50	3.768	13.31	1.7
10.00	0.070	0.068	5.85	6.22	8173	-4.50	11.440	8.69	0.4
10.00	0.070	0.068	5.85	6.22	8173	-5.50	11.530	9.54	0.6
1.00	0.156	0.116	8.29	29.36	8173	-4.50	1.245	18.33	0.3
1.00	0.156	0.116	8.29	29.36	8173	-5.50	1.256	19.41	1.7
10.0	0.280	0.121	15.96	12.44	8173	-4.50	11.144	5.88	0.9
10.0	0.280	0.121	15.96	12.44	8173	-5.50	11.246	6.85	0.1
3.16	0.070	0.070	7.35	11.06	7173	-4.50	3.345	14.62	1.7
3.16	0.070	0.070	7.35	11.06	7173	-5.50	3.383	15.90	1.4
10.00	0.070	0.068	5.85	6.22	7173	-4.50	10.202	10.44	1.6
10.00	0.070	0.068	5.85	6.22	7173	-5.50	10.289	11.38	1.7
1.00	0.156	0.116	8.29	29.36	7173	-4.50	1.129	22.89	1.7
1.00	0.156	0.116	8.29	29.36	7173	-5.50	1.140	23.42	0.0
10.0	0.280	0.121	15.96	12.44	7173	-4.50	9.924	7.43	0.3
10.0	0.280	0.121	15.96	12.44	7173	-5.50	10.022	8.49	1.0

Table 3.1: List of simulation parameters with computed front plate collected currents, relative enhancement δ and absolute deviations $\epsilon = |\delta_{sim} - \delta_{model}|$ in predicted enhancements obtained with model equation 3.4. The smallest and largest values of δ_{sim} , and the largest relative errors ϵ are in bold.

set to $-2 V$, whereas the plate is biased to $-3.5 V$ with respect to the spacecraft, thus, the plate is biased to $-5.5 V$ with respect to background plasma. The particle trajectories in Fig. 3.3 and 3.4 were calculated using the electric field obtained from the equipotential surfaces shown in Fig. 3.2. In Fig. 3.3, twelve plasma particles, six H^+ and six O^+ , were injected from the boundary towards the plate with velocities of magnitude equal to the ram velocity plus or minus their respective thermal speed. In all cases, particles would miss the plate in the absence of the sheath electric field. The presence of the electric field directed toward the plate, however, deflects a fraction of these incoming particles to the edge of the plate where they add to the collected current and thus contribute to the relative enhancement of the front plate effective

cross section. Similarly in Fig. 3.4, thirty eight particles (nineteen H^+ and nineteen O^+) injected at the upstream boundary, from different angles with speeds equal to the ram speed plus their respective species thermal speed. All particles are aimed a few centimeters above the front-plate and would miss the plate in the absence of the sheath electric field but, as seen in the figure, (in the presence of the field,) many are deflected to the plate where they add to the collected ion current.

3.3 PHYSICAL MODEL FOR THE COLLECTED CURRENT

The next step consists of constructing an empirical analytic expression that can approximate the tabulated values of δ in the range of parameters considered. Referring to Figs. 3.3 and 3.4, the enhancement in the collected ion currents is seen to be caused by electric fringe effects at the plate perimeter, whereby electric fields associated with curved equipotential surfaces near the edge shown in Fig. 3.2, deflect incident ions towards the plate.

It was found that the relative enhancements δ in Table 3.1 can be approximated with good accuracy analytically. Several expressions with adjustable parameters have been tried, and the one that was found to best reproduce our computed enhancement is given by:

$$I = env_{\perp} A_{geo} \left[1 + \frac{\alpha P \lambda_D}{A_{geo}} \left(1 - \beta \frac{eV}{\frac{1}{2} m_{eff} v_{\perp}^2} - \gamma \frac{eV}{kT_e} - \frac{\zeta}{eV} \frac{e^2}{4\pi\epsilon_0 \lambda_D} \right) \right], \quad (3.4)$$

where P is the perimeter of the plate (the sum of the length of all sides), V is the plate potential with respect to background plasma, T_e is the electron temperature, and the electron Debye length λ_D is given by $(\epsilon_0 k T_e / e^2 n)^{1/2}$. α , β , γ and ζ are fit parameters. The effective thickness of the deflecting region around the plate is taken to be proportional to the scaled electron Debye length λ_D . In Eq. 3.4, the term $(eV) / (\frac{1}{2} m_{eff} v_{\perp}^2)$ is consistent with the fact that less energetic ions are deflected more

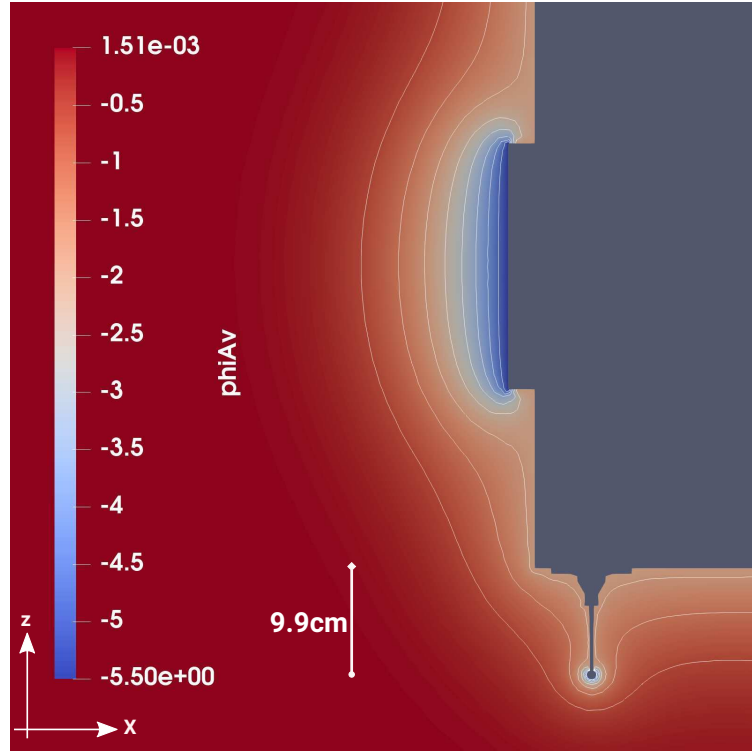


Figure 3.2: Curved equipotentials around the front plate and Langmuir probe. The color bar labeled as ϕ_{Av} , represents the electric potential averaged in time at steady state.

by sheath electric fields, and that for a given incident particle energy, larger attractive voltages lead to stronger particle deflections. The term multiplying γ accounts for the increase in the sheath thickness surrounding the plate, as the ratio eV/kT_e increases, while the one multiplying ζ was found purely empirically to improve the accuracy of the fit. In Eq. 3.4, the effective mass is defined by

$$\frac{1}{m_{eff}} = \sum_{i=1}^N \frac{n_i}{n_{tot}} \frac{1}{m_i} \quad (3.5)$$

where, for a multiple-ion species plasma, n_i is the density of species i and n_{tot} is the total ion density. From 3.4 and the definition of δ in 3.2, it follows that the relative

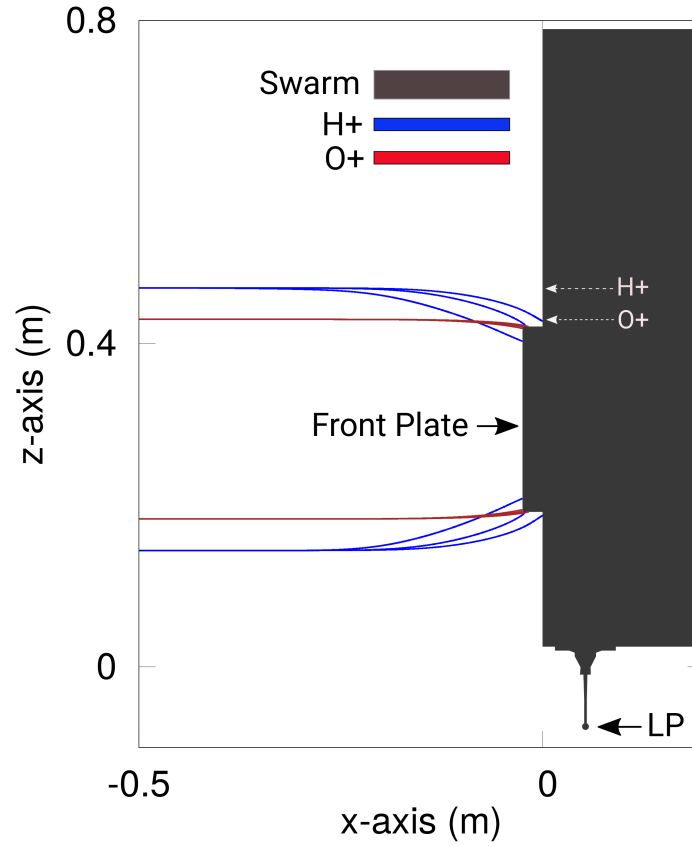


Figure 3.3: Ion trajectories deflected near the front plate, due to curved equipotentials around the perimeter. Both species are aimed slightly below or above (dashed arrows) the plate with velocities exactly from the ram direction. Three speeds are considered corresponding to v_{ram} , and $v_{ram} \pm v_{th}$ with $v_{th} = \sqrt{2kT/m}$ being the species thermal speed. Particles with the lower speed ($v_{ram} - v_{th}$) are deflected the most, and the ones with the higher speed ($v_{ram} + v_{th}$) are deflected the least.

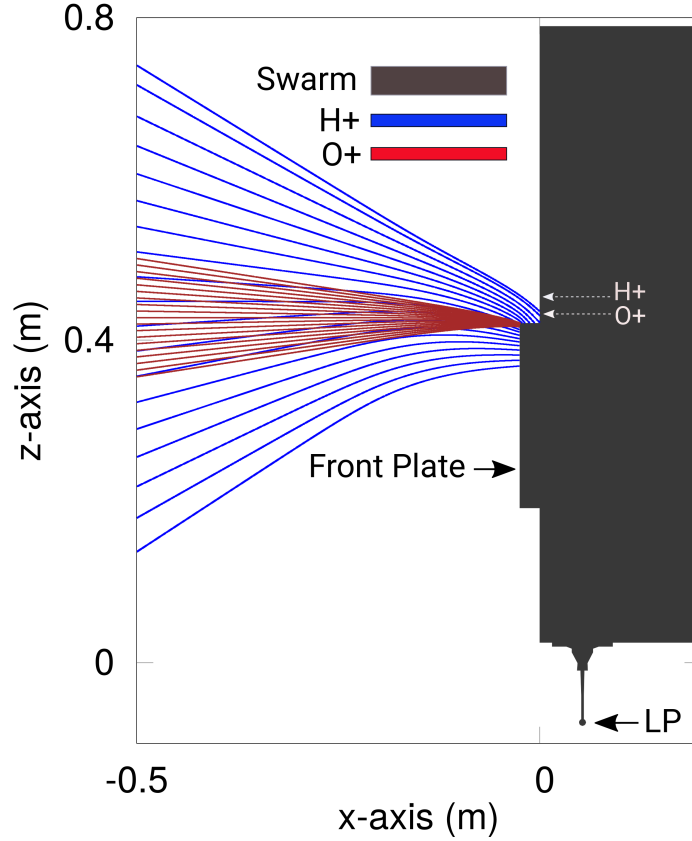


Figure 3.4: O^+ and H^+ ion trajectories deflected near the front plate due to curved equipotentials around the perimeter. In all cases, the magnitude of the incident velocity is equal to $\sqrt{v_{ram}^2 + v_{th}^2}$, where $v_{th} = \sqrt{2kT/m}$ is the ion thermal speed. The incoming particles have different incident angle. The arrows show where H^+ and O^+ ions would impact if they were undeflected.

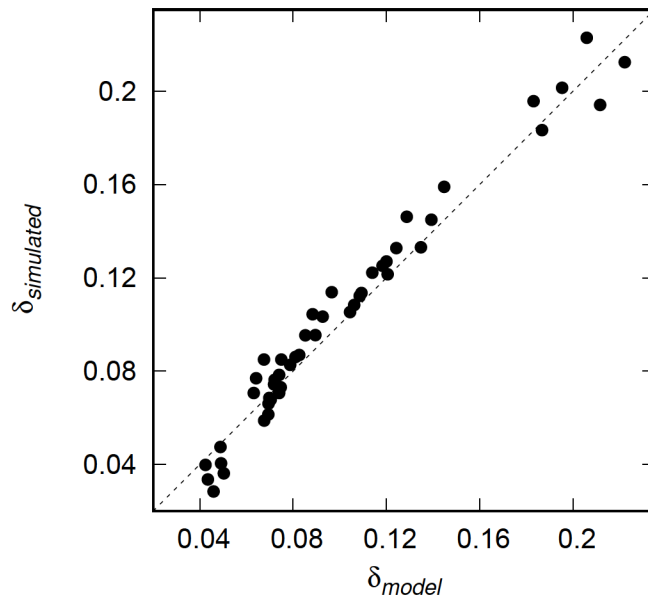


Figure 3.5: Correlation between model predicted relative enhancement δ_{model} and values computed from simulations δ_{sim} . Dashed line: perfect one-to-one correlation.

enhancement in this model is

$$\delta_{model} = \frac{\alpha P \lambda_D}{A_{geo}} \left(1 - \beta \frac{eV}{\frac{1}{2} m_{eff} v_{\perp}^2} - \gamma \frac{eV}{kT_e} - \frac{\zeta}{eV} \frac{e^2}{4\pi\epsilon_0\lambda_D} \right). \quad (3.6)$$

The four fitting parameters α , β , γ , and ζ in Eq. 3.6 are adjusted so as to minimize the maximum absolute error $|\delta_{sim} - \delta_{model}|$. The optimal values are found to be $\alpha = 0.06929$, $\beta = 1.40573$, $\gamma = 0.08045$, and $\zeta = 77.97608 \times 10^6$ for which the maximum absolute error is 1.7 %. The correlation between simulated and model predicted relative enhancements is shown in Fig. 3.5, and the error in the predictions, defined by $|\delta_{sim} - \delta_{model}|$ are listed in Table 3.1 for reference. The scatter in this plot may seem disappointing, but as shown below, all other relevant parameters being known, the model does allow an estimate of the density within approximately 2 %.

This indeed follows, from Eq. 3.3 from which

$$\begin{aligned} n &= \frac{I}{A_{eff}ev_{\perp}} = \frac{I}{A_{geo}(1 + \delta_{sim})ev_{\perp}} \\ &= \frac{I}{A_{geo}(1 + \delta_{model} \pm \epsilon)ev_{\perp}}, \end{aligned} \quad (3.7)$$

where ϵ is the error in the model prediction. The variation in n associated with an uncertainty of $\pm\epsilon$ is then

$$\begin{aligned} \Delta n &= \frac{1}{2} \frac{I}{A_{geo}ev_{\perp}} \left(\frac{1}{1 + \delta_{model} - \epsilon} - \frac{1}{1 + \delta_{model} + \epsilon} \right) \\ &= \frac{I}{A_{geo}ev_{\perp}} \frac{\epsilon}{(1 + \delta)^2 - \epsilon^2} = \frac{n(1 + \delta)}{(1 + \delta)^2 - \epsilon^2} \times \epsilon, \end{aligned} \quad (3.8)$$

from which

$$\frac{\Delta n}{n} = \frac{(1 + \delta)}{(1 + \delta)^2 - \epsilon^2} \times \epsilon. \quad (3.9)$$

Given the relative enhancements and errors listed in Table 3.1, the fraction multiplying ϵ can be seen to be lower than unity in all cases. It then follows that the relative error in the inferred density is at most ϵ . Taking the largest error in the table we conclude that, all other parameters being known, equation 3.4 can be used to predict the plasma density with 2 % accuracy over the simulation conditions considered.

3.4 DISCUSSION

It was shown in Sec. 3.3 that, within the range of parameters considered, the empirical formula 3.4 can be used to determine the plasma density within ~ 1.7 % accuracy, given accurate numerical values of other parameters. This can be done explicitly by solving for n in terms of the other parameters in 3.4. After some algebra it follows

that

$$\begin{aligned}
 n &= \left\{ \left[-\frac{\alpha P}{A_{geo}} \sqrt{\frac{\epsilon_0 k T_e}{e^2}} \left(1 - \beta \frac{eV}{\frac{1}{2} m_{eff} v_{\perp}^2} - \gamma \frac{eV}{k T_e} \right) \right. \right. \\
 &+ \left[\left(\frac{\alpha P}{A_{geo}} \right)^2 \frac{\epsilon_0 k T_e}{e^2} \left(1 - \beta \frac{eV}{\frac{1}{2} m_{eff} v_{\perp}^2} - \gamma \frac{eV}{k T_e} \right)^2 \right. \\
 &- \left. \left. 4 \left(1 - \frac{\alpha P}{A_{geo}} \frac{\zeta}{eV} \frac{e^2}{4\pi\epsilon_0} \right) \left(\frac{I}{e v_{\perp} A_{geo}} \right) \right]^{\frac{1}{2}} \right] \\
 &\times \left. \frac{1}{2} \left(1 - \frac{\alpha P}{A_{geo}} \frac{\zeta}{eV} \frac{e^2}{4\pi\epsilon_0} \right)^{-1} \right\}^2. \tag{3.10}
 \end{aligned}$$

where the fit parameters α , β , γ , and ζ are determined in the previous section. The point to note here is that a model based on equation 3.10, or equivalently on 3.7, depends explicitly on four unknown plasma parameters. These are the electron temperature T_e , the plasma speed v_{\perp} in the ram direction, the effective ion mass m_{eff} and the spacecraft floating potential V_f . The dependence on V_f follows from the fact that the plate potential V with respect to background plasma is the sum of the floating potential and the known bias potential V_{bias} : $V = V_f + V_{bias}$. Therefore while it is possible in principle to use 3.7 to infer the density accurately in the parameter space considered, the skill of the model would depend on the accuracy with which other parameters can be determined. It is not the intent in this study to discuss other measurements made on Swarm, but suffice it to mention that the electron temperature, the density, and satellite floating potential, can in principle be obtained from the two spherical Langmuir probes [111, 65]. However the effective mass (or relative ion densities) and the plasma flow velocity from the ram direction are not measured independently. It therefore follows that the interpretation of measurements of the collected ion current by the front plate, might involve more unknown plasma parameters than there are independent measurements.

In closing it is interesting to compare values obtained from our model equations 3.6 with values inferred using fixed relative enhancements $\delta = 17\%$, 12% or 8% . In Table 3.2 comparisons are made between relative errors in densities based on these three fixed values, and from our model.

While the relative error resulting from a fixed δ can be smaller in some cases, the maximum relative error (in bold) is appreciably less when our model is used, which implies that, in the range of parameters considered, more accurate inference of the density can be made by using equation 3.7 or equivalently 3.10. The results shown in the previous section confirm that an enhancement in the collection area of the front plate as planar Langmuir probe exists. Our proposed model for the enhancement depends on the geometry of the plate, the percentage of light ions in the plasma and their kinetic energy, as well as the electric sheath surrounding the front plate.

Table 3.2 Part I									
n $10^{10}m^{-3}$	T_e eV	T_i eV	m_{eff} amu	λ_D mm	v_{\perp} m/s	$\delta_{17\%}$ %	$\delta_{12\%}$ %	$\delta_{8\%}$ %	δ_{model} %
3.16	0.070	0.070	7.35	11.06	7673	-4.2	+0.2	+3.8	+0.7
3.16	0.070	0.070	7.35	11.06	7673	-3.3	+1.1	+4.7	+0.7
3.16	0.070	0.070	7.35	11.06	7673	-2.2	+2.2	+5.7	+0.5
10.00	0.070	0.068	5.85	6.22	7673	-7.7	-3.1	+0.6	+0.5
10.00	0.070	0.068	5.85	6.22	7673	-6.8	-2.2	+1.4	+0.9
10.00	0.070	0.068	5.85	6.22	7673	-6.0	-1.5	+2.2	+1.0
31.6	0.070	0.070	4.10	3.50	7673	-9.3	-4.6	-0.9	+0.7
31.6	0.070	0.070	4.10	3.50	7673	-8.6	-4.0	-0.3	+1.2
31.6	0.070	0.070	4.10	3.50	7673	-7.8	-3.2	+0.5	+1.6
63.2	0.082	0.079	13.71	2.68	7673	-13.7	-8.9	-5.0	-1.7
63.2	0.082	0.079	13.71	2.68	7673	-13.2	-8.4	-4.5	-0.9
63.2	0.082	0.079	13.71	2.68	7673	-12.5	-7.7	-3.9	-0.3
1.00	0.156	0.116	8.29	29.36	7673	+2.2	+6.3	+9.7	+1.3
1.00	0.156	0.116	8.29	29.36	7673	+2.6	+6.8	+10.1	+0.5
1.00	0.156	0.116	8.29	29.36	7673	+3.5	+7.6	+10.9	-0.9
3.16	0.140	0.113	11.40	15.65	7673	-5.9	-1.3	+2.3	+0.1
3.16	0.140	0.113	11.40	15.65	7673	-5.1	-0.6	+3.0	+0.4
3.16	0.140	0.113	11.40	15.65	7673	-3.8	+0.6	+4.2	+0.6
10.0	0.140	0.112	12.99	8.80	7673	-10.2	-5.5	-1.8	-0.8
10.0	0.140	0.112	12.99	8.80	7673	-9.6	-4.9	-1.1	-0.3
10.0	0.140	0.112	12.99	8.80	7673	-8.5	-3.9	-1.5	+0.4
31.6	0.140	0.089	15.88	4.95	7673	-12.9	-8.1	-4.2	-1.4
31.6	0.140	0.089	15.88	4.95	7673	-12.4	-7.6	-3.8	-0.8
31.6	0.140	0.089	15.88	4.95	7673	-11.7	-6.9	-3.1	-0.1
3.16	0.210	0.120	12.57	19.16	7673	-5.6	-1.1	+2.6	+0.2
3.16	0.210	0.120	12.57	19.16	7673	-5.2	-0.7	+2.9	+0.4
3.16	0.210	0.120	12.57	19.16	7673	-4.0	+0.5	+4.1	+0.6
10.0	0.220	0.107	11.28	11.03	7673	-9.3	-4.6	-0.9	-0.3
10.0	0.220	0.107	11.28	11.03	7673	-9.0	-4.4	-0.6	-0.2
10.0	0.220	0.107	11.28	11.03	7673	-8.1	-3.4	+0.3	+0.4
10.0	0.280	0.121	15.96	12.44	7673	-9.7	-5.1	-1.3	-0.3
10.0	0.280	0.121	15.96	12.44	7673	-8.7	-4.1	-0.3	+0.4

n $10^{10}m^{-3}$	T_e eV	T_i eV	m_{eff}	λ_D mm	v_{\perp} m/s	$\delta_{17\%}$ %	$\delta_{12\%}$ %	$\delta_{8\%}$ %	δ_{model} %
3.16	0.070	0.070	7.35	11.06	8173	-4.3	+0.1	+3.7	+0.1
3.16	0.070	0.070	7.35	11.06	8173	-3.3	+1.2	+4.7	+0.2
10.00	0.070	0.068	5.85	6.22	8173	-7.7	-3.0	+0.6	+0.4
10.00	0.070	0.068	5.85	6.22	8173	-6.8	-2.2	+1.4	+0.6
1.00	0.156	0.116	8.29	29.36	8173	+1.2	+5.3	+8.7	-0.3
1.00	0.156	0.116	8.29	29.36	8173	+2.0	+6.2	+9.5	-1.6
10.0	0.280	0.121	15.96	12.44	8173	-10.5	-5.8	-2.0	-0.8
10.0	0.280	0.121	15.96	12.44	8173	-9.5	-4.8	-1.1	-0.1
3.16	0.070	0.070	7.35	11.06	7173	-2.1	+2.3	+5.8	+1.6
3.16	0.070	0.070	7.35	11.06	7173	-0.9	+3.3	+6.8	+1.3
10.00	0.070	0.068	5.85	6.22	7173	-5.9	-1.4	+2.2	+1.5
10.00	0.070	0.068	5.85	6.22	7173	-5.0	-5.5	+3.0	+1.6
1.00	0.156	0.116	8.29	29.36	7173	+4.2	+8.4	+11.7	+1.5
1.00	0.156	0.116	8.29	29.36	7173	+5.2	+9.3	+13.0	-0.1
10.0	0.280	0.121	15.96	12.44	7173	-8.9	-4.2	-0.5	+0.2
10.0	0.280	0.121	15.96	12.44	7173	-7.8	-3.2	+0.5	+0.9

Table 3.2: List of relative errors in the densities inferred with a fixed relative enhancement δ of 0.17, $\delta_{17\%}$, 0.12, $\delta_{12\%}$, 0.08, $\delta_{8\%}$. The rightmost column gives the relative errors δ_{model} resulting from using our model. All relative errors are in percent. Positive and negative values of δ correspond, respectively, to model overestimates and underestimates. Maximum relative errors are in bold.

3.5 SUMMARY

An empirical expression for the current collected by the Swarm front-plate is proposed which reproduces the enhancement of the Swarm EFI front plate as a function of plasma environment parameters. This expression in turn is meant to improve the interpretation of ion current collected by the plate when it is operated as a planar Langmuir probe. The analytical expression for the relative enhancement δ is constructed to best represent the simulation results, and account for the deflection of incoming ions to the plate by fringe electric fields around the plate perimeter. The

four fit parameters in the model were adjusted by minimizing the maximum absolute error in computed relative enhancements δ_{sim} over a range of parameters of relevance to mid latitude ionospheric plasma. Given accurate values for the other parameters, our model can be used to infer the density from measured collected currents, with an accuracy of approximately 2 % in the range of parameters considered. The skill of the model was also compared with predictions making use of fixed (independent of plasma parameters) values of δ . In all cases the maximum relative error computed for the forty eight cases considered, was significantly lower when using δ predicted with our model. It was noted however that, while our model can infer the density from measurements with good accuracy, it does rely on other environment parameters being known with sufficiently good accuracy. Those parameters include the electron temperature, the flow velocity in the ram direction, the effective ion mass, and the spacecraft floating potential. This study is a first step at understanding and quantifying the physical causes of the observed enhancement in the Swarm front plate effective cross section. The longer term goal being to improve the interpretation of measured currents collected by the front plate, in order to better infer the density and possibly other plasma parameters, can be pursued with an analysis including more physical processes, and possibly cover a broader range of space environment conditions. Such processes would include photoelectron emission from the satellite, and possibly the front plate when the satellite is exposed to solar radiation. Photoelectron emission from the plate would likely increase the effective positive current collected, and thereby contribute to further enhancing the effective cross section. This enhancement in turn would depend on the orientation of the satellite with respect to the sun and, given electron's relatively small gyro-radii, on the strength and direction of the magnetic field. The construction of such a detailed model is beyond the scope of this first exploratory study, and it is intended for future studies.

CHAPTER 4.

SWARM SPHERICAL LANGMUIR PROBES

4.1 INTRODUCTION

Probe characteristics in space missions are generally interpreted analytically in terms of plasma parameters using theoretical models. These analytic approaches, however, not always account for actual measurement conditions. Consequently, inferred parameters may come with significant uncertainties. An alternative to analytic models to interpret probe measurements consists of using kinetic simulations as introduced in Chapter 2. An advantage of using PIC simulations over analytic models, is that plasma interaction under more realistic conditions can be taken into account. However, using kinetic simulations require considerably more time and computational resources than analytic formulas. A direct use of PIC simulations to interpret in situ measurements in space missions is impractical. Kinetic simulations can be used on the other hand, to simulate space plasma interactions for representative cases and from there, test, develop, or correct analytic models to improve the interpretation of probe measurements in terms of plasma parameters.

In this chapter the objective is to investigate the particle collection of the Swarm spherical Langmuir probes under more realistic ionospheric plasma conditions than possible with analytic theories, to assess the uncertainty in the inferred parameters

in terms of physical process and plasma conditions not included in OML theory. The spherical Langmuir probes are part of the Swarm Electric Field Instruments (EFI). By using PIC simulations with a representative sample of ionospheric plasma parameters, the collection of plasma particles by the Swarm Langmuir probes is studied to better understand the physics of this process. Swarm methodology to infer plasma parameters from probe measurements is tested under more realistic plasma conditions to qualitatively and quantitatively assess the uncertainties derived from the use of OML theory in the interpretation.

For this purpose, analytic expressions obtained in the OML approximation, and used to interpret Swarm probe measurements, are presented. A brief description of the kinetic simulation tool is then given. Simulation results are presented in two independent sections. Section 4.3 considers the ion saturation region of the probe characteristic, from which the plasma density can be determined. Collected electron currents in the retardation and electron saturation region are then discussed in Section 4.4, from which the electron temperature is inferred.

4.2 METHODOLOGY

4.2.1 ORBITAL MOTION LIMITED THEORY (OML)

OML theory offers a relatively good balance between simplicity and accuracy which makes this analytic approach a good practical option for interpreting probe measurements in terms of plasma parameters. In the ionosphere, if the radius of Langmuir probes used on Low Earth Orbit (LEO) missions is smaller than the Debye length, particle collection by the probes can be approximated in the OML approximation. With probes on LEO missions, the satellite speeds are typically much larger than ion thermal speeds, but much smaller than electron thermal speeds. As a result, in the satellite reference frame ions are seen as drifting from the ram direction at supersonic

speeds, while electron drifts are practically negligible. These conditions can readily be accounted for in the OML theory.

Knudsen et al. [65] recently derived a set of equations from OML theory for the current collected by the spherical probe that is used in Swarm to infer electron densities and temperatures. These equations, however, are derived by assuming the limiting case where the plasma flow is much larger than the ion thermal speed, and hence, the contribution to the collected current from ion thermal motion is neglected. In appendix A, an expression for the collected current by a spherical probe immersed in a drifting plasma is derived on the basis of OML theory. This derivation accounts for the contribution to the collection of particles due to plasma flow, and particle thermal motion, as a function of the probe voltage. Assuming a single species for simplicity, the current collected by a probe with negative voltage is given by

$$\begin{aligned}
 I_{net} &= \pi a^2 q n \left(\frac{2kT_i}{\pi m_i} \right)^{1/2} \left[e^{-x_{id}} + \left(1 + 2x_{id} - \frac{2qV}{kT_i} \right) \frac{\sqrt{\pi} \operatorname{erf}(x_{id})}{2 x_{id}} \right] \\
 &- \pi a^2 q n \left(\frac{2kT_e}{\pi m_e} \right)^{1/2} \left\{ \frac{x_{ed} + x_{em}}{2x_{ed}} e^{-(x_{ed}-x_{em})^2} + \frac{x_{ed} - x_{em}}{2x_{ed}} e^{-(x_{ed}+x_{em})^2} \right. \\
 &+ \left. \left[\frac{1}{2} + x_{ed}^2 - \frac{qV}{kT_e} \right] \frac{\sqrt{\pi} \operatorname{erf}(x_{ed} - x_{em}) + \operatorname{erf}(x_{ed} + x_{em})}{2 x_{ed}} \right\}, \quad (4.1)
 \end{aligned}$$

while, if the potential is positive, $V > 0$, then

$$\begin{aligned}
 I_{net} &= \pi a^2 q n \left(\frac{2kT_i}{\pi m_i} \right)^{1/2} \left\{ \frac{x_{id} + x_{im}}{2x_{id}} e^{-(x_{id}-x_{im})^2} + \frac{x_{id} - x_{im}}{2x_{id}} e^{-(x_{id}+x_{im})^2} \right. \\
 &+ \left. \left[\frac{1}{2} + x_{id}^2 - \frac{qV}{kT_i} \right] \frac{\sqrt{\pi} \operatorname{erf}(x_{id} - x_{im}) + \operatorname{erf}(x_{id} + x_{im})}{2 x_{id}} \right\} \\
 &- \pi a^2 q n \left(\frac{2kT_e}{\pi m_e} \right)^{1/2} \left[e^{-x_{ed}} + \left(1 + 2x_{ed} - \frac{2qV}{kT_e} \right) \frac{\sqrt{\pi} \operatorname{erf}(x_{ed})}{2 x_{ed}} \right], \quad (4.2)
 \end{aligned}$$

Whipple [64], where

$$x_d = \frac{v_d}{\sqrt{2kT/m}}, \quad (4.3)$$

$$x_m = \sqrt{\frac{qV}{kT}}, \quad (4.4)$$

and the error function is defined as

$$\text{erf}(s) = \frac{2}{\sqrt{\pi}} \int_0^s dt e^{-t^2}. \quad (4.5)$$

For multiple ion species, equations 4.1 and 4.2 can be extended straightforwardly by replacing the expression for ions with the summation over ions species. An expression to calculate the plasma density can be obtained from the derivative Eq. 4.1 with respect to the bias voltage V . The resulting expression for the density then depends on the admittance in the ion saturation region, $d_{ion} = dI_{ion}/dV$,

$$n = \frac{dI}{dV} \left(-\pi a^2 \frac{2q^2}{v_d} \sum_{j=1}^N \frac{n_j}{n_{tot}} \frac{1}{m_j} \text{erf} \left(\frac{v_d}{\sqrt{2kT_i/m_j}} \right) \right)^{-1}, \quad (4.6)$$

The admittance is defined as the real part of the derivative of the current with respect to the probe voltage V . In Eq. 4.6, for multiple singly ionized ion species, n_j is the density of species j and n_{tot} is the total ion density. In Eq. 4.6 the contribution from electrons to the total collected current in the ion saturation region has been neglected since it is much smaller than that of ions.

In the limiting case where the plasma flow velocity is much larger than ion thermal velocity $v_d \gg v_{th}$, the asymptotic behavior of Eq. 4.1 gives a simplified expression

for the collected current in the ion saturation region

$$I_{ion} = \pi a^2 q n v_d \left(1 - \frac{2qV}{m_{eff} v_d^2} \right), \quad (4.7)$$

from which the admittance is readily seen to be

$$d_{ion} = \pi a^2 n \frac{2q^2}{m_{eff} v_d}. \quad (4.8)$$

From Eq. 4.8, it follows that the density is given by

$$n = d_{ion} \left(\pi a^2 \frac{2q^2}{m_{eff} v_d} \right)^{-1}, \quad (4.9)$$

When the probe voltage is positive, the probe then collects electrons. In the ionosphere, the electron speed is typically more than one order of magnitude larger than the plasma speed in the satellite reference frame. As a result, the current collected from electrons can be approximated by

$$I_{ret} = \pi a^2 q n v_d \left(1 - \frac{2qV}{m_{eff} v_d^2} \right) - 4\pi a^2 q n \sqrt{\frac{kT_e}{2\pi m_e}} \exp\left(\frac{qV}{kT_e}\right) \quad (4.10)$$

in the retardation region, where the admittance $d_{ret} = dI_{ret}/dV$ is given by

$$d_{ret} = \pi a^2 n \frac{2q^2}{m_{eff} v_d} - 4\pi a^2 q^2 n \sqrt{\frac{1}{2\pi m_e}} \frac{1}{\sqrt{kT_e}} \exp\left(\frac{qV}{kT_e}\right), \quad (4.11)$$

whereas the current in the electron linear region is

$$I_{lin} = 4\pi a^2 q n \sqrt{\frac{kT_e}{2\pi m_e}} \left(1 + \frac{qV}{kT_e} \right), \quad (4.12)$$

and the admittance $d_{lin} = dI_{lin}/dV$ is

$$d_{lin} = 4\pi a^2 q^2 n \sqrt{\frac{1}{2\pi m_e}} \frac{1}{\sqrt{kT_e}}. \quad (4.13)$$

An expression to infer the electron temperature can be derived by combining equations 4.10, 4.7, 4.11, and 4.8, as follows

$$\begin{aligned} I_{ret} - I_{ion} &= \pi a^2 n \frac{2q^2}{m_{eff} v_d} (V_{ret} - V_{ion}) - 4\pi a^2 q^2 n \sqrt{\frac{kT_e}{2\pi m_e}} \exp\left(\frac{qV}{kT_e}\right) \\ &= d_{ion} (V_{ret} - V_{ion}) - 4\pi a^2 q^2 n \sqrt{\frac{kT_e}{2\pi m_e}} \exp\left(\frac{qV}{kT_e}\right) \end{aligned} \quad (4.14)$$

$$\begin{aligned} \frac{kT_e}{q} \times (d_{ret} - d_{ion}) &= kT_e \times \left(-4\pi a^2 q n \sqrt{\frac{1}{2\pi m_e}} \frac{1}{\sqrt{kT_e}} \exp\left(\frac{qV}{kT_e}\right) \right) \\ &= -4\pi a^2 q n \sqrt{\frac{kT_e}{2\pi m_e}} \exp\left(\frac{qV}{kT_e}\right) \end{aligned} \quad (4.15)$$

$$I_{ret} - I_{ion} = d_{ion} (V_{ret} - V_{ion}) + \frac{kT_e}{q} \times (d_{ret} - d_{ion}) \quad (4.16)$$

Finally, Eq. 4.16 can be solved for the electron temperature T_e (in eV)

$$T_e = \frac{I_{ret} - I_{ion} - d_{ion} (V_{ret} - V_{ion})}{d_{ret} - d_{ion}}, \quad (4.17)$$

which gives a convenient analytic expression for the electron temperature from probe measurements in the ion saturation and electron retardation regions, Knudsen, et al. [65]. Note that Eqs. 4.10 and 4.11 are approximations resulting from neglecting the plasma flow contribution to the net current since electron thermal speeds are much larger than electron drift speeds in satellite' rest frame. In Eqs. 4.12 and 4.13, the ion contribution to the net current has been neglected since it is approximately four orders of magnitude smaller than that of electron.

4.2.2 SWARM PROBE MEASUREMENTS INTERPRETATION

In Swarm, measurements of voltage, current and admittance, are used to infer the plasma density and electron temperature, using analytic expression obtained in the OML approximation. These measurements are made in the ion saturation, electron retardation, and electron saturation regions. The plasma density is obtained from measurements in the ion saturation region as prescribed in Eq. 4.9. In current applications of this equation, plasma is assumed to consist of electrons and 100% singly ionized oxygen ions. As a result, the effective atomic mass appearing in Eq. 4.9 is assumed to be exactly 16, then Eq. 4.7 becomes

$$I_{ion} = \pi a^2 q n v_d \left(1 - \frac{2qV}{16m_p v_d^2} \right), \quad (4.18)$$

and similarly Eq. 4.9

$$n = d_{ion} \left(\pi a^2 \frac{2q^2}{16m_p v_d} \right)^{-1}. \quad (4.19)$$

Using kinetic simulations to compute collected currents under different space environment conditions, the applicability of this expression for the density can be assessed straightforwardly. Specifically, kinetic simulations carried out for different voltages of the probes in the ion saturation region, can be used to determine the ion admittance. Comparing the predicted density on the basis of Eq. 4.19 with the known ones used in the simulations then provides a measure of the errors in the analytic model predictions.

Similarly, electron temperatures predicted with Eq. 4.17 can be compared with known ones used as input in the kinetic simulations, thus providing error estimates in these predictions. As for density, this is done by carrying out simulations in the retardation, electron and ion saturation regions to determine the parameters appearing in Eq.

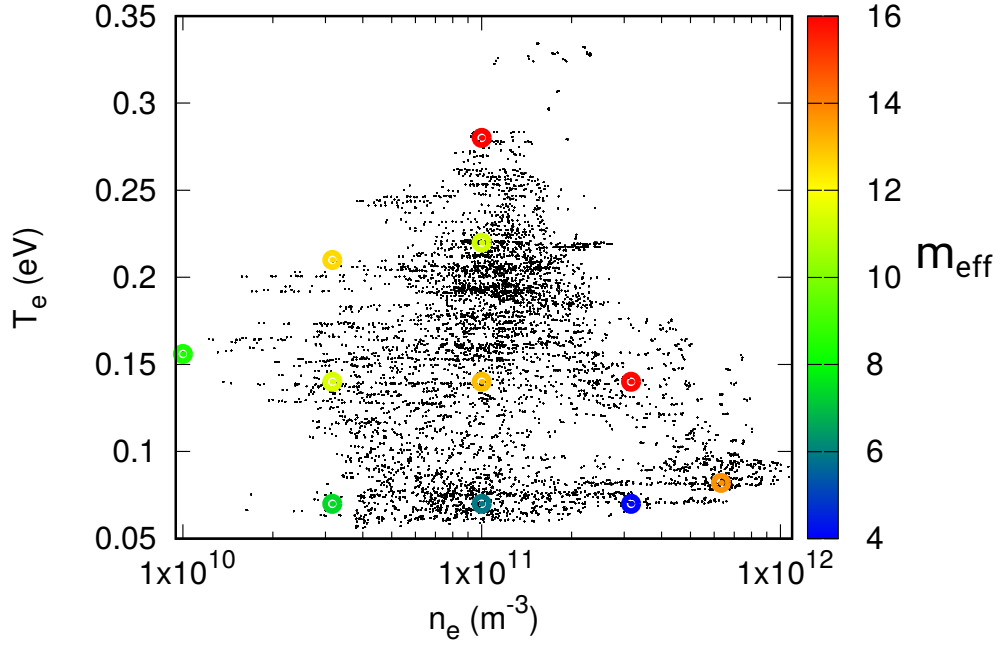


Figure 4.1: Plasma parameters considered in PIC simulations obtained from the IRI model. The plot shows values for electron temperature and plasma density (on a logarithmic scale) obtained from the IRI model. The data points in colored circles are the plasma parameter used in the kinetic simulations. The color bar represents the values of ion effective mass.

4.17. The discrepancy between predicted temperatures and the known ones used as input in the simulations then provides an estimate of the uncertainties in the model predictions.

4.2.3 SIMULATIONS SETUP

Simulation results are obtained for several configurations of plasma parameters, including, density, temperature, ion plasma composition, background magnetic field, and two different geometric configurations for the spherical Langmuir probes.

The sample of plasma parameters considered in the simulations has been obtained with the International Reference Ionosphere (IRI) model [110] for different latitude, longitudes, daytimes, and for a range of altitudes between 450 – 500 km. Considering

the fact that the IRI is constructed using a combination of historical data and results from ionospheric models, and that it does not account for the significant variability which characterized the ionosphere, it cannot be used to determine the state of the ionosphere at given times and positions. As a consequence, it cannot be seen as a substitute for in situ measurements. Figure 4.1 shows a scatter plot for plasma density and temperatures obtained from the IRI model. The colored circles represent the cases considered in the kinetic simulations, in which the color scale is used to provide the value of the ion effective mass, with values lower than 16 indicating the presence of minority ions in the plasma. A background magnetic field of $\vec{B} = (36.6, 0, \pm 8.56) \mu\text{T}$ was considered in some cases to investigate the effect of the electron thermal gyration radius in the current collection. Considering that Swarm satellites have an orbital speed of approximately 7673 m/s in the quasi-inertial geocentric reference frame, this speed has been assumed for the plasma ram flow in many simulations. Several simulations have been made to account for possible ionospheric winds with speed of up to ± 500 m/s in the ram direction. Winds perpendicular to the ram velocity of the same magnitude have not been considered in the simulations since it was found that their effect on the particle collection is negligible, below 1%.

Two geometrical configurations for a spherical probe have been considered. The first one consists of an isolated sphere of 4 mm radius in an otherwise uniform plasma background. In this case, no account is taken for the presence of the main body of the satellite or the post holding the sphere. This is the simplest case considered, and it is the one for which the OML approximation is best satisfied. The second case accounts for the presence of the main body of the spacecraft and the 9.53 cm post joining it to the satellite bus. The posts holding the spheres are grounded to the spacecraft. In this geometry, illustrated in Fig. 4.2, only a simplified and truncated geometry of the Swarm ram end is considered because accounting for the full length of the satellite

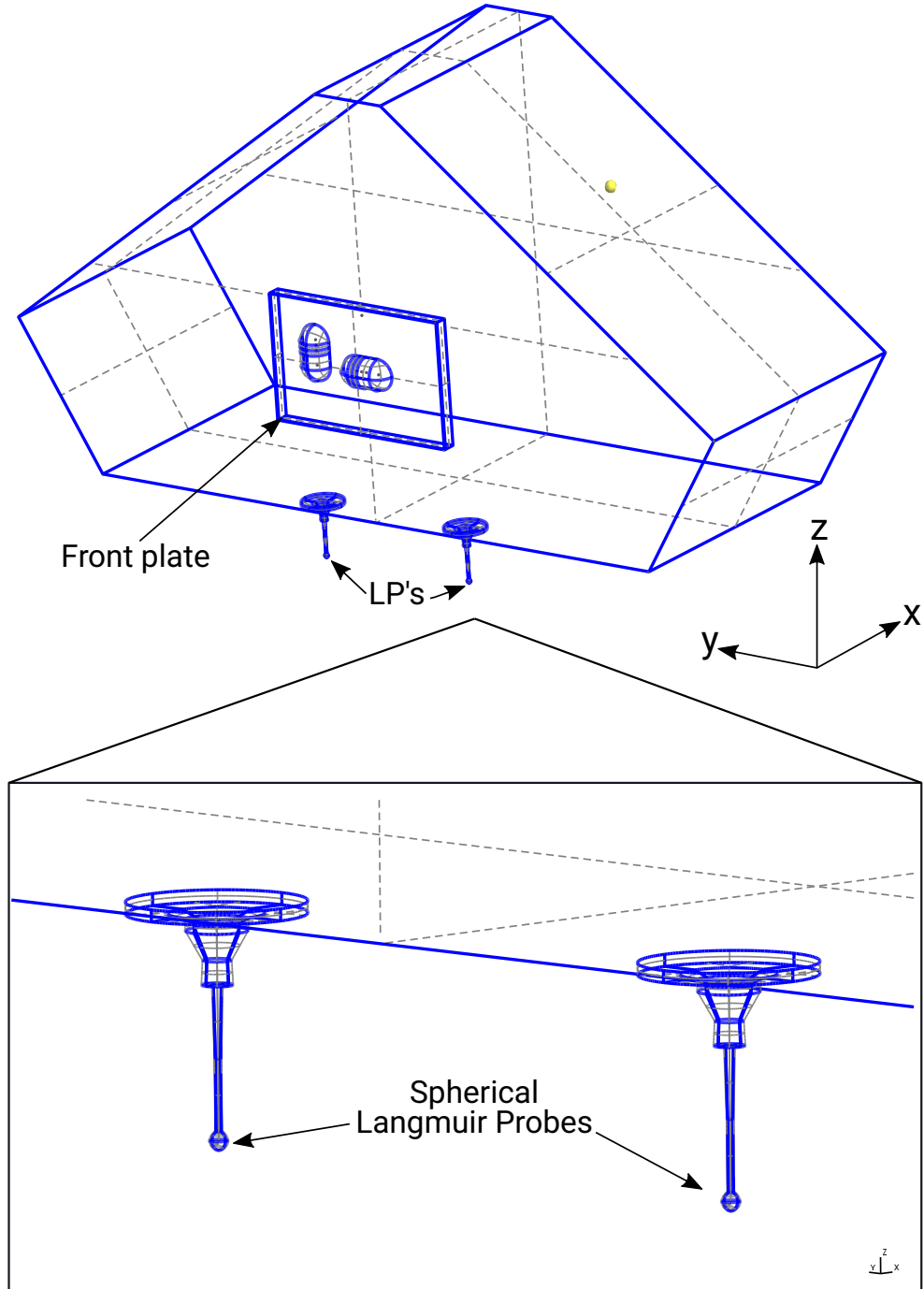


Figure 4.2: Geometry used in kinetic simulations. The spherical Langmuir probes are mounted on a post attached to the bus of the satellite. The satellite is a truncated version of the full Swarm geometry [112]. The radius of the spherical probes is 4 mm where the distance from the center of the sphere to the bus of the satellite is 99.01 mm. The shells and front plate are also included.

would have been computationally too time consuming. Mostly, accounting for the full length of the satellite should have negligible impact on probe current characteristic, given their location near the satellite ram face. With the second configuration, the validity of the OML interpretation of the characteristic is tested under more realistic conditions, especially to assess the effect of nearby charged objects in the collection of particles by the spherical probe. In this case, two spherical probes of 4 mm radius are attached to the satellite bottom as in an actual Swarm satellite. Accounting for the two probes has the advantage of providing independent characteristics and reduce statistical errors by averaging calculated collected currents. It also provides an estimate of finite discretization errors made in the simulations.

Kinetic simulations were made with PTetra, an electrostatic three-dimensional particle in cell (PIC) code. In this model, space is discretized with an adaptive unstructured tetrahedral mesh, and many physical processes of relevance to spacecraft environment interaction can be considered [71]. Simulations were made using meshes with 1.5 to 4.6 million tetrahedrons, with numbers of simulation particles ranging from approximately 38 to 549 million per species. This corresponds to statistical weights ranging from 15 to 1324 for the isolated probe simulations, and from 236 to 8532 for simulations including the truncated satellite bus. In the model, both electron and ions are treated fully kinetically, and electric fields are calculated self-consistently by solving Poisson's equation at each time step. When simulating the isolated probe characteristic, in case 1, the simulation domain consists of a cylinder of radius of 20 cm and length 60 cm. In case 2 where a more realistic geometry is considered, the simulation domain is also cylindrical with a radius of 1 m, and a length of 7 m.

4.2.4 RIPPLE TECHNIQUE

Since the plasma parameters are inferred from in situ measurements, voltages, currents, and admittance, it is important to explain how these measurements are obtained. There are two methods for measuring the net currents collected by a Langmuir probe which are the most commonly used. In a full sweep, the probe bias voltage is varied from a sufficient negative bias potential, in the ion saturation region, up to a sufficient positive potential in the electron linear region. In a full sweep, the full characteristic of the probe is obtained, including the three regions of most interest, namely the ion saturation, the retardation and the electron linear region. An alternative approach used on Swarm, is referred to as “*the ripple*”. Instead of collecting current with a full sweep, thus generating a full characteristic, this method focuses on the parts of the characteristics needed to infer the density and temperature. With the ripple, probe voltages are modulated sinusoidally at a certain frequency, and with a variable amplitude depending on the region of the characteristic.

In Swarm, the ripple technique is used to measure currents and admittances. The three key region of the characteristic are measured with this technique as illustrated in Fig. 4.3, and the results are averaged over 10 full cycles. Ripple measurements are taken every 128 s, with a duration of 1 s, Knudsen, et al. [65]. The frequency for the sinusoidal signal for the voltage can be set from 128 Hz up to 4 kHz. The frequency used on-board Swarm is 128 Hz for all three regions. The amplitude of the ripple, however, is different for each region. In the ion saturation region, an amplitude of 625 mV is used, whereas for the retardation region 78 mV is used instead. For the electron linear region, two values for the amplitude are used: 156.25 and 312.5 mV for high and low gain probe operation respectively. The probe is operated at high/low gain depending on the plasma density. In high gain, the current is amplified by a

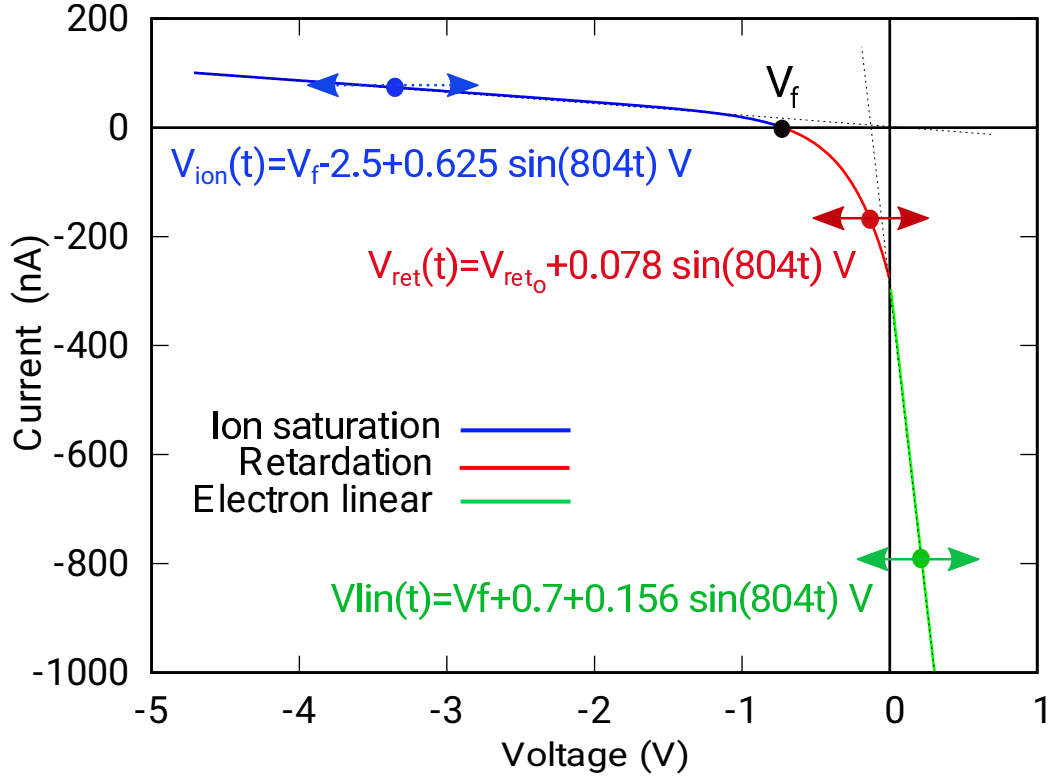


Figure 4.3: Ripple technique used in Swarm. The sinusoidal signal for the bias voltage is varied at frequency of 128 Hz. The amplitude of the sinusoidal signal depends on the characteristic region of interest.

factor of 50 compared to that in low gain, thus providing more sensitivity in low plasma density conditions.

Kinetic simulations implementing the ripple technique have been made for the purpose of comparing steady state solutions with those obtained from the ripple method. For these simulations, only the first geometrical configuration for the probe has been considered, that is, only the sphere is present in the simulation domain. Owing to the large number of particles and size of the simulation mesh required, simulating a probe at steady state can take days of computer time. Simulating the time evolution of a collected current in a ripple is much more time consuming and can take up to several

weeks. With a steady state solution only a single voltage and its respective current is obtained, whereas using the ripple, a continuous profile of voltage-current becomes available. Since the OML theory predicts a linear dependence of the current with applied voltage in the ion saturation and electron linear region, it should be sufficient in principle to have a pair of current-voltages in each region, in order to calculate the admittance. In the retardation region, if a variation in the applied voltage is small enough, the current response can be approximately linear. In that case, two or three points on the I-V characteristic in this region should be sufficient to calculate the admittance. Comparing steady state solutions to those from the ripple approach, it was possible to conclude that admittances obtained from steady state solutions were sufficiently accurate.

With the ripple technique, because the bias voltage of the probe is changing in time, particles could respond to this perturbation generating plasma waves and cause a phase lag between voltage and collected current. In the simulations, the voltage has been varied at a frequency of 4 kHz since, if no waves and associated phase lag occur at this higher frequency, it is unlikely that they would be manifest at lower frequencies. In that case, currents vs. voltages measured with the ripple technique should be the same as those obtained at steady state, which would require much less simulation time. In order to estimate possible phase shifts between harmonic voltage applied to the probe, and collected current, a density of 10^{10} m^{-3} , electron temperature $T_e = 0.236 \text{ eV}$ and ion temperature $T_i = 0.125 \text{ eV}$ were considered. An ion effective mass $m_{eff} = 13.3 \text{ amu}$ was used in order to account for light ion species in addition to oxygen ions.

For the ion saturation region, the ripple technique was applied with variations in the voltage in the range $-2.5 \text{ V} \pm 625 \text{ mV}$ with respect to the background plasma. Note that on Swarm, the same range of voltages are used, but those are with respect to

the spacecraft. The voltages considered in the simulations can therefore be different from the ones in situ, depending on the spacecraft floating potential. Similarly, the electron linear region was simulated when the probe voltage was varied in the range $0.7V \pm 156$ mV with respect to background plasma. In the simulations, voltages with respect to background plasma were used instead, to make sure that the simulations would be made in the saturation regions. The electron retardation region was found at $V_{ret} = -0.355$ V by using the interpolation between ion saturation region and electron linear region, while the ripple amplitude used in simulations was 0.078 V. Simulation results show a small phase shift between the applied voltage and the collected current. The phase shifts between voltage and current are found to be 2.44×10^{-3} rad, 7.79×10^{-2} rad, and 1.47×10^{-2} rad, in the ion saturation, electron retardation and linear region, respectively. The current collected by the probe as a response to the applied voltage is shown in top Fig. 4.4 and 4.5, for the ion saturation and retardation region, respectively. Note that the aspect ratio in the figures is not 1 : 1 in order for small phase shift to be visible. At the bottom of both figures, 4.4 and 4.5, the current and voltage are plotted as a function of time with a phase shift of π rad. Because the phase shift in the electron retardation region is one order of magnitude larger than in the ion saturation, the difference in phase between current and voltage is more visible in Fig. 4.5. The blue dots in Fig. 4.4, are simulation results calculated from a steady state solutions. The green dots in both figures, are currents calculated using the OML equations 4.1 and 4.2. The plasma conditions considered in the simulations give an electron plasma frequency of $\omega_{pe} = 897$ kHz. This frequency is much higher than the 4 kHz used when simulating the ripple, which is consistent with the small phase shifts calculated. The phase shift would be even smaller with the 128 kHz ripple used on Swarm. Note also that due to the supersonic flow, any standing ion acoustic wave between the probes and the spacecraft would be

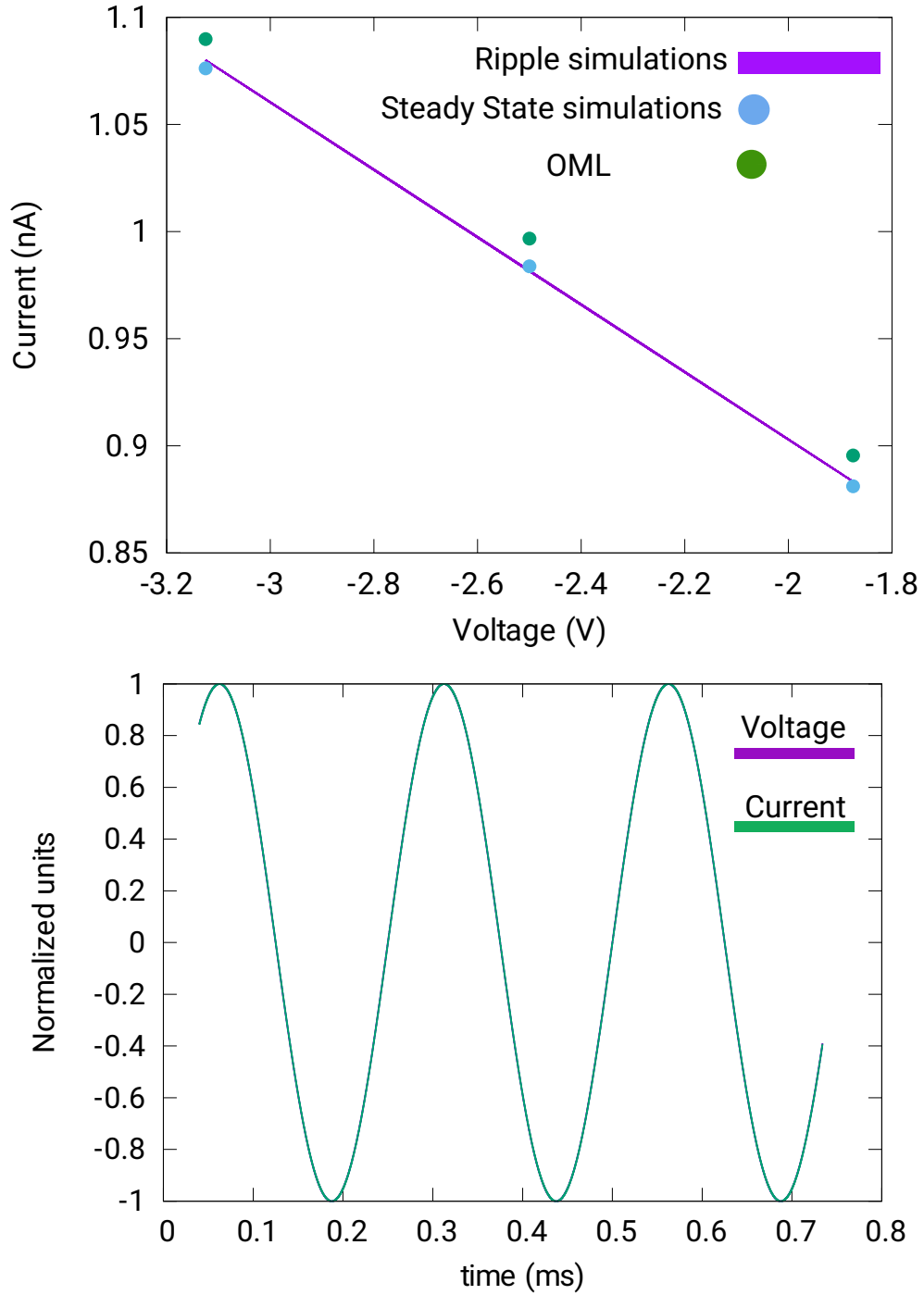


Figure 4.4: The top panel shows the current response to the applied time varying voltage of the spherical Langmuir probe, operated in the ion saturation region. The bottom panel shows the normalized voltage and collected current as a function of time. The phase difference between the two is approximately 2.44×10^{-3} rad, with the current lagging the voltage. The phase shift here is too small to be visible in the plot.

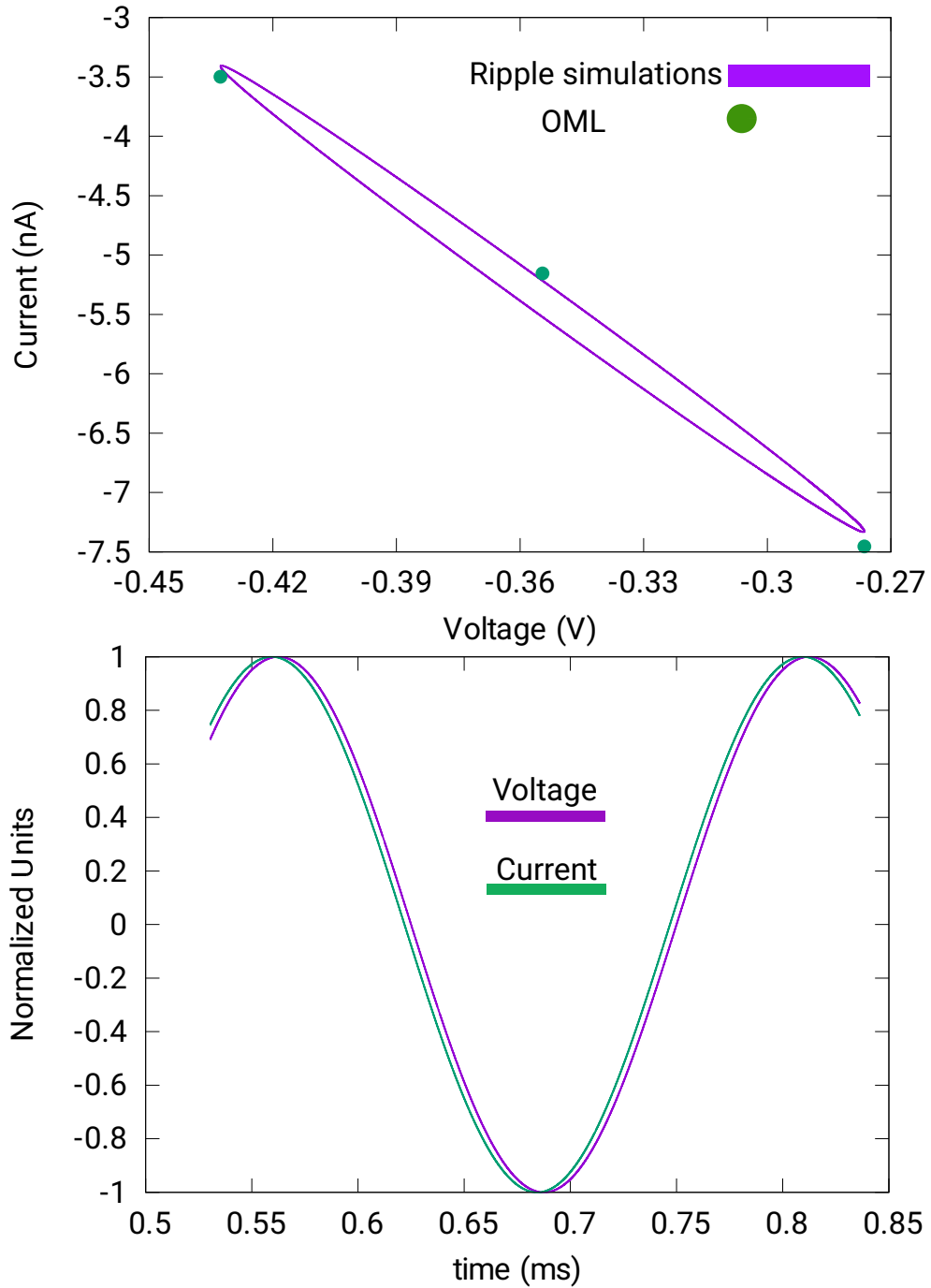


Figure 4.5: The top panel shows the current response to the applied time varying voltage of the spherical Langmuir probe, operated in the retardation region. The bottom panel shows the normalized voltage and collected current as a function of time. The phase difference between the two is approximately 7.79×10^{-2} rad, with the current lagging the voltage.

“swept” downstream.

The steady state results and those obtained from OML theory are in good agreement with those calculated with the ripple technique. Voltages, currents and admittances, calculated from simulations using the ripple technique were used as input in Eqs. 4.6 and 4.17, to infer plasma parameters. In this case, a relative error in the density of $\epsilon_n = 4\%$, and electron temperature $\epsilon_{T_e} = 3\%$, with respect to simulation input parameters were found. Overall, these results, involving the ripple technique, steady state solutions, and OML theory, are in good agreement and seem to be equivalent for the plasma parameters considered here. It can be concluded that currents calculated from simulations using the ripple technique are equivalent to those of simulations made for steady state. Currents predicted with the analytic solutions Eq. 4.1 and 4.2 are also found to be in good agreement with both simulation results.

Recalling the fact that simulations using the ripple technique are considerably more computationally intensive than those for steady state solutions, in the following, only results from simulations made for steady state current response are considered. A minor disadvantage in considering steady state solutions instead of time dependent solutions is the loss of details in the probe characteristic obtained using the ripple. However, steady state solutions prove to be sufficient for the purpose of this work, where one of the goals is to understand qualitatively how the space plasma environment affects the in situ measurements of the probe on-board Swarm.

4.3 ION SATURATION REGION. PLASMA DENSITY

Probe collected currents have been simulated in the three key regions of the $I - V$ characteristic. In each case, two or three currents were obtained from steady state solutions in order to calculate the admittance. Currents calculated from simulations while accounting for different combinations of plasma parameters, magnetic field and

geometry, are compared to those predicted by the OML theory. The plasma density and temperature inferred from simulated probe measurements are then compared to the input parameters of the simulations.

The first results presented are those obtained when the isolated spherical probe is simulated in the ion saturation region, from which, the plasma density can be inferred using Eq. 4.1, 4.6, 4.19. In these results, the magnetic field was not accounted for. Selected cases have been simulated with the inclusion of a background magnetic field in the ion saturation region. Because for the ionospheric conditions considered, the thermal gyroradius of ions is relatively large (1–4 m) compared to the probe radius, the incoming ions can reach the probe as if the particles were not magnetized. This explains why the current collected were practically the same with the inclusion or absence of magnetic field.

4.3.1 ION CURRENTS. ISOLATED PROBE

Table B.1 lists currents calculated for an isolated spherical probe in the ion saturation region, in the absence of any other structure. In Table B.1, I_{sim} is the current from kinetic simulations, while, $\epsilon_{I_{OML}}$ and $\epsilon_{I_{OML_{16}}}$ are the relative differences between I_{sim} and those currents predicted with 4.1 (I_{OML}) and 4.18 ($I_{OML_{16}}$) respectively. ϵ_{OML} and $\epsilon_{OML_{16}}$ are defined as follow

$$\epsilon_{I_{OML}} = (I_{sim} - I_{OML})/I_{sim} \quad (4.20)$$

$$\epsilon_{I_{OML_{16}}} = (I_{sim} - I_{OML_{16}})/I_{sim}. \quad (4.21)$$

In all cases the drifting plasma flow is taken to be equal to the Swarm ram speed $v_d = 7673$ m/s. The probe is biased to three different voltages V_p . In bold, the 4.2% maximum relative difference in ϵ_{OML} suggests that the analytic expression for the collected current by a spherical Langmuir probe immersed in a drifting plasma,

Eq. 4.1, captures the physics involved in the ion collection. On the other hand, when the plasma is assumed to be composed by 100% O^+ , currents from simulations are overestimated up to 61.1 % (column ϵ_{OML16}) with respect to those predicted by the analytic model used in Swarm Eq. 4.18. In table B.1, $\delta_{I_{sim}}$ are the relative uncertainties on the currents obtained from simulations.

The uncertainties in the simulated collected currents are calculated from

$$\delta_{I_{sim}} = \frac{\sigma}{\sqrt{\mathcal{N}}}, \quad (4.22)$$

where σ is the standard deviation in the calculated current and $\mathcal{N} = t_{tot}/\tau$, where t_{tot} is the total time of the simulation at steady state considered in the calculation of σ , and τ is the decorrelation time between measurements in the simulation which in this case, is taken to be ten time steps, $\tau = 10 dt$. Figure 4.6 shows an example of currents collected by the two spherical probes, plotted as a function of time, where the red bar represents the estimated decorrelation time τ . The noise level in the signal of the simulated probe currents depends on the probe collection area, which is relatively small in Swarm's probes (probe radius 4 mm), the plasma density, and on the number of macroparticles used in the PIC simulations.

An example of cross-section for the charge density and electric equipotentials calculated from kinetic simulations is shown in Fig. 4.7. In this example, the probe voltage is -4.5 V, the density is $n = 1 \times 10^{10} \text{ m}^{-3}$ and the electron temperature is $T_e = 0.156$ eV. The charge density in Fig. 4.7 shows the wake formed due to the supersonic plasma at which the accumulation of ions distorts the electric potential.

The electric potential illustrated in Fig. 4.7 is used to calculate particle trajectories shown in Fig. 4.8. Twelve particles, six H^+ and six O^+ , were injected from the ram boundary. Three different particle velocities were used, v_{ram} and $v_{ram} \pm v_{th}$, where

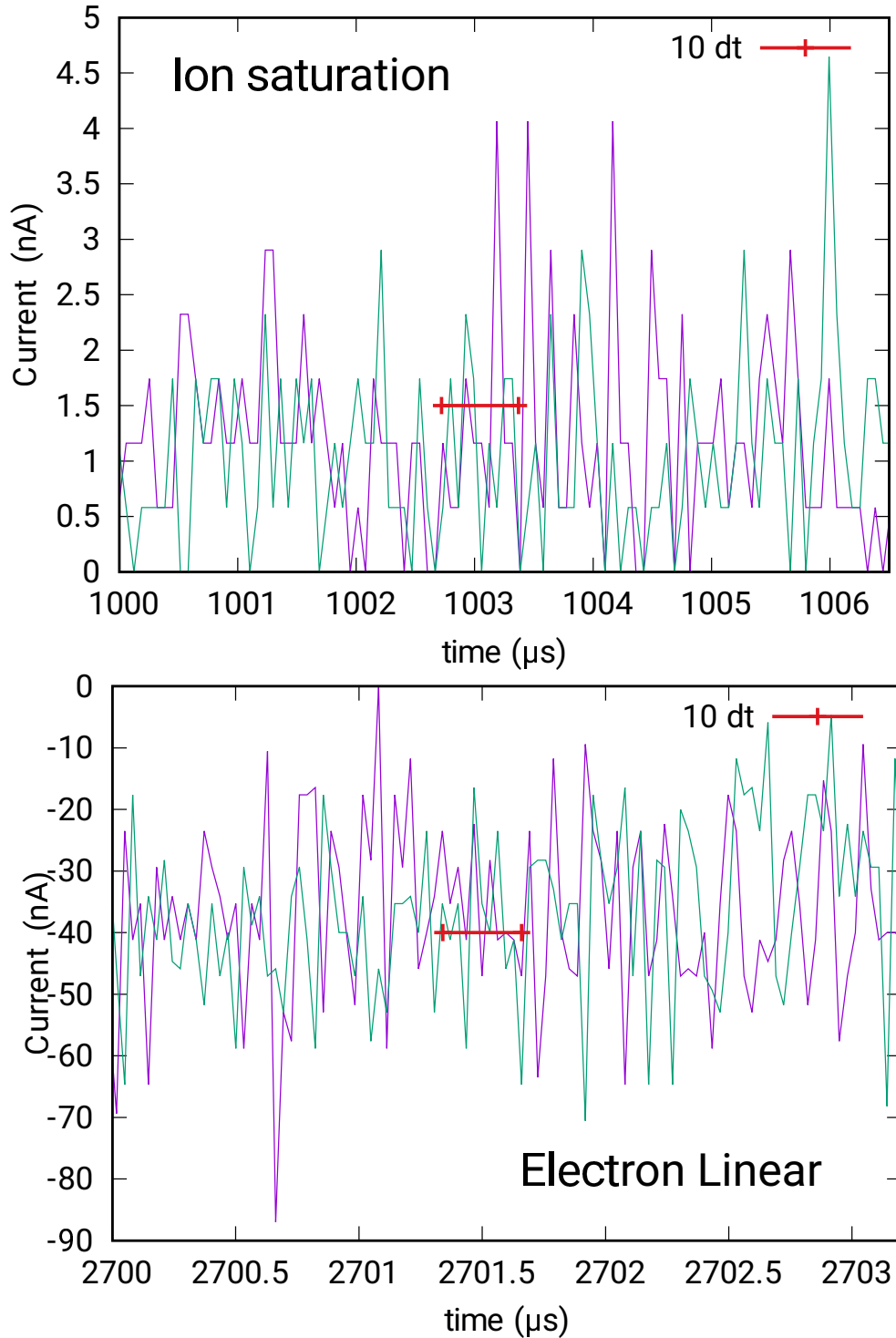


Figure 4.6: Sample currents collected by the two Swarm spherical probes as a function of time. The uncertainty in the simulation results is calculated with a decorrelation time in the measurements τ equal to ten time steps ($10dt$, red bar) estimated by inspection.

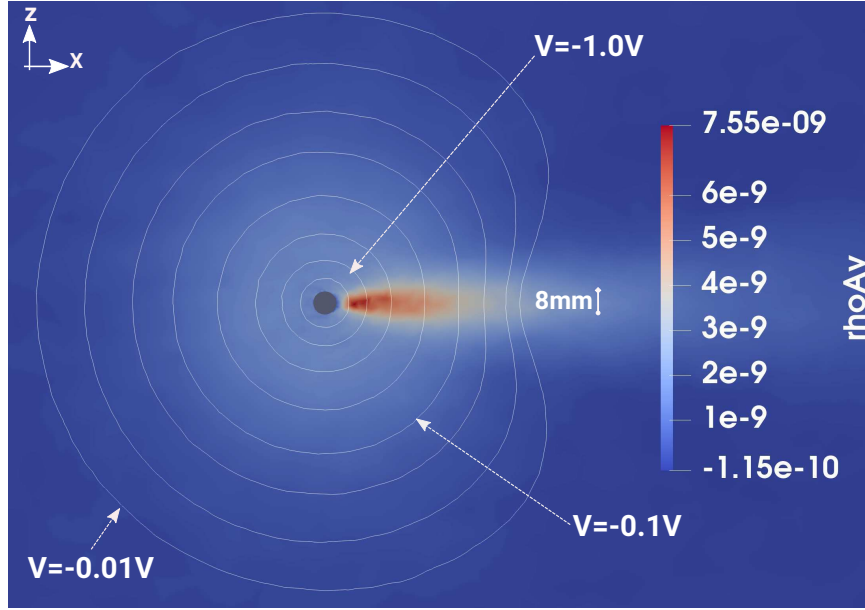


Figure 4.7: Cross-section of the charge density, with electric equipotentials when the spherical Langmuir probe is operated in the ion saturation region. The probe voltage is -4.5 V. In this case, the plasma density is $n = 1 \times 10^{10} \text{ m}^{-3}$, the electron temperature is $T_e = 0.156$ eV, whereas the plasma flow velocity is $v_d = 7673$ m/s.

$v_{th} = \sqrt{2kT_i/m_i}$ is the thermal speed of ion species i . In the absence of an electric field, particles would travel ballistically in the x direction. However, as seen in Fig. 4.8, the probe electric field sheath deflects some of the incoming ions towards it, where only those with the highest energy overcome the attracting force and are not collected. Fig. 4.8 shows the particle trajectories predicted by OML theory, in which depending on the energy of the ions traveling towards the probe, particles would be collected or not. The next step in the analysis is to calculate the plasma density using the calculated currents. Voltages and currents from Table B.1 are used in Eqs. 4.1 (solved for n), to calculate the admittance (d_{ion}) that are then used in Eqs. 4.6, and 4.19. The relative errors between inferred densities obtained from the three methods and the density used as input parameters in the kinetic simulations are given in Table

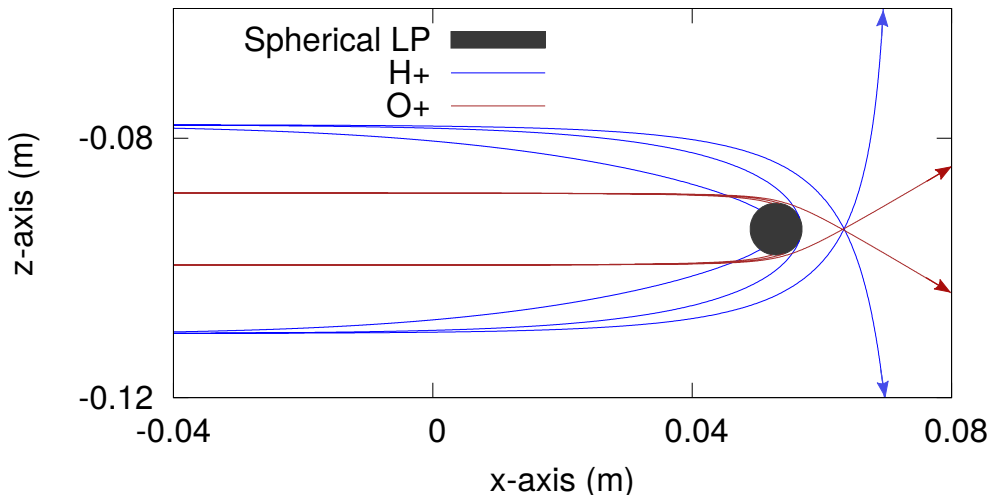


Figure 4.8: O^+ and H^+ ion trajectories deflected due to the probe sheath electric field when the spherical probe is operated in the ion saturation region. Both species are aimed slightly below or above the spherical probe with velocities exactly from the ram direction. Ideally, the incoming ions would be collected by the probe. Three speeds are considered corresponding to v_{ram} , and $v_{ram} \pm v_{th}$ with $v_{th} = \sqrt{2kT/m}$ being the species thermal speed. Particles with the lower speed ($v_{ram} - v_{th}$) are deflected the most, and the ones with the higher speed ($v_{ram} + v_{th}$) are deflected the least.

B.2. ϵ_{n_I} , ϵ_n , and $\epsilon_{n_{16}}$ are the relative error corresponding to the densities calculated from 4.1 (solved for n), 4.6, and 4.19, respectively.

$$\epsilon_{n_x} = \frac{n_{inferred} - n_{input}}{n_{inferred}} \quad (4.23)$$

$$\delta_{n_x} = \frac{\Delta n_{inferred}}{n_{inferred}} \quad (4.24)$$

In Table B.2 the maximum relative errors are in bold, while the uncertainties in the inferred densities are given under δ_{n_I} and δ_n . It is clear that from the three methods presented here, the most accurate densities (within 4%) result from solving Eq. 4.1 for n , followed by using calculated admittance in Eq. 4.6 with an accuracy within 10%. Errors in the currents are amplified in the calculation of the admittance because

a numerical derivative tend to increase errors, thus yielding enhanced errors in the inferred plasma density. The largest discrepancies come from using d_{ion} in Eq. 4.19, with overestimations up to 75%, when the plasma ion composition is assumed to consist of 100% O^+ .

In Fig. 4.9 the contents in Tables B.1 and B.2 are plotted at the top and bottom respectively. This serves to demonstrate the contribution of minority ions to the net current, and their impact on the calculated plasma density. The relative errors in current and density are plotted on the y axis while on the x axis a factor involving a ratio between the Debye length λ_D and the probe radius r_p , and the probe floating potential V_f to the probe voltage V_p . The reason for considering relative errors as a function of $(\lambda_D/r_p)(V_f/V_p)$ comes from observing the data in both Tables B.1 and B.2, showing that the relative errors increase as the Debye length increases, and decrease as the voltage increases. In these first simulations, the probe floating potential V_f is the one computed for each case of plasma parameters, however, in the next subsection when the bus of the satellite is present in the simulation domain, variations on the satellite floating potential V_f additional to the one computed, play an important role in ion collection. The color bar on both plots refers to the effective mass. In the presence of minority ions, simulated currents are larger than those predicted with Eq. 4.18, which neglects the contribution from minority ions. This in turn yields relatively large overestimations in the inferred plasma density.

Simulations made with an isolated probe in the absence of any nearby object, represent an ideal scenario for particle collection. It is then best suited not only to test the validity of OML theory under ionospheric plasma conditions, but also the additional assumptions made in interpretation of Swarm probe measurements. The results shown in Fig. 4.9 demonstrate that assuming an ion concentration of 100% O^+ for ionospheric plasma may yield discrepancies up to 61% between simulated currents

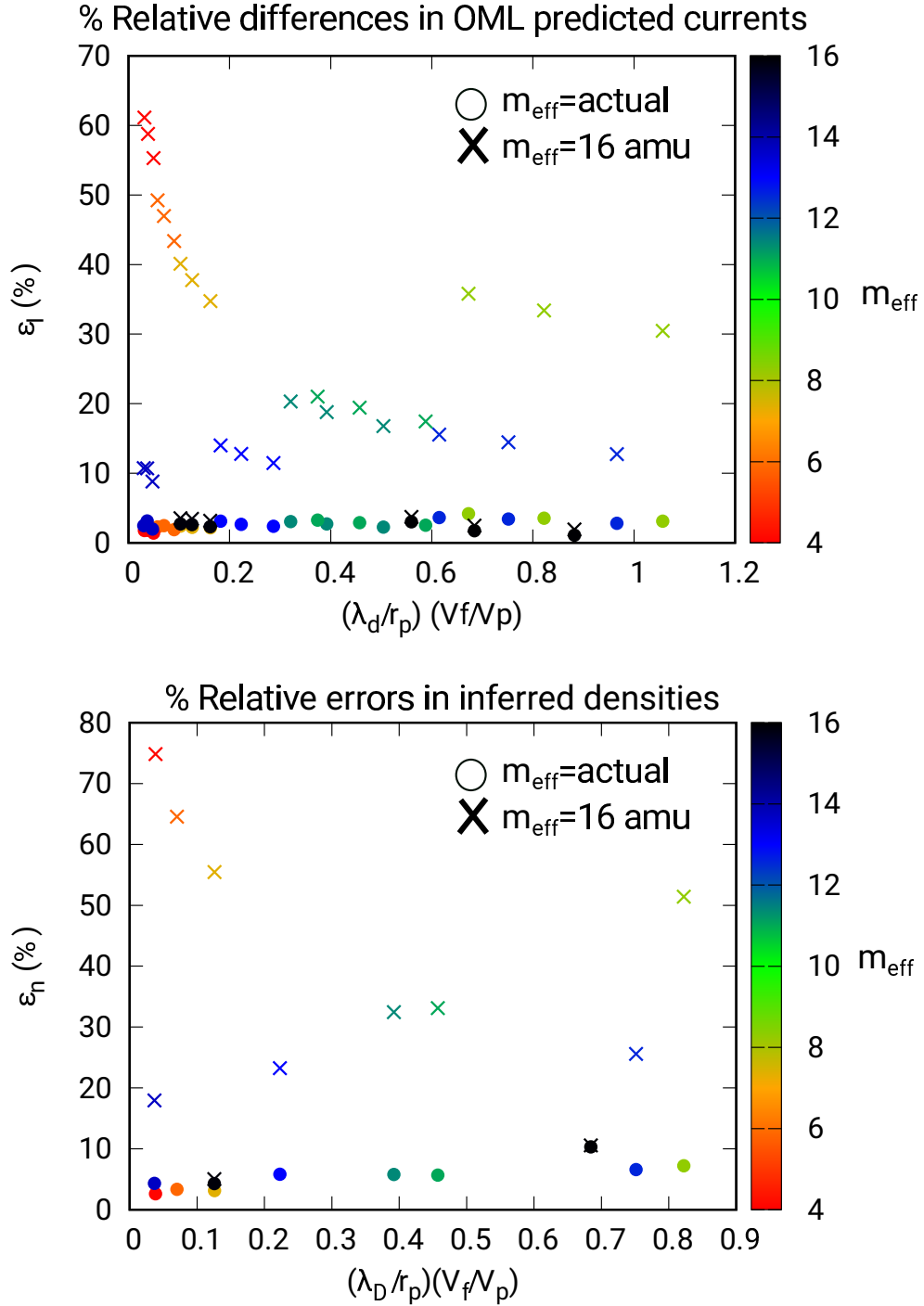


Figure 4.9: Top: Relative error in currents from simulations compared to those predicted with OML, I_{OML} from Eq. 4.1, and I_{OML16} from 4.18. Bottom: Relative error in inferred density with respect to the one used as input in the simulations. n_{OML} is obtained from Eq. 4.6, and n_{OML16} from 4.19. These results were obtained for an isolated probe in the simulation domain.

and the ones predicted by Eq. 4.18. Similarly, relative errors up to 75% between the inferred densities and the ones used as input in the simulations are found when the percentage of minority ions is not negligible, and not accounted for in the interpretation of probe measurements. Due to their relatively smaller masses, ions traveling toward the probe are more easily deflected by the probe electric field, enhancing the collected current as seen in Fig. 4.8, confirmed in the result plotted in Fig. 4.9. If the contribution from minority ions is considered as in the analytic model using Eq. 4.1, then the OML approach and simulation results are in agreement within 4% and 10%, in the collected current and inferred density respectively. This demonstrates that the OML analytic model for a drifting plasma can predict with relatively good accuracy the particle collection of a spherical probe for the ionospheric plasma conditions considered, this however, requires additional information such as ion concentration and their respective temperatures. The point to note here is that assuming that the ionospheric plasma is composed of 100% O^+ when minority ions are indeed present, yields relatively large uncertainties in the inferred plasma density, and that these occur even under optimal conditions for particle collection, in which an isolated sphere collects current, in the absence of any nearby object.

4.3.2 ION CURRENTS. SWARM PROBES

Simulation results for the collected currents by the Swarm Langmuir probes are now presented for more representative geometrical conditions. The obvious difference in space configuration is the presence of the Swarm ram segment where the 4 mm radius spherical probes are mounted on a post of 9.53 cm length as illustrated in Fig. 4.2. In this configuration, the satellite represents an obstacle between plasma and probe. In addition, owing to floating potential of the satellite, and the proximity of the probe, the sheath electric field of the spacecraft can deflect particles in the vicinity of the

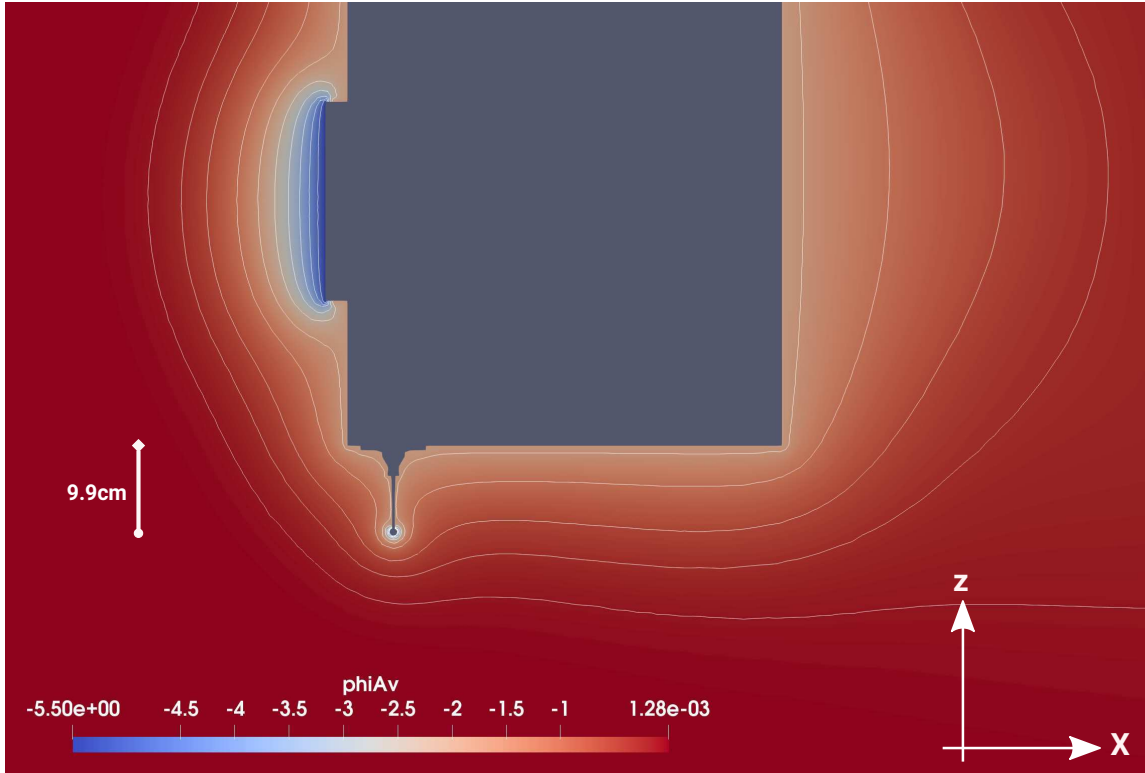


Figure 4.10: Cross-section of electric potential when the spherical Langmuir probe is operated in the ion saturation region. In this case, the satellite floating potential is set at $V_f = -2$ V, the front-plate is at -3.5 V and the spherical probe at -2.5 V, both with respect to the spacecraft. The plasma density is $n = 1 \times 10^{10} \text{ m}^{-3}$, the electron temperature is $T_e = 0.156$ eV, whereas the plasma flow velocity is $v_d = 7673$ m/s. The color bar “phiAV” refers to the electric potential averaged in time at steady state.

probe thus affecting its characteristics.

Figure 4.10 shows a cross-section of the electric potential profile for one of the cases considered. The white lines surrounding the satellite are equipotentials representing the electric sheath of the satellite, including the spherical probe and the front plate when is operated as a planar Langmuir probe. The plasma conditions considered in Fig. 4.10 consist of a density $n = 1 \times 10^{10} \text{ m}^{-3}$ and electron temperature $T_e = 0.156$

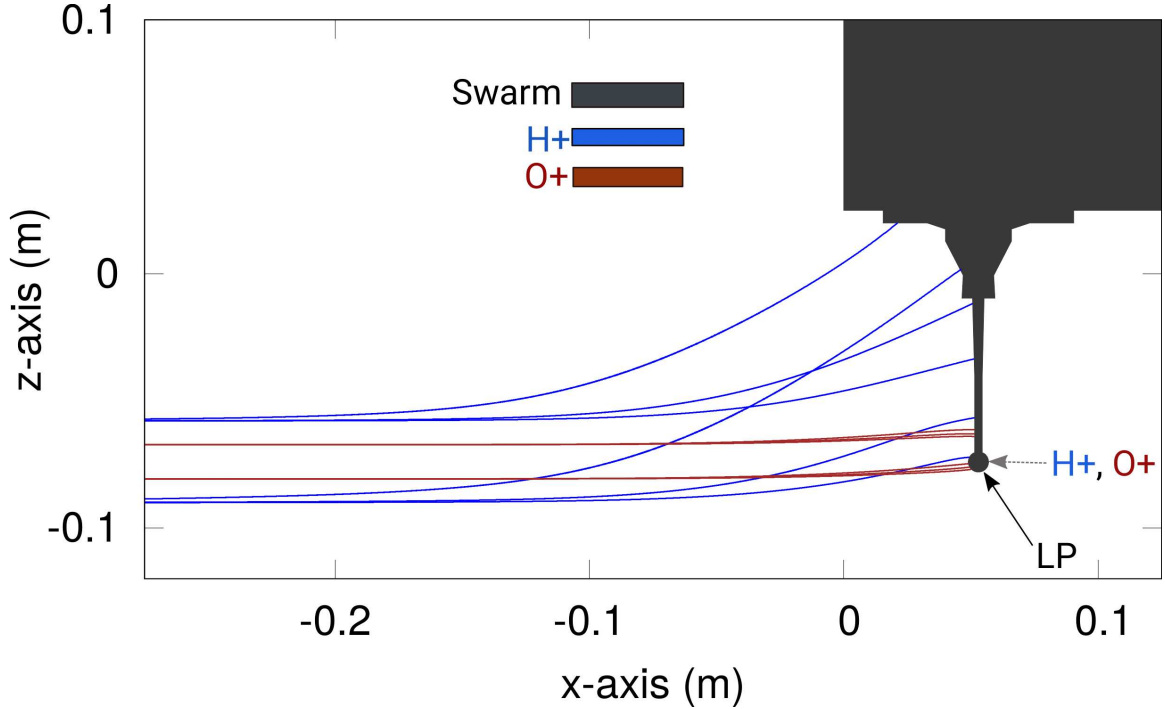


Figure 4.11: O^+ and H^+ ion trajectories deflected in the satellite sheath when the spherical probes are operated in the ion saturation region. Both species are aimed slightly below or above the spherical probe with velocities exactly from the ram direction. Ideally, the incoming ions would be collected by the probe (grey arrow). Three speeds are considered corresponding to v_{ram} , and $v_{ram} \pm v_{th}$ with $v_{th} = \sqrt{2kT/m}$ being the species thermal speed. Particles with the lower speed ($v_{ram} - v_{th}$) are deflected the most, and the ones with the higher speed ($v_{ram} + v_{th}$) are deflected the least.

eV. The spherical probes are biased with respect to the spacecraft to -2.5 V, and the front plate to -3.5 V. In this case, the floating potential is assumed to be -2 V.

As for an isolated sphere, the electric potential shown in Fig. 4.10 for a probe attached to the spacecraft, can be used to calculate particle trajectories. In Fig. 4.11, the same twelve particles, six H^+ and six O^+ , are launched from the boundary towards the spherical probe. In the absence of satellite, the ions would follow the same trajectories as in Fig. 4.8 since they were launched from the same positions and with the same

velocities, v_{ram} and $v_{ram} \pm v_{th}$. However, Fig. 4.11 shows that the presence of the satellite affects those trajectories significantly. H^+ ions are strongly deflected by the spacecraft sheath electric field compared to O^+ , due to their lower mass. In Fig. 4.12, thirty-eight ions, nineteen H^+ and nineteen O^+ , are launched at different angles from the boundary aimed at the center of the sphere. A single velocity has been considered in this case, $|\vec{v}| = \sqrt{v_{ram}^2 + v_{th}^2}$. As in Fig. 4.11, a considerable portion of lighter ions that would contribute to the probe net current are collected by the post and satellite bus instead. The electric field in the satellite sheath also causes particles coming from below that would miss the probe in the absence of the satellite sheath, to be deflected and collected. However the satellite sheath electric field below the probes is weaker than the one between the probes and the spacecraft. As a result, more particles are deflected away from the probe toward the spacecraft, than are deflected to the probe from below, resulting in a net reduction in the ion collected current. Note that the situation is different when the probe is biased positively to collect electrons. In this case, assuming a negative spacecraft floating potential, incoming electrons are repelled in the spacecraft sheath region.

When the satellite is included in the simulation, two independent probe measurements are obtained, labeled as $LP1$ and $LP2$ in Tables B.4 - B.22, where LPA refers to the average of the two probes. The 2% relative differences between simulated currents from the two probes provide an estimate of the uncertainty in the simulations. In this case, uncertainties can be attributed in part to statistical errors, and in part to the use of a grid with finite spatial resolution in the simulations. When referring to currents or calculated plasma density of Tables B.4 - B.23, for cases in which the satellite is included in the simulations, the reference will be the average values.

Tables B.4 - B.22 list currents calculated from kinetic simulations I_{sim} , while accounting for the spacecraft sheath effects. In the tables, B.4 - B.22, $\epsilon_{I_{OML}}$ and $\epsilon_{I_{OML16}}$

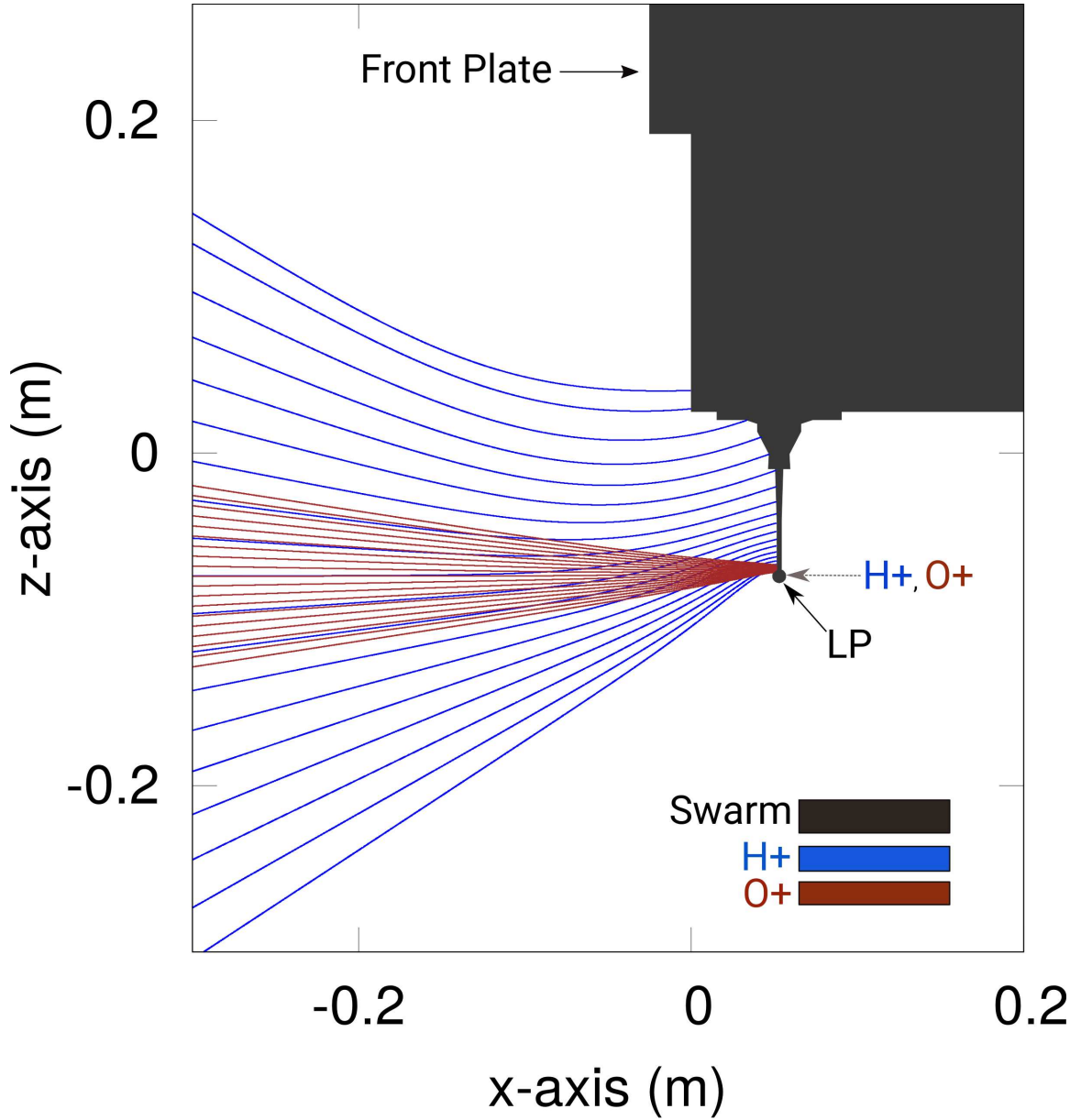


Figure 4.12: O^+ and H^+ ion trajectories deflected in the satellite sheath when the spherical probes are operated in the ion saturation region. In all cases, the magnitude of the incident velocity is equal to $\sqrt{v_{ram}^2 + v_{th}^2}$, where $v_{th} = \sqrt{2kT/m}$ is the ion thermal speed. The incoming particles have different incident angle. The grey arrow shows where H^+ and O^+ ions would impact if they were not deflected.

are the relative differences in current defined respectively as in 4.20 and 4.21 in the previous section. Values under $\delta_{I_{sim}}$ are the relative uncertainties in the calculated currents from simulations. The negative sign in the relative differences tabulated in B.4 - B.22, indicates that currents calculated from simulations are underestimated when are compared to those predicted by Eq. 4.1. Positive values on the other hand, indicate that the computed currents are overestimated compared to ones estimated with Eq. 4.18. Because the separation between the satellite bus and the probes is only 9.53 *cm* in the simulations, there are cases where the electric sheath thickness is comparable to this separation length. In simulations, due to the deflection of ions towards the satellite, the current collected by the probes is lower than that collected by an isolated probe as predicted with Eq. 4.1. Overestimations in the simulated currents with respect to the predicted one with Eq. 4.18, come from the fact that the contribution of the lighter ions to the collected current is not accounted for in Eq. 4.18 in which plasma ions are assumed to consist of 100% O^+ . The largest relative difference in each column are highlighted in bold. The maximum underestimation in the current is 48%, while the maximum overestimation of 56% is obtained when only O^+ ions are assumed.

The discrepancy in currents calculated from kinetic simulations and theory affects the accuracy of the inferred plasma densities. In Table B.23 relative errors in inferred densities are presented. Similarly to what has been shown in the previous subsection, the density has been calculated using three different approaches. In Table B.23, ϵ_{n_I} is the relative difference between the density obtained from Eq. 4.1 with the use of the current from simulations, and the density used as input in the kinetic simulations. In the table, ϵ_n and $\epsilon_{n_{16}}$ refer to the relative error between the density calculated using the admittance in Eqs. 4.6 and 4.19 respectively, and the one used as input in the simulations. δ_{n_I} and δ_n , are the uncertainties in the inferred densities calculated from

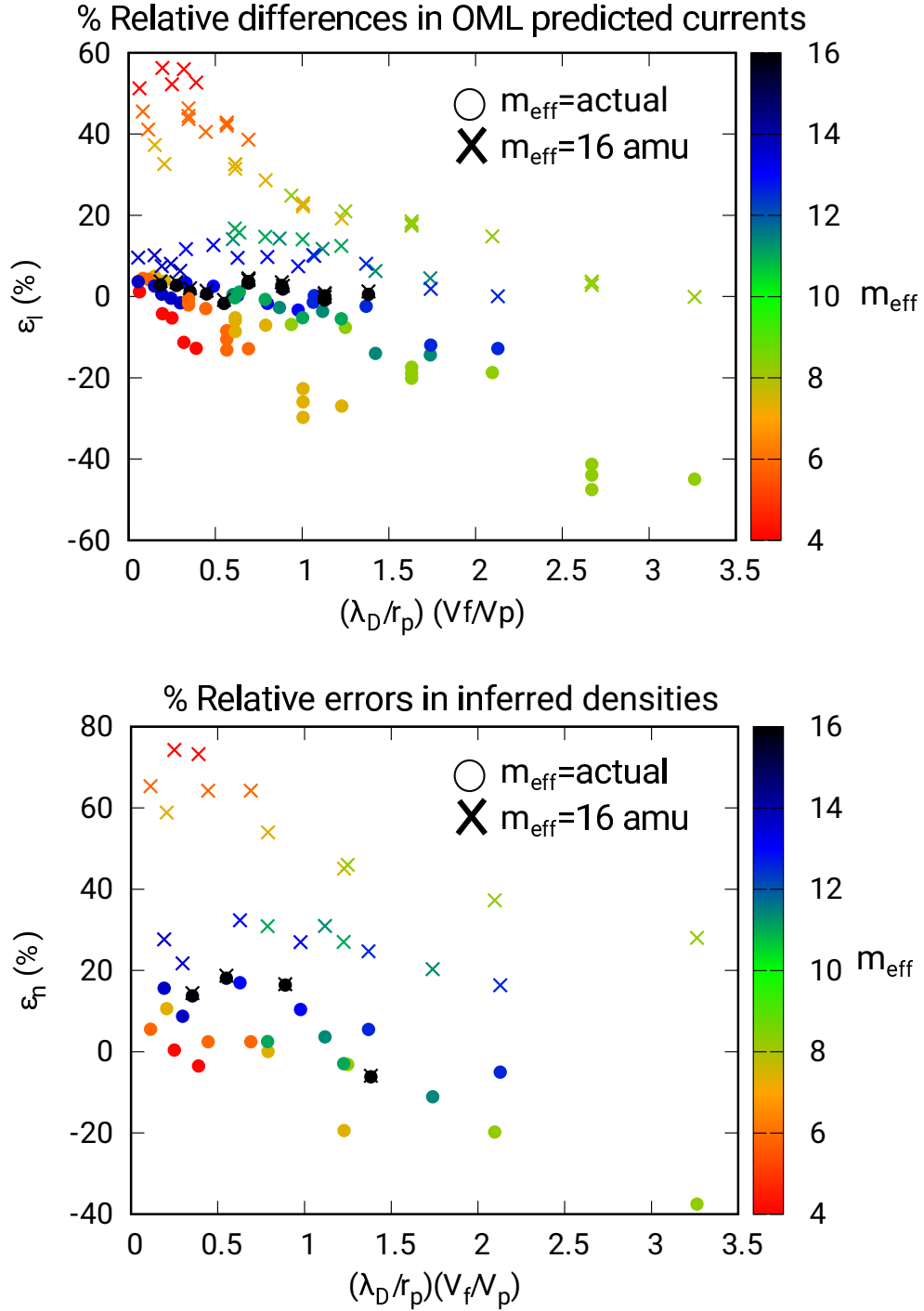


Figure 4.13: Top: Relative error in currents from simulations compared to those predicted with OML, I_{OML} from Eq. 4.1, and I_{OML16} from 4.18. Bottom: Relative error in inferred density with respect to the one used as input in the simulations. n_{OML} is obtained from Eq. 4.6, and n_{OML16} from 4.19. The probes are mounted on the Swarm bus.

simulated currents and admittances respectively. Note that in Table B.23, in some cases where the density is calculated from the computed admittance, the magnitude of the calculated uncertainty in the inferred density is larger than the calculated relative error. Results obtained in such cases are not conclusive for this study. The discrepancies in the simulated currents and relative errors in the inferred densities are plotted in Fig. 4.13, top and bottom respectively. Here, the relative differences and errors are on the y axis while on the x axis, the same ratio $(\lambda_D/r_p)(V_f/V_p)$ as in Fig. 4.9 is used as a rough measure of the satellite electric sheath strength.

The deflection of ions towards the satellite bus has a strong effect on the inferred densities. The admittance calculated from simulated currents under a strong influence of the Swarm electric sheath are underestimated compared to the theoretical values as illustrated in Fig. 4.14. This leads to underestimations up to 43% in the inferred plasma density. In Fig. 4.14 the solid lines are the currents predicted with the OML approach, the purple line corresponds to Eq. 4.1 (*OML*) whereas the green line to Eq. 4.18 (*OML₁₆*). The colored dots represent simulation results for different cases:

1. A single probe is simulated without the presence of the satellite and the floating potential is calculated self-consistently at $V_f = -0.512$ V (L_p in blue circles).
2. The two probes are attached to Swarm and the floating potential is calculated self-consistently at $V_f = -0.504$ V (V_f in navy diamonds).
3. The probes are attached to Swarm and the floating potential is set at $V_f = -1.0$ V (V_{f_1} in orange triangles).
4. The probes are attached to Swarm and the floating potential is set at $V_f = -2.0$ V (V_{f_2} in inverted red triangles).

In this example, the plasma density used in the simulations is $n = 1 \times 10^{10}$ m⁻³, with

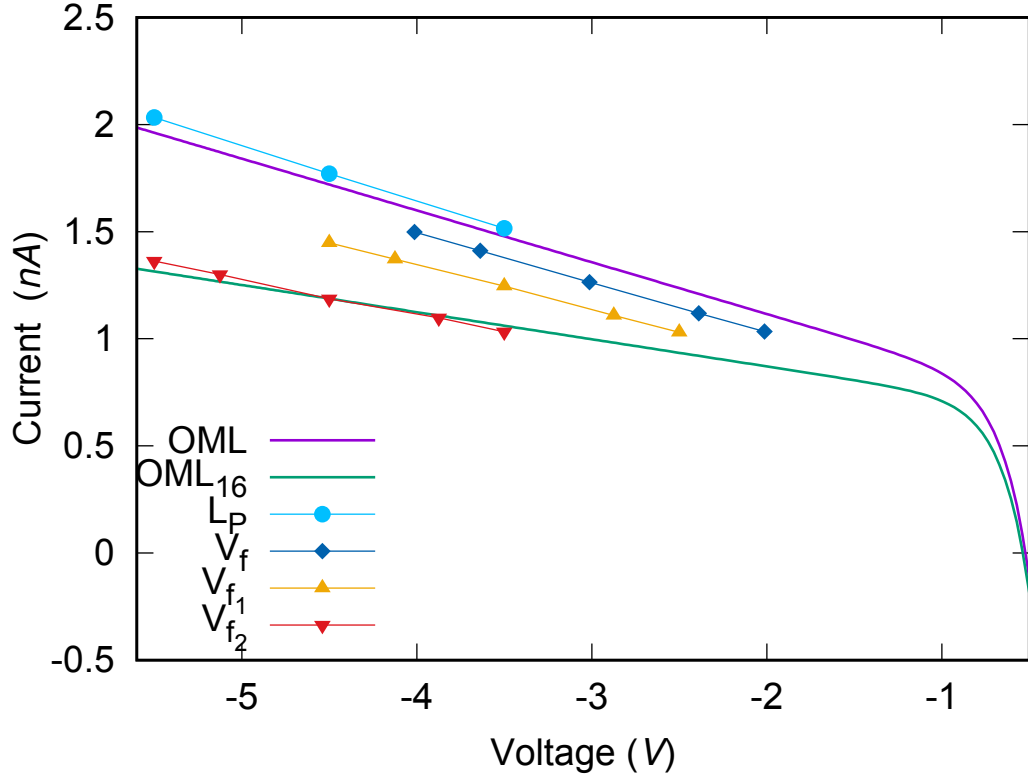


Figure 4.14: Ion saturation region example results. This case includes collected currents when the satellite floating potential V_f is varied from the one calculated self-consistently to -1 and -2 V. Results for the sphere simulated without the presence of the satellite, and those predicted by the OML theory are also shown for comparison. The plasma density, the electron temperature, and plasma flow velocity in all cases are $n = 1 \times 10^{10} \text{ m}^{-3}$, $T_e = 0.156 \text{ eV}$, $v_d = 7673 \text{ m/s}$ respectively.

an electron temperature of $T_e = 0.156 \text{ eV}$, which gives a Debye length of $\lambda_D = 29.4 \text{ mm}$. The effective ion mass is $m_{eff} = 8.3 \text{ amu}$. In Fig. 4.14 it is observed that as the floating potential becomes more negative, the deflection of minority light ions towards the satellite is enhanced leading to a reduction in the magnitude of the admittance. The theoretical model used in Swarm to infer the plasma density neglects the minority light ion contribution to the collected current. Then, in the presence of light ions, as for example in Fig. 4.14, the currents from simulations are larger than those

predicted by the analytic expression Eq. 4.18 (green solid line). The calculated currents where the satellite floating potential is varied, fall between those currents measured under ideal conditions (Eq. 4.1 and blue circles), and the currents predicted by Eq. 4.18. If the reduced currents from simulations are used in the theoretical model where the minority light ion contribution to the net currents is neglected, this results in overestimations up to 76% in the calculated density. In Fig. 4.14 the currents represented by the red inverted triangles are apparently in good agreement with the expression Eq. 4.18, however, in the calculation of the plasma density the admittance or slope of the I-V characteristic is what determines the inferred values. In this case, it is clear by inspecting the plot that the slope from simulation results is larger in magnitude than the one from Eq. 4.18 in the solid green line.

4.4 ELECTRON TEMPERATURE

Kinetic simulation results from the electron retardation and linear region are now presented. The data obtained from the electron linear region is used along with the ion saturation region to determine the voltage corresponding to the electron retardation region. With retardation and ion saturation region data, the electron temperature can then be calculated using Eq. 4.17.

The electron linear region in Swarm is measured at 0.7 V with respect to the floating potential of the spacecraft, that is $V_{lin} = V_f + 0.7$ V. Because this region is defined in terms of the floating potential V_f , it is important to understand how that varies with space plasma conditions. In table B.3 floating potential are listed for different plasma parameters and geometrical configurations. In the table, V_f^{Swarm} is the floating potential calculated from simulations when the spherical probes and a Swarm satellite are considered in the simulation domain. V_f^{LP} is the floating potential obtained from simulations when the probe is the only object in the domain. V_f^{OML} is the floating

potential predicted in the OML approximation (Eqs. 4.1 and 4.2). A point to note in Table B.3 is that the floating potential varies approximately linearly with the electron temperature T_e , independently of the objects considered in the simulation domain. As T_e increases, the energy of the electrons rises, as a consequence the satellite becomes more negative in order to repel electrons and maintain a net zero collected current. Inspecting Table B.3, it is clear that floating potentials estimated from the OML analytic approach are more negative than those calculated from simulations. As a result, the probe characteristic obtained in the OML approximation is shifted horizontally to the left compared to those calculated from simulations.

The differences in floating potentials yield enhanced discrepancies when currents and voltages calculated with OML are compared with those from simulations. When the probe is operated in the electron retardation and linear regions, currents estimated from OML are always significantly larger than those calculated for simulations if the difference in floating potential is not accounted for. In order to better compare the currents from simulations with those predicted in the OML approximation, in Tables B.24 and B.25 where currents from the electron linear and retardation regions are listed, the differences in floating potential are accounted for in the calculation of relative differences. In other words, the OML voltages and their respective currents, have been shifted in the horizontal axis of the probe characteristic by the difference in floating potential when comparing with simulated currents,

$$V_p^{OML} = V_p^{sim} + (V_f^{OML} - V_f^{sim}), \quad (4.25)$$

then the comparison is made between $I_{sim}(V_p^{sim})$ and $I_{OML}(V_p^{OML})$, where

$$I_{OML}(V_p^{OML}) \equiv I_{OML}(V_p^{sim} + (V_f^{OML} - V_f^{sim})). \quad (4.26)$$

Here, I_{sim} is the current calculated from kinetic simulations when the probe at V_p^{OML} , I_{OML} is the current that OML theory predicts (Eq. 4.2) for a given voltage V_p^{OML} which depends on: probe potential used in simulations V_p^{sim} , the floating potential predicted with the OML approximation V_f^{OML} , and the floating potential calculated self-consistently from simulations V_f^{sim} .

4.4.1 ELECTRON CURRENTS. ISOLATED PROBE

The electron retardation and linear regions have been simulated for only two space plasma conditions. However, the two geometrical configurations for the probe have been used for each set of plasma parameters, that is, when the sphere is the only object in the simulation domain, and the other being the spherical probe attached to the satellite. In addition, two orientations of background magnetic field have been used in combination with the geometrical and plasma parameter configurations. These cases correspond to two orientations of the geomagnetic field at mid-latitudes.

In Fig. 4.15 an example of a cross-section of the charge density and the electric potential profile (white contours) are shown from one of the cases simulated. The probe in this case is biased to $V = V_f + 0.7$ V where $V_f = -0.504$ V. The plasma density and electron temperature used are $n = 1 \times 10^{10}$ m⁻³ and $T_e = 0.156$ eV, respectively. The background magnetic field in this case is set to zero. Using the electric potential profile shown in Fig. 4.15, particle trajectories were calculated and these are shown in Fig. 4.16. Electrons are launched from equidistant points from the spherical probe center (red dots), with velocities of magnitude equal to $\sqrt{v_{ram}^2 + v_{th}^2}$, where $v_{th} = \sqrt{2kT_e/m}$ is the electron thermal speed. All injected electrons are aimed at the center of the sphere, as seen in Fig. 4.16, and because the electron thermal velocity is much larger than the drift velocity, electrons can reach the probe from all directions. The color bar in Fig. 4.16 represents the variations of the particle

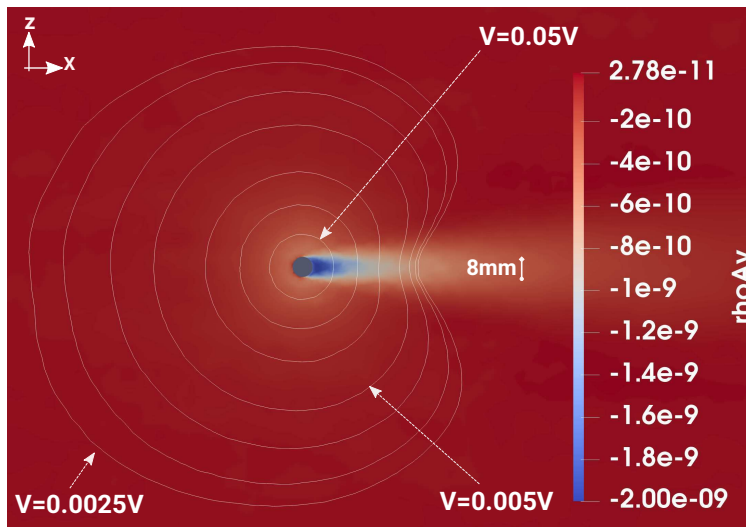


Figure 4.15: Cross-section of the charge density, with electric equipotentials when the spherical Langmuir probe is operated in the electron linear region. The probe voltage is $V_f + 0.7$ V, where the satellite floating potential is $V_f = -0.504$ V; both voltages are with respect to the plasma. In this case, the plasma density is $n = 1 \times 10^{10} \text{ m}^{-3}$, the electron temperature is $T_e = 0.156$ eV, and the plasma flow velocity is $v_d = 7673$ m/s. The background magnetic field is zero.

trajectories in the y plane. In this case, the launched electrons exhibit variations in their y coordinate due to discretization errors in the integration of particle trajectories, caused by the mesh finite resolution. Such variation however, are negligibly small compared to the dimensions of the probe allowing all injected electrons reach the probe.

Once the magnetic field is accounted for, the charge density and electric potential profile change from the one observed in Fig. 4.15 to the one shown in Fig. 4.17. All variables are the same as in the previous case except that a background magnetic field ($\vec{B} = (36.6, 0, 8.56) \mu T$) is now assumed in the simulations. The thermal gyroradius for the two electron temperatures considered are approximately between 5 and 4 cm . The electron motion near the probe is shown in Fig. 4.18, where particle trajectories

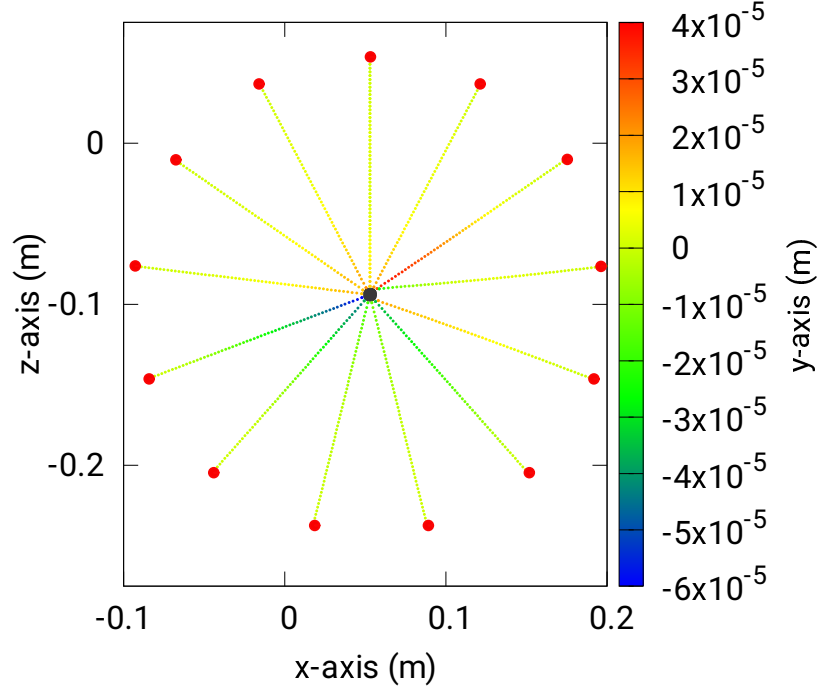


Figure 4.16: Electron trajectories calculated when the spherical probe is operated in the electron linear region. In all cases, the magnitude of the incident velocity is equal to $\sqrt{v_{ram}^2 + v_{th}^2}$, where $v_{th} = \sqrt{2kT/m}$ is the electron thermal speed. The incoming particles have different incident angles. All electrons reach the spherical probe. In this case, the background magnetic field is zero. Particles are launched at $y = 0.0$ m. The color code represents the variations in y coordinate.

were calculated using the electric potential profile shown in Fig. 4.17. In Fig. 4.18, electrons are launched in similar conditions as in Fig. 4.16. Here however, due to the presence of the background magnetic field, the electrons gyrate along field lines. As in Fig. 4.16, the color bar shows particle deviations along the y axis. Because of the gyration, stronger variations along the y axis are observed in this case. Considering the floating potential differences and the fact that in the OML theory, the magnetic field contribution to particle collection is not accounted for, currents from simulations remain relatively similar to the ones predicted by the OML approximation. A more

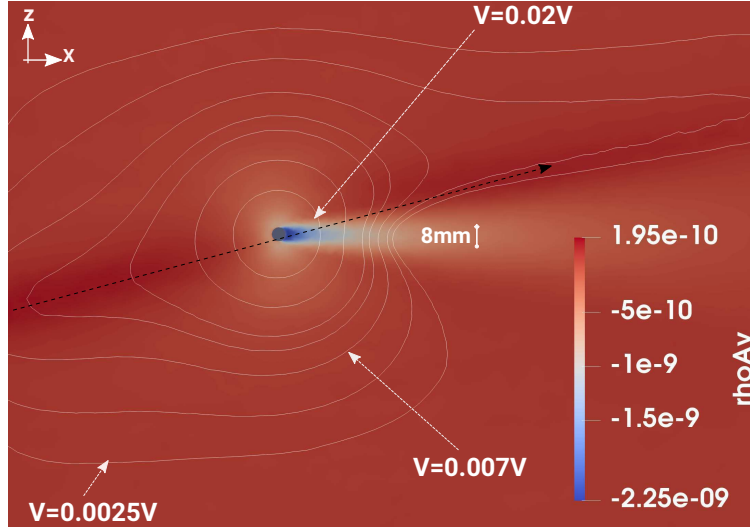


Figure 4.17: Cross-section of the charge density, with electric equipotentials when the spherical Langmuir probe is operated in the electron linear region. The probe voltage is $V_f + 0.7$ V, the satellite floating potential is $V_f = -0.503$ V, both with respect to the plasma. In this case, the plasma density is $n = 1 \times 10^{10} \text{ m}^{-3}$, the electron temperature is $T_e = 0.156$ eV, whereas the plasma flow velocity is $v_d = 7673$ m/s. The magnitude of the background magnetic field (black arrow) is $37.6 \mu\text{T}$.

detailed discussion is presented below.

4.4.2 ELECTRON CURRENTS. SWARM PROBES

When the satellite is included in the simulations, the charge density and electric potential surrounding the spherical probe is greatly modified compared to the one shown in Fig. 4.15 and even 4.17. Figure 4.19 shows how the presence of the satellite (with a floating potential $V_f = -2$ V) modifies the electric field sheath near the probe. The plasma conditions considered in this example are the same as in Fig. 4.15, where the magnetic field is set to zero. The dotted lines in Fig. 4.19 show the two orientations of magnetic field considered in the simulations. In Fig. 4.20 particle trajectories calculated using the electric profile in 4.19 (with $\vec{B} = 0$) are shown. Electrons (red dots) are injected at speeds equal to their thermal velocity plus the

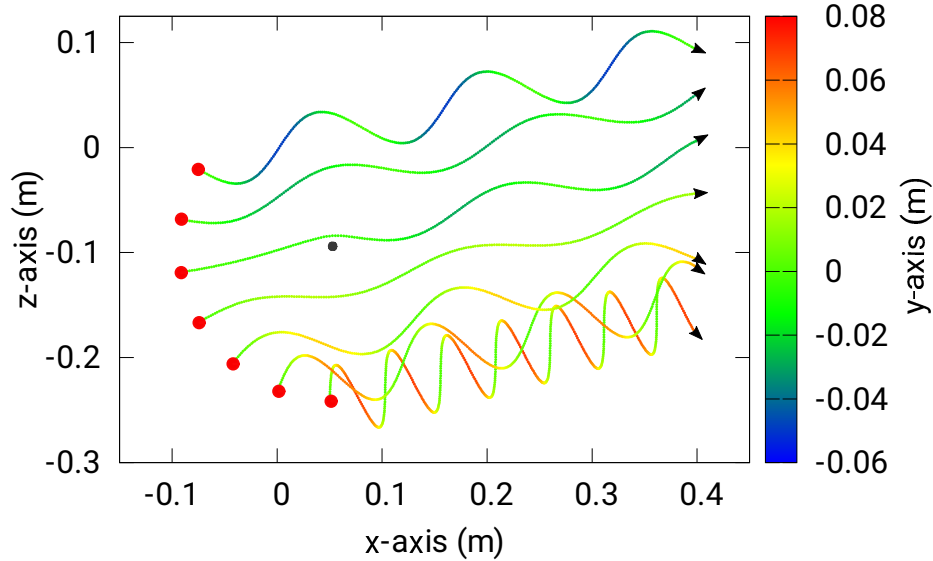


Figure 4.18: Electron trajectories calculated when the spherical probe is operated in the electron linear region. Particles gyrate due to the presence of a background magnetic field. In all cases, the magnitude of the incident velocity is equal to $\sqrt{v_{ram}^2 + v_{th}^2}$, where $v_{th} = (2kT/m)^{1/2}$ is the electron thermal speed. The incoming particles have different incident angles. Electrons would impact the spherical probe if they were not gyrating. Particles are launched at $y = 0.0$ m. The color code represents the variations in y coordinate.

drift velocity. Due to electric fields associated with the spacecraft sheath, most of electrons missed the spherical probe, contrary to what was observed in Fig. 4.16. The repelled electrons in the Swarm sheath yield a reduction in the probe collected current.

When a background magnetic field $\vec{B} = (36.6, 0, 8.56) \mu T$, is included in the simulations, electron motion observed from calculated trajectories is shown in Fig. 4.21. Electrons launched towards the probe gyrate along field lines as predicted, however, this motion is modified by the satellite electric field sheath which extends up to the wake in comparison to what is observed in Fig. 4.18 where the satellite is not accounted. The electron trajectories in Fig. 4.21 may suggest that none or a few of the

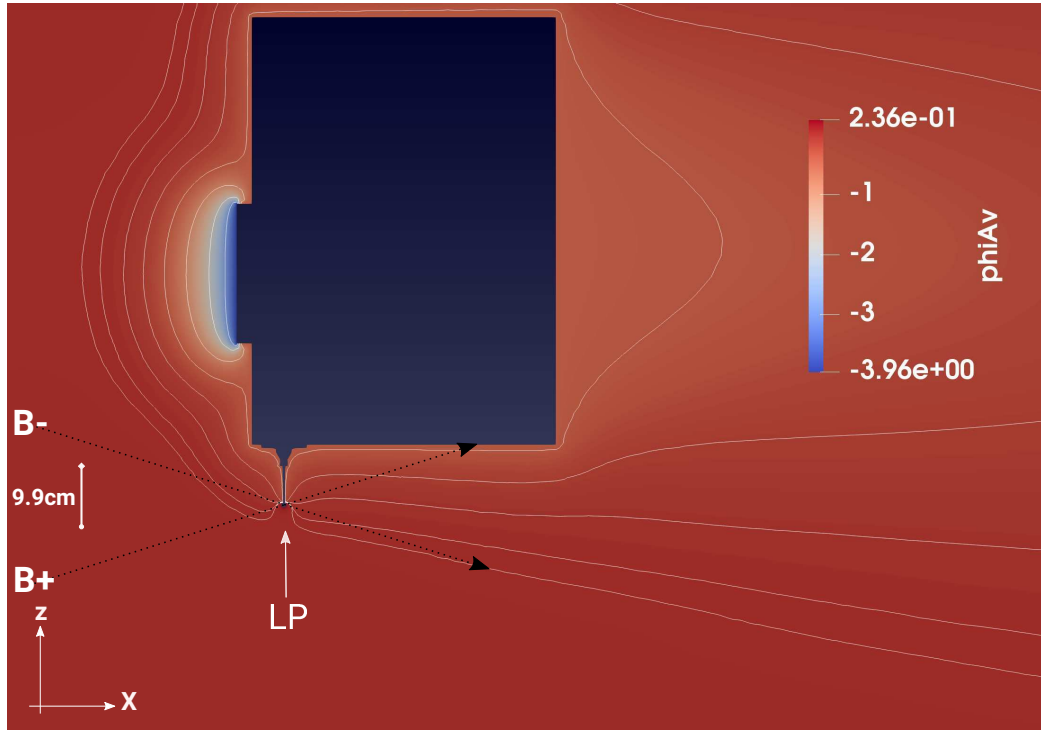


Figure 4.19: Cross-section of electric potential when the spherical Langmuir probe is operated in the electron linear region. In this case, the floating potential is set to $V_f = -2$ V, the front-plate is biased to -3.5 V and the spherical probe to 0.7 V, both with respect to the spacecraft. The plasma density is $n = 1 \times 10^{10} \text{ m}^{-3}$, the electron temperature is $T_e = 0.156$ eV, whereas the plasma flow velocity is 7673 m/s. Black dotted lines represent the two orientations of background magnetic field considered in the simulations. The color bar “phiAV” refers to the electric potential averaged in time at steady state.

launched particles reach the probe. However, results in Tables B.24 and B.25, show that although the magnetic field has an effect in the collected currents, such currents are comparable to those calculated without the presence of magnetic field.

Tables B.24 and B.25 contain the calculated currents from simulations for the two sets of plasma parameters considered, while the presence of the satellite and magnetic field were varied. These two cases of plasma parameters, taken as a examples to explore

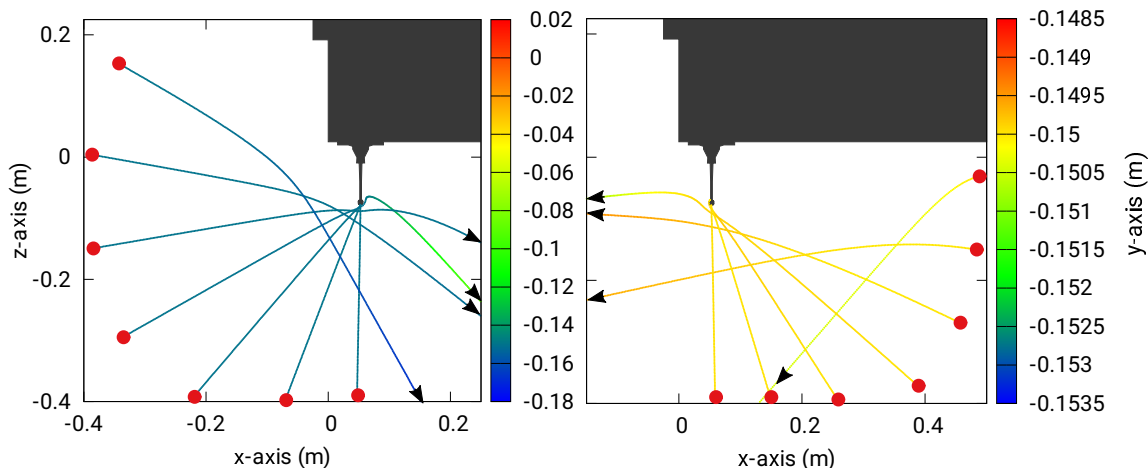


Figure 4.20: Electron trajectories deflected due to the satellite electric field sheath when the spherical probe is operated in the electron linear region. In all cases, the magnitude of the incident velocity is equal to $\sqrt{v_{ram}^2 + v_{th}^2}$, where $v_{th} = \sqrt{2kT/m}$ is the electron thermal speed. The incoming particles have different incident angle. Electrons would impact the spherical probe if they were not deflected. In this case, the background magnetic field is zero. Particles are launched at $y = 0.15$ m where the color code represents the variations in y coordinate. In this case the satellite floating potential is -0.514 V, and the probe biased to 0.7 V with respect to the spacecraft.

the interpretation of the electron temperature, are those where the influence of the satellite electric sheath was observed to be one of the strongest (Table B.24) and one of the weakest (Table B.25), in the plasma density analysis. In the tables, V_p is the probe voltage. I_p is the net current calculated from simulations, ϵ_{I_p} is the relative difference between current from simulations and the one predicted by OML $((I_p - I_{OML})/I_p)$, remembering that here, in the calculation of I_{OML} , the difference in floating potential between simulations and the one predicted by OML has been accounted as in Eq. 4.26. δ_{I_p} is the uncertainty in the calculated current from simulations. The column labeled *Swarm(Yes/No)* refers to the presence or absence of the satellite in the simulation domain, and where the \pm sign in $|\vec{B}|$ along the magnitude of the field, indicates the

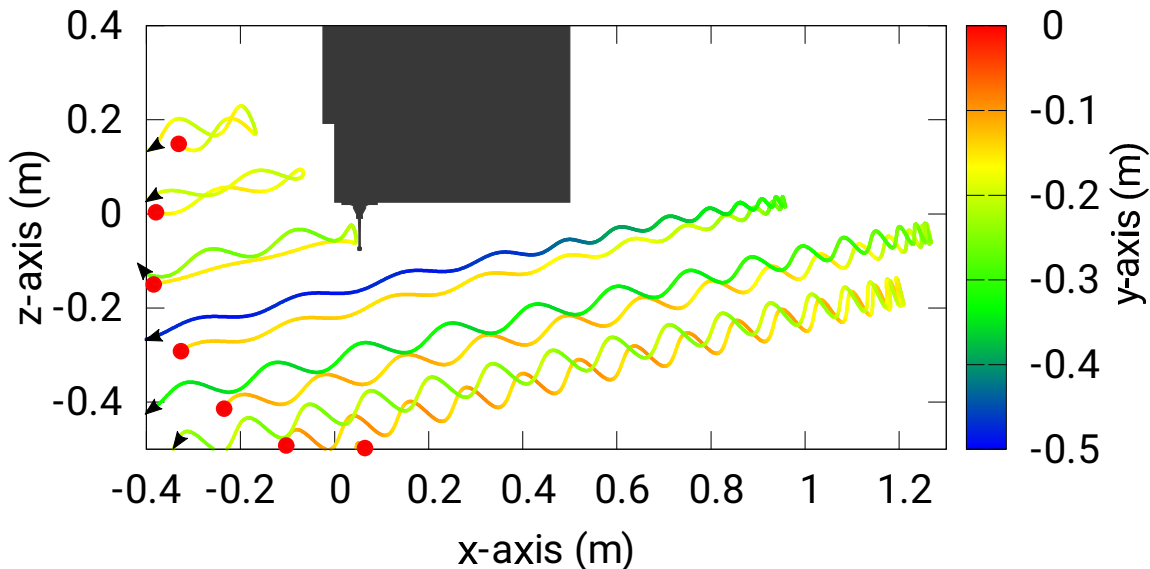


Figure 4.21: Electron trajectories deflected due to the satellite sheath electric field when the spherical probe is operated in the electron linear region. Particles gyrate due to the presence of a background magnetic field. In all cases, the magnitude of the incident velocity is equal to $\sqrt{v_{ram}^2 + v_{th}^2}$, where $v_{th} = \sqrt{2kT/m}$ is the electron thermal speed. The incoming particles have different incident angle. Electrons would impact the spherical probe if they were not gyrating. Particles are launched at $y = -0.15$ m where the color code represents the variations in y coordinate. In this case the spacecraft floating potential is -0.465 V, and the probe is biased to 0.7 V with respect to the spacecraft.

sign of B_z .

4.4.3 RETARDATION REGION

To estimate the electron retardation region, one pair of current-voltage were calculated in the electron linear region, one at $V_f + 0.7V$ and the other at $V_f + 1V$. The retardation region was found by interpolating the slopes, the one from the electron linear region with the one from the ion saturation. That is, assuming a linear dependence of the current with applied voltage in the ion saturation and electron linear

regions, these currents are equal at the retardation voltage V_{ret} , then

$$I_{ion}(V_{ret}) = I_{o_{ion}} + d_{ion}V_{ret} \quad (4.27)$$

$$I_{lin}(V_{ret}) = I_{o_{lin}} + d_{lin}V_{ret} \quad (4.28)$$

$$\begin{aligned} I_{ion}(V_{ret}) &= I_{lin}(V_{ret}) \\ V_{ret} &= \frac{I_{o_{ion}} - I_{o_{lin}}}{d_{ret} - d_{ion}}. \end{aligned} \quad (4.29)$$

In Eq. 4.29, $I_{o_{ion}}$ and $I_{o_{lin}}$ are the characteristic currents predicted by the assumed linear dependence of the current at zero voltage, for the ion saturation and electron linear region respectively. Following this, simulation results in the ion saturation region and linear region were used to calculate these values as follow:

$$I_{o_{ion}} = I_{ion}(V_{ion}) - d_{ion}V_{ion} \quad (4.30)$$

$$I_{o_{lin}} = I_{lin}(V_{lin}) - d_{lin}V_{lin}, \quad (4.31)$$

where I_{ion} and V_{ion} , as well as I_{lin} and V_{lin} , are current-voltage pairs calculated from simulations for the ion saturation and electron linear region respectively. d_{ion} and d_{lin} are the slopes calculated numerically using current-voltage simulation data for each region. Once the retardation voltage was found, simulations to calculate the retardation current were done. Additionally, two more currents were calculated at voltages $V_{ret} \pm = V_{ret} \pm 0.029 V$, in order to obtain the admittance.

4.4.4 INFERRED ELECTRON TEMPERATURE

With the voltages and corresponding currents in the retardation region given in Tables B.24 and B.25, along with their respective ion saturation data, the electron temperature was inferred from Eq. 4.17. The results in Table B.26 for the temperatures inferred from kinetic simulation results using the Swarm data processing

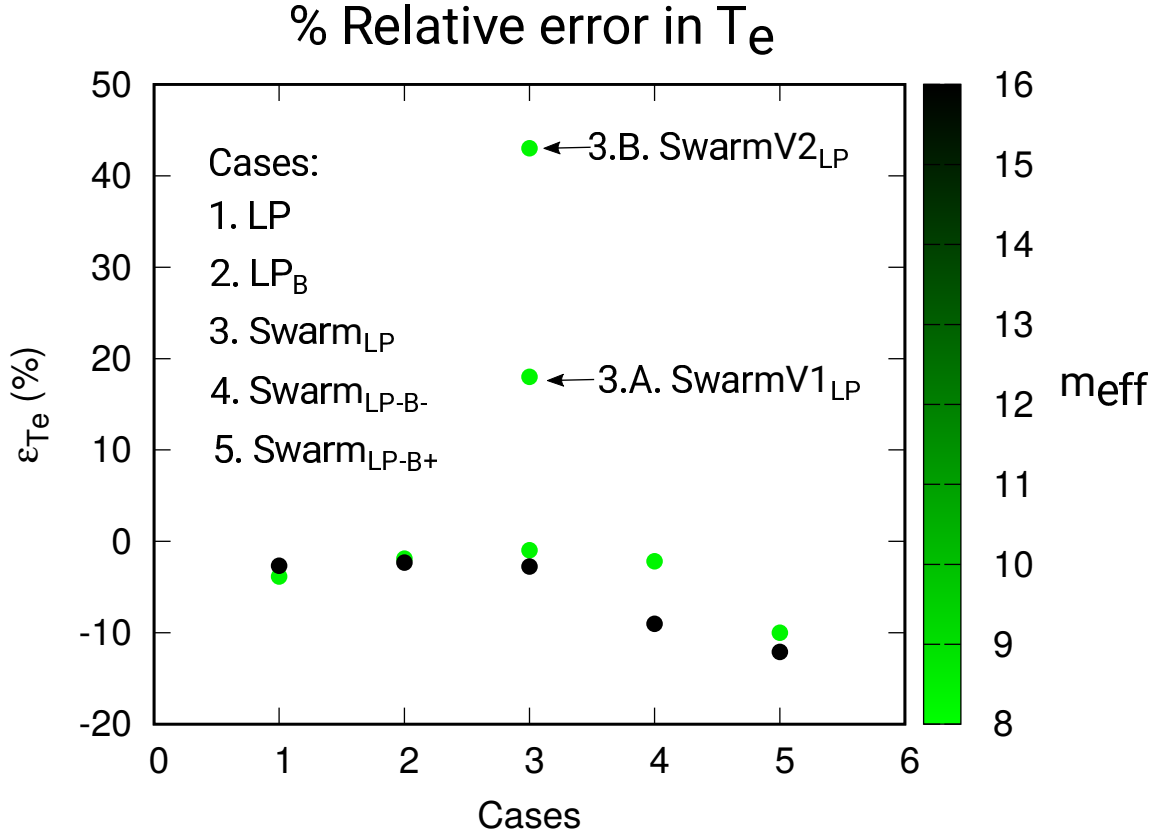


Figure 4.22: Relative errors in inferred electron temperature compared to T_e used as input in the simulations. The relative errors are plotted along the y axis. In the x axis, the different cases considered are listed as follows: LP corresponds to the case of the isolated probe and $\vec{B} = 0$. In LP_B , the probes is isolated and $\vec{B} \neq 0$. In $Swarm_{LP}$, the probe is mounted on Swarm and $\vec{B} = 0$. In $SwarmV1_{LP}$, the probe is mounted on Swarm, while $V_f = -1$ V, and $\vec{B} = 0$. In $SwarmV2_{LP}$, the probe is mounted on Swarm, while $V_f = -2$ V, and $\vec{B} = 0$. In $Swarm_{LP-B-}$, the probe is mounted on Swarm and $\vec{B} \neq 0$, and it is magnetically disconnected. Finally, in $Swarm_{LP-B+}$, the probe is mounted on Swarm and $\vec{B} \neq 0$, and it is magnetically connected.

algorithm, are plotted in Fig. 4.22. In B.26, ϵ_{T_e} is the relative error between the inferred temperature and the one used as input in the simulations. δ_{T_e} is the uncertainty in the calculated electron temperature. The $-$ and $+$ signs in ϵ_{T_e} indicate that the inferred temperature is respectively an underestimation and overestimation of the actual temperature assumed in the simulations.

With both sets of plasma parameters considered, the relative errors in the inferred temperature remain below 4%, except for those where the satellite is present and the magnetic field is not zero. When the satellite is included, but the background magnetic field is zero, the calculated temperature also remains accurate within 4%. Two orientations of the magnetic field have been considered, $\vec{B} = (36.6, 0, \pm 8.56)$, corresponding to two possibilities for magnetic flux tubes from which electrons can be collected by the probes. When B_z is negative, field lines crossing the spherical probe do not intersect any other part of the satellite. In this case, gyrating electrons confined to flux tubes can reach the probes from all directions. This configuration is referred to as “*magnetically disconnected*”. The relative error in the calculated electron temperature, shown in table B.26 and Fig. 4.22, when the probe is magnetically disconnected, do not exceed 2% for the first case of plasma parameters, as seen in Table B.24, while for the second case, B.25, the error can be approximately 9%. With B_z positive, the field lines connect the spherical probe with the bottom of the satellite bus, and this configuration is referred to as “*magnetically connected*”. In the two cases considered, the electron temperature is underestimated by 10% and 12%. This indicates that under magnetic connection, the presence and orientation of the magnetic field with respect to the probe and satellite affects the electron collection and should be accounted for in the interpretation of the probe characteristics.

In the presence of a magnetic field, electrons are confined to magnetic flux tubes of radius of the order two thermal gyroradii. Since in ionospheric plasma, the electron

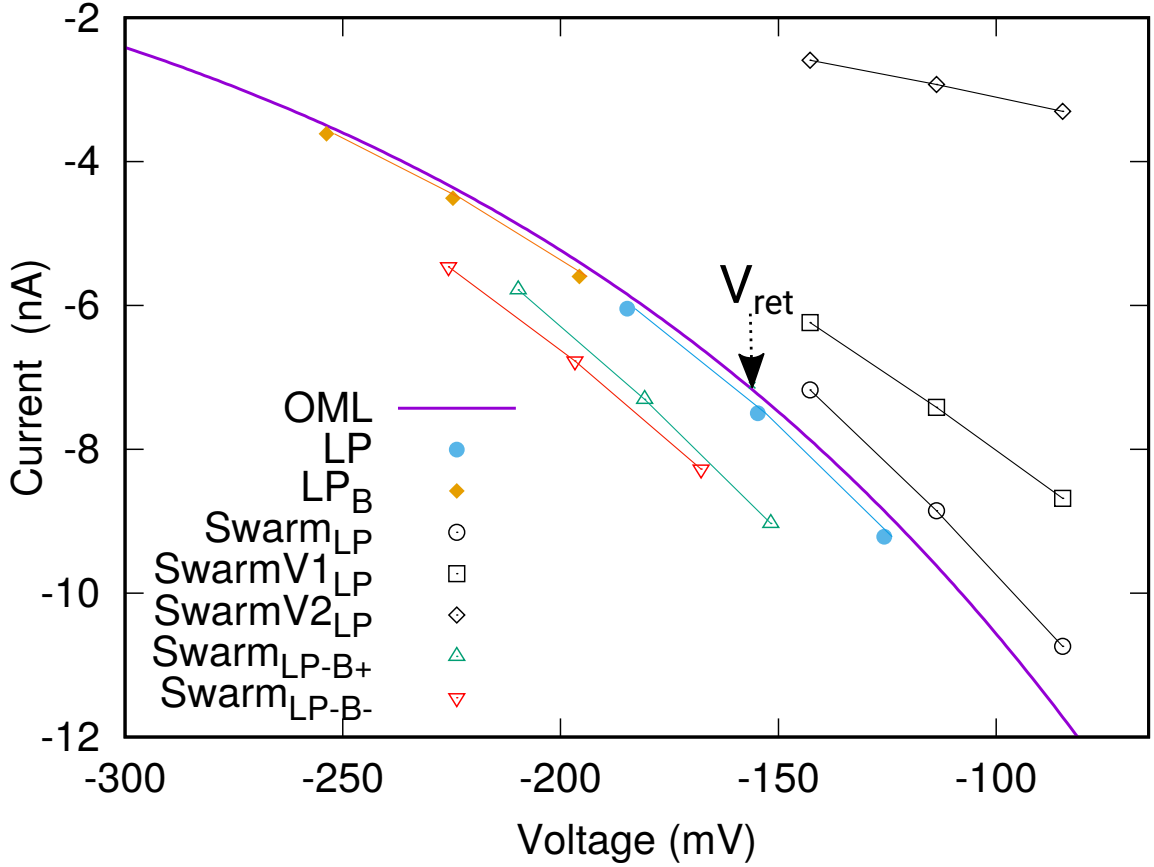


Figure 4.23: Electron retardation currents calculated from simulations. The solid line correspond to the currents predicted with the OML theory, Eq. 4.2. The different data points correspond to the different configurations considered as in Fig. 4.22. In simulations the plasma density used is $n = 10^{10} \text{ m}^{-3}$, and an electron temperature $Te = 0.156 \text{ eV}$.

thermal gyroradius is more than 10 times larger than the Swarm probe radius, incoming electrons are collected approximately as if they were unmagnetized. This is why for an isolated probe, in the absence of any nearby object, the collected current is independent of the magnetic field.

The floating potential of the spacecraft was varied only for the first case of plasma parameters while no magnetic field was included. Simulations were made with $V_f = -1, -2 \text{ V}$ in addition to the one calculated self-consistently. It is found that the

satellite electric sheath repels incoming electron that otherwise would be collected by the probe, thus reducing the collected currents and hence, the admittance, as illustrated in Fig. 4.23. In 4.23, the simulated currents for the cases where the floating potential were set to -1 and -2 V, are labeled as “*SwarmV1_{LP}*” and “*SwarmV2_{LP}*” respectively. The other labels in Fig. 4.23 follow the same descriptions as in Fig. 4.22. The estimated temperatures are found to be overestimated by up to 18% and 43% with respect to the one used as input in the simulations, corresponding to spacecraft floating potentials of -1 , and -2 V, respectively. The satellite electric sheath then has an impact on the electron temperature accuracy comparable to the one observed in the plasma density inferred from ion currents.

CHAPTER 5.

SUMMARY AND CONCLUSIONS

In this thesis, current collection by the Swarm front plate and Langmuir probes is studied under more realistic conditions than those accounted for in the analytic model used to interpret probe measurements. The study is conducted by using particle-in-cell (PIC) simulations to calculate collected currents that are used as input in the methodology derived from Orbital Motion Limited (OML) theory as in the actual Swarm. Discrepancies in the estimated parameters are found and associated with plasma conditions that are not accounted for in the theoretical model used to interpret probe measurements, then providing a better understanding of the physics involved and allowing improvements in such interpretations.

The main objective of the thesis is to simulate the response of two particle sensors that are part of the Electric field instrument (EFI) under different environment conditions, in order to assess the accuracy of the algorithms currently used to infer plasma parameters. Particular attention is given to:

1. Understanding and quantifying the relation between the current collected by the EFI front plate when is used as a planar Langmuir probe.
2. Assess the accuracy of the algorithms used to infer plasma density and electron temperature from Swarm spherical probes measurements.

The thesis also presents and illustrates a method for suppressing the self-force on particles in the general PIC approach.

SELF-FORCE

A general method was presented to remove the non-physical "self-force" which appears in most Particle-in-Cell (PIC) models. The method consists of precomputing an array of electric fields by successively assigning a unit charge to each node in the mesh while setting zero charges at other nodes. The resulting electric fields at this node, as well as at other nodes to which it is connected in a given cell are then tabulated. This array can then be used to interpolate the self-electric field at a particle position in a given element (tetrahedron). These tabulated fields can then be used to subtract self-forces at every particle positions in a PIC simulations.

One advantage of this method is that, in addition to removing self-forces, it also removes the unphysical force associated with mirror charges at the simulation domain outer boundary, when Dirichlet boundary conditions are applied. This advantage at the outer boundary however, is a disadvantage at physical boundaries where, owing to Dirichlet boundary conditions, image charges and associated forces are physically correct. It is noted however, that the self-force subtraction method presented here, would only remove the force associated with a given particle's own image charge. Image charges of other nearby particles would be "seen" by a particle, and they would affect its dynamics. In particular, if two simulation particles occupied the same position in space at a given time, none would be affected by its own self-electric field, but each would be affected by the self-electric field of the other.

Finally, the magnitude of the acceleration of an electron in a finite density plasma is found to be orders of magnitude larger than that caused by the self-force or by the image charge at a boundary. It should then be acceptable to ignore the self-force in most plasma simulations. Should there be special cases where the self-force needs to be removed however, the method presented would prove accurate and efficient.

SWARM FRONT PLATE AS PLANAR LANGMUIR PROBE

The Swarm front plate is used as planar Langmuir probe for additional plasma diagnostics when the thermal ion imagers embedded in the plate are not in operation. Measured ion currents are found experimentally to be appreciably larger than those expected assuming a collection surface equal to the geometrical plate area. Using results from kinetic simulations with representative ionospheric plasma conditions, it is possible to quantify relative enhancements in the front plate effective cross-section. These enhancements are caused by the deflection of incident ions by fringe electric fields around the plate. Light ions are particularly affected, and even in small concentrations, they contribute proportionally significantly more to the relative enhancement than heavier ions. Similarly, ions incident with lower ram speeds are deflected more than ions incident at higher speeds. A good approximation to the enhancement was constructed using a semi-empirical fit involving relevant plasma environment parameters including:

1. The electron Debye length, thus, plasma density and electron temperature.
2. The spacecraft floating potential.
3. The ion effective mass.
4. The plasma flow velocity.

The strength and extent of the sheath electric field around the plate increases as the potential becomes more negative with respect to background plasma. With a fixed bias voltage of -3.5 V with respect to the spacecraft, the plate's effective collection surface area varies with the satellite floating potential.

SWARM SPHERICAL LANGMUIR PROBES

Simulations were also made to assess the accuracy of the OML analytic expressions used to process Swarm spherical Langmuir probe measurements. This was done by simulating collected probe characteristics under a representative range of ionospheric plasma conditions, and applying the same algorithm as used in actual Swarm data processing. Two geometries were considered, consisting of i) a single isolated spherical probe, and ii) a probe attached to a post below a truncated ram segment of Swarm. Comparing densities and temperatures inferred from simulated currents, with known ones used in the simulations, then provides an assessment of the OML-based methodology. OML inferences are found to be in excellent agreement with simulation results obtained for an isolated probe provided that ion mass distributions be taken into account in both simulations and OML. Inferred densities however, show a marked dependence on minority light ion concentration and along-track plasma speeds. This in turn leads to discrepancies compared to predictions made with the assumption that plasma consists of 100% O^+ ions, with along-track flow speed equal to the satellite orbital speed.

With a more realistic geometry, in which a portion of satellite bus and the probe post were accounted for, significant discrepancies in the characteristics between simulations and OML, were found in all cases. The proximity of the probe to the spacecraft bus (~ 10 cm from the bottom) puts it in the spacecraft electric sheath, which then affects the trajectory particles to be collected. With negative biasing, when collecting electrons, the presence and orientation of the geomagnetic field is also found to affect characteristics. Neither the proximity of the Swarm bus, nor magnetic fields are accounted for in OML or Swarm probe data processing.

FUTURE WORK AND OPEN QUESTIONS

The results presented in this study shed light on the physical processes and plasma conditions involved in particle collection of the Swarm probes. Future work involving a broader range in parameter space while addressing some of the assumptions made in this first study, would allow the development of an improved methodology to interpret Swarm probe in situ measurements. Other than standard approximations made in computer simulations, such as using a finite grid to represent fields and geometry, the physical model considered in simulations also entail approximations, including:

1. Drifting Maxwellian distribution for the background plasma. This approximation should be valid at mid latitudes, but it would likely break down at high latitudes, where energetic non-Maxwellian particle distribution are expected, depending on space weather conditions.
2. Photoelectron and secondary electron emissions were also neglected for simplicity. Emitted electrons would likely return to the probes when their voltages are positive, but they would escape when they are negative. This would affect measured collected front plate, and spherical probe measurements in which electron losses would count as a positive ion collection. Emitted electrons from other parts of the spacecraft could also travel to, and be collected by the probes thus affecting measurements.

LANGMUIR PROBE MEASUREMENT CHALLENGE.

From the results and discussions presented in the previous chapter, it is clear that Langmuir probe characteristic depend on a number of parameters characterizing the state of a plasma, as well as on several physical processes and geometrical conditions. As seen in Chapter 3 and 4, the main challenge, in order to better interpret probe

measurements, is that probe characteristics are not only dependent on the density and temperature, but also on other parameters and conditions which are not necessarily known or diagnosed. These include for example, the ion composition, particularly the presence of light minority ions, the plasma flow velocity in the spacecraft reference frame, the proximity to other satellite components and their sheath electric fields, and the spacecraft floating potential. As such, the probe interpretation problem can be seen as an undetermined inverse problem in which, in the absence of more diagnostics, it is necessary to assume values for some of these parameters, or neglect the geometry in which measurements are made. This is the case for example, with Swarm probe data analysis, with the assumptions of pure O^+ plasma, along-track flow speed equal to the satellite orbital speed, and the neglect of the sheath electric field near the satellite body. As a result, the inferred plasma parameters unavoidably come with uncertainties which, in the absence of independent measurements, are difficult to assess. This predicament is what motivated this thesis, in which several conditions not accounted in the analytic expressions used in the interpretation of probe measurements, were accounted for in kinetic computer simulations. By comparing inferred parameters using the same algorithm as for Swarm data, with input values used in the simulations, error estimates have been made for different plasma environment conditions. The empirical model derived for the density in Chapter 3 can be used to estimate errors in inferred densities when certain assumptions are made concerning the ion composition and along-track flow speed. In Chapter 4, several physical processes were shown to affect spherical probe measurements in ways not accounted for with OML. Here however, no empirical model was derived as in Chapter 3, because of the higher complexity of the problem, which also depends on the satellite sheath electric field, the magnitude, and direction of the geomagnetic field. As such, Chapter 4 does not answer as many questions as Chapter 3, but it points to further studies

needed to better understand and parametrise Swarm spherical probe measurements. It also demonstrates the importance of non-ideal effects in several cases.

In conclusion, kinetic simulations prove to be a valuable tool for studying the effect of physical and geometrical effects on satellite particle sensors measurements, under more realistic conditions than possible using analytic expressions. Such simulations can in principle be used to infer plasma parameters such as the density and temperature, from measurements. Finally, to the extent possible, sensor measurement campaigns, particularly in space, should be preceded and accompanied with relevant theoretical and simulation support in order to optimize scientific output.

REFERENCES

- [1] Gerd Pröls. *Physics of the Earths space environment: an introduction*. Springer Science & Business Media, 2012.
- [2] Margaret G Kivelson and Christopher T Russell. *Introduction to space physics*. Cambridge university press, 1995.
- [3] Wolfgang Baumjohann and Rudolf A Treumann. *Basic space plasma physics*. World Scientific Publishing Company, 2012.
- [4] Steven A Cummer. Modeling electromagnetic propagation in the earth-ionosphere waveguide. *IEEE Transactions on Antennas and Propagation*, 48(9):1420–1429, 2000.
- [5] Carl Greifinger and Phyllis Greifinger. Approximate method for determining elf eigenvalues in the earth-ionosphere waveguide. *Radio Science*, 13(5):831–837, 1978.
- [6] B Jayachandran, N Balan, PB Rao, JH Sastri, and GJ Bailey. Hf doppler and ionosonde observations on the onset conditions of equatorial spread f. *Journal of Geophysical Research: Space Physics*, 98(A8):13741–13750, 1993.
- [7] Stanimir M Stankov, Koen Stegen, Plamen Muhtarov, and Rene Warnant. Local ionospheric electron density profile reconstruction in real time from simultaneous ground-based gnss and ionosonde measurements. *Advances in Space Research*, 47(7):1172–1180, 2011.

REFERENCES

- [8] Gregory Breit and Merle A Tuve. A radio method of estimating the height of the conducting layer. *Nature*, 116(2914):357, 1925.
- [9] Robert Morris Page. The early history of radar. *Proceedings of the IRE*, 50(5):1232–1236, 1962.
- [10] T Hagfors, Wk Birkmayer, and M Sulzer. A new method for accurate ionospheric electron density measurements by incoherent scatter radar. *Journal of Geophysical Research: Space Physics*, 89(A8):6841–6845, 1984.
- [11] T Hagfors and M Lehtinen. Electron temperature derived from incoherent scatter radar observations of the plasma line frequency. *Journal of Geophysical Research: Space Physics*, 86(A1):119–124, 1981.
- [12] Cathryn N Mitchell and Paul SJ Spencer. A three-dimensional time-dependent algorithm for ionospheric imaging using gps. *Annals of Geophysics*, 46(4):687–696, 2003.
- [13] George A Hajj and Larry J Romans. Ionospheric electron density profiles obtained with the global positioning system: Results from the gps/met experiment. *Radio Science*, 33(1):175–190, 1998.
- [14] Irina Zakharenkova, Elvira Astafyeva, and Iurii Cherniak. Gps and in situ swarm observations of the equatorial plasma density irregularities in the topside ionosphere. *Earth, Planets and Space*, 68(1):120, 2016.
- [15] LH Brace, NW Spencer, and George R Carignan. Ionosphere electron temperature measurements and their implications. *Journal of Geophysical Research*, 68(19):5397–5412, 1963.

REFERENCES

- [16] Larry H Brace. Langmuir probe measurements in the ionosphere. *Geophysical Monograph-American Geophysical Union*, 102:23–36, 1998.
- [17] Stephen Mitchell Wolfe, KJ Button, J Waldman, and DR Cohn. Modulated submillimeter laser interferometer system for plasma density measurements. *Applied optics*, 15(11):2645–2648, 1976.
- [18] D E TF Ashby and DF Jephcott. Measurement of plasma density using a gas laser as an infrared interferometer. *Applied Physics Letters*, 3(1):13–16, 1963.
- [19] GF Swadling, SV Lebedev, GN Hall, S Patankar, NH Stewart, RA Smith, AJ Harvey-Thompson, GC Burdiak, P de Grouchy, J Skidmore, et al. Diagnosing collisions of magnetized, high energy density plasma flows using a combination of collective thomson scattering, faraday rotation, and interferometry. *Review of Scientific Instruments*, 85(11):11E502, 2014.
- [20] G. Murphy, J. Pickett, N. d’Angelo, and W.S. Kurth. Measurements of plasma parameters in the vicinity of the space shuttle. *Planetary and Space Science*, 34(10):993 – 1004, 1986/10/.
- [21] G.B. Giffin, D. Hastings, and G.B. Shaw. Continued analysis of ion current collection in the plasma wake during the charging hazards and wake studies (chaws) experiment. pages 215 –, 1996//.
- [22] J Sayers. In-situ probes for ionospheric investigations. *Journal of Atmospheric and Terrestrial Physics*, 32(4):663–691, 1970.
- [23] D.L. Cooke, W. Pakula, V.A. Davis, M.J. Mandell, M. Tautz, and C.L. Enloe. Measurement and simulation of high voltage-wake interactions. pages 242 –, 1996//.

REFERENCES

- [24] JE Allen, RLF Boyd, and P Reynolds. The collection of positive ions by a probe immersed in a plasma. *Proceedings of the Physical Society. Section B*, 70(3):297, 1957.
- [25] James G Laframboise. Theory of spherical and cylindrical langmuir probes in a collisionless, maxwellian plasma at rest. Technical report, TORONTO UNIV DOWNSVIEW (ONTARIO) INST FOR AEROSPACE STUDIES, 1966.
- [26] J Rubinstein and JG Laframboise. Theory of a spherical probe in a collisionless magnetoplasma. *The Physics of Fluids*, 25(7):1174–1182, 1982.
- [27] MJM Parrot, LRO Storey, LW Parker, and JG Laframboise. Theory of cylindrical and spherical langmuir probes in the limit of vanishing debye number. *The Physics of Fluids*, 25(12):2388–2400, 1982.
- [28] JE Allen. Probe theory-the orbital motion approach. *Physica Scripta*, 45(5):497, 1992.
- [29] Walter R Hoegy and Larry H Brace. Use of langmuir probes in non-maxwellian space plasmas. *Review of scientific instruments*, 70(7):3015–3024, 1999.
- [30] I Katz, GA Jongeward, VA Davis, TL Morton, and DC Ferguson. Current collection by a large langmuir probe in a meso-thermal (ram) plasma. *GEOPHYSICAL MONOGRAPH-AMERICAN GEOPHYSICAL UNION*, 102:37–42, 1998.
- [31] Shu T Lai. An improved langmuir probe formula for modeling satellite interactions with near-geostationary environment. *Journal of Geophysical Research: Space Physics*, 99(A1):459–467, 1994.

REFERENCES

- [32] JG Laframboise and LJ Sonmor. Current collection by probes and electrodes in space magnetoplasmas: A review. *Journal of Geophysical Research: Space Physics*, 98(A1):337–357, 1993.
- [33] Isaac D Sudit and R Claude Woods. A study of the accuracy of various Langmuir probe theories. *Journal of applied physics*, 76(8):4488–4498, 1994.
- [34] Levan Lomidze, David J Knudsen, Johnathan Burchill, Alexei Kouznetsov, and Stephan C Buchert. Calibration and validation of swarm plasma densities and electron temperatures using ground-based radars and satellite radio occultation measurements. *Radio Science*, 53(1):15–36, 2018.
- [35] AG Burns, SC Solomon, Wenbin Wang, Liying Qian, Y Zhang, and LJ Paxton. Daytime climatology of ionospheric nmf2 and hmf2 from cosmic data. *Journal of Geophysical Research: Space Physics*, 117(A9), 2012.
- [36] Yen-Hsyang Chu, Chin-Lung Su, and Hsiao-Tsung Ko. A global survey of cosmic ionospheric peak electron density and its height: A comparison with ground-based ionosonde measurements. *Advances in Space Research*, 46(4):431–439, 2010.
- [37] Dieter Bilitza, David Altadill, Bodo Reinisch, Ivan Galkin, Valentin Shubin, and Vladimir Truhlik. The international reference ionosphere: Model update 2016. In *EGU General Assembly Conference Abstracts*, volume 18, 2016.
- [38] D Bilitza, D Altadill, V Truhlik, V Shubin, I Galkin, B Reinisch, and X Huang. International reference ionosphere 2016: From ionospheric climate to real-time weather predictions. *Space Weather*, 15(2):418–429, 2017.

REFERENCES

- [39] Joseph W Schumer and James Paul Holloway. Vlasov simulations using velocity-scaled hermite representations. *Journal of Computational Physics*, 144(2):626–661, 1998.
- [40] Tilman Dannert and Frank Jenko. Vlasov simulation of kinetic shear alfvén waves. *Computer physics communications*, 163(2):67–78, 2004.
- [41] Takayuki Umeda. A conservative and non-oscillatory scheme for vlasov code simulations. *Earth, planets and space*, 60(7):773–779, 2008.
- [42] Yasuhiro Idomura, H Urano, Nobuyuki Aiba, and S Tokuda. Study of ion turbulent transport and profile formations using global gyrokinetic full-f vlasov simulation. *Nuclear Fusion*, 49(6):065029, 2009.
- [43] Charles K Birdsall. Particle-in-cell charged-particle simulations, plus monte carlo collisions with neutral atoms, pic-mcc. *IEEE Transactions on Plasma Science*, 19(2):65–85, 1991.
- [44] Eric Sonnendrücker, John J Ambrosiano, and Scott T Brandon. A finite element formulation of the darwin pic model for use on unstructured grids. *Journal of Computational Physics*, 121(2):281–297, 1995.
- [45] Beniamino Di Martino, Sergio Briguglio, Gregorio Vlad, and Piero Sguazzero. Parallel pic plasma simulation through particle decomposition techniques. *Parallel Computing*, 27(3):295–314, 2001.
- [46] R-F Lottermoser, M Scholer, and AP Matthews. Ion kinetic effects in magnetic reconnection: Hybrid simulations. *Journal of Geophysical Research: Space Physics*, 103(A3):4547–4559, 1998.

REFERENCES

- [47] Keith Lewis Cartwright, John Paul Verboncoeur, and Charles Kennedy Birdsall. Nonlinear hybrid boltzmann–particle-in-cell acceleration algorithm. *Physics of Plasmas*, 7(8):3252–3264, 2000.
- [48] Zhihong Lin and Liu Chen. A fluid–kinetic hybrid electron model for electromagnetic simulations. *Physics of Plasmas*, 8(5):1447–1450, 2001.
- [49] Dan Winske, Lin Yin, Nick Omid, Homa Karimabadi, and Kevin Quest. Hybrid simulation codes: Past, present and futurea tutorial. In *Space plasma simulation*, pages 136–165. Springer, 2003.
- [50] Robert L Richard, Raymond J Walker, and Maha Ashour-Abdalla. The population of the magnetosphere by solar winds ions when the interplanetary magnetic field is northward. *Geophysical research letters*, 21(23):2455–2458, 1994.
- [51] Micháel Mendillo, Joshua Emery, and Brian Flynn. Modeling the moon’s extended sodium cloud as a tool for investigating sources of transient atmospheres. *Advances in Space Research*, 19(10):1577–1586, 1997.
- [52] Mei-Ching Fok, Thomas E Moore, and Dominique C Delcourt. Modeling of inner plasma sheet and ring current during substorms. *Journal of Geophysical Research: Space Physics*, 104(A7):14557–14569, 1999.
- [53] Satoshi Takeuchi. New particle accelerations by magnetized plasma shock waves. *Physics of plasmas*, 12(10):102901, 2005.
- [54] TE Moore, M-C Fok, MO Chandler, CR Chappell, SP Christon, DC Delcourt, J Fedder, M Huddleston, M Liemohn, WK Peterson, et al. Plasma sheet and (nonstorm) ring current formation from solar and polar wind sources. *Journal of Geophysical Research: Space Physics*, 110(A2), 2005.

REFERENCES

- [55] TE Moore, M-C Fok, DC Delcourt, SP Slinker, and JA Fedder. Global aspects of solar wind–ionosphere interactions. *Journal of Atmospheric and Solar-Terrestrial Physics*, 69(3):265–278, 2007.
- [56] F Mackay, R Marchand, K Kabin, and JY Lu. Test kinetic modelling of collisionless perpendicular shocks. *Journal of Plasma Physics*, 74(3):301–318, 2008.
- [57] Mats Holmström, Martin Wieser, Stas Barabash, Yoshifumi Futaana, and Anil Bhardwaj. Dynamics of solar wind protons reflected by the moon. *Journal of Geophysical Research: Space Physics*, 115(A6), 2010.
- [58] Richard Marchand. Test-particle simulation of space plasmas. *Communications in Computational Physics*, 8(3):471, 2010.
- [59] R Marchand, F Mackay, JY Lu, and K Kabin. Consistency check of a global mhd simulation using the test-kinetic approach. *Plasma Physics and Controlled Fusion*, 50(7):074007, 2008.
- [60] Saeed ur Rehman and Richard Marchand. Plasma-satellite interaction driven magnetic field perturbations. *Physics of Plasmas*, 21(9):090701, 2014.
- [61] S.U. Rehman, R. Marchand, J.-J. Berthelier, T. Onishi, and J. Burchill. Earth magnetic field effects on particle sensors on LEO satellites. *IEEE Trans. Plasma Sci. (USA)*, 41(12):3402 – 9, 2013/12.
- [62] DE Hastings. A review of plasma interactions with spacecraft in low earth orbit. *Journal of Geophysical Research: Space Physics*, 100(A8):14457–14483, 1995.
- [63] Daniel Hastings and Henry Garrett. *Spacecraft-environment interactions*. Cambridge university press, 2004.

REFERENCES

- [64] Elden C Whipple. Potentials of surfaces in space. *Reports on Progress in Physics*, 44(11):1197, 1981.
- [65] DJ Knudsen, JK Burchill, SC Buchert, AI Eriksson, R Gill, J-E Wahlund, L Åhlen, M Smith, and B Moffat. Thermal ion imagers and Langmuir probes in the swarm electric field instruments. *Journal of Geophysical Research: Space Physics*, 122(2):2655–2673, 2017.
- [66] Roger W Hockney and James W Eastwood. *Computer simulation using particles*. crc Press, 1988.
- [67] Phillip Colella and Peter C Norgaard. Controlling self-force errors at refinement boundaries for amr-pic. *Journal of Computational Physics*, 229(4):947–957, 2010.
- [68] Jay P Boris and Roswell Lee. Nonphysical self forces in some electromagnetic plasma-simulation algorithms. *Journal of Computational Physics*, 12(1):131–136, 1973.
- [69] D Vendor and Rod W Boswell. Numerical modeling of low-pressure rf plasmas. *IEEE Transactions on Plasma Science*, 18(4):725–732, 1990.
- [70] Christophe Cornet and Dixon TK Kwok. A new algorithm for charge deposition for multiple-grid method for pic simulations in r–z cylindrical coordinates. *Journal of Computational Physics*, 225(1):808–828, 2007.
- [71] R. Marchand. PTetra, a tool to simulate low orbit satellite-plasma interaction. *IEEE Trans. Plasma Sci. (USA)*, 40(2):217 – 29, 2012.

REFERENCES

- [72] Richard Marchand and Pedro Alberto Resendiz Lira. Kinetic simulation of spacecraft–environment interaction. *IEEE Transactions on Plasma Science*, 45(4):535–554, 2017.
- [73] W Fox, A Bhattacharjee, and K Germaschewski. Fast magnetic reconnection in laser-produced plasma bubbles. *Physical review letters*, 106(21):215003, 2011.
- [74] J Birn, JF Drake, MA Shay, BN Rogers, RE Denton, M Hesse, M Kuznetsova, ZW Ma, A Bhattacharjee, A Otto, et al. Geospace environmental modeling (gem) magnetic reconnection challenge. *Journal of Geophysical Research: Space Physics*, 106(A3):3715–3719, 2001.
- [75] PL Pritchett. Geospace environment modeling magnetic reconnection challenge: Simulations with a full particle electromagnetic code. *Journal of Geophysical Research: Space Physics*, 106(A3):3783–3798, 2001.
- [76] JF Drake, M Swisdak, H Che, and MA Shay. Electron acceleration from contracting magnetic islands during reconnection. *Nature*, 443(7111):553, 2006.
- [77] William Daughton, Jack Scudder, and Homa Karimabadi. Fully kinetic simulations of undriven magnetic reconnection with open boundary conditions. *Physics of Plasmas*, 13(7):072101, 2006.
- [78] Francis H Harlow and MW Evans. A machine calculation method for hydrodynamic problems. *LAMS-1956*, 1955.
- [79] Francis H Harlow. The particle-in-cell computing method for fluid dynamics. *Methods Comput. Phys.*, 3:319–343, 1964.

REFERENCES

- [80] Charles K Birdsall and Dieter Fuss. Clouds-in-clouds, clouds-in-cells physics for many-body plasma simulation. *Journal of Computational Physics*, 3(4):494–511, 1969.
- [81] O Buneman. Time-reversible difference procedures. *Journal of Computational Physics*, 1(4):517–535, 1967.
- [82] JM Dawson. Electrostatic sheet model for a plasma and its modification to finite-size particles. Technical report, Princeton Univ., NJ, 1970.
- [83] Roger W Hockney. The potential calculation and some applications. *Methods Comput. Phys.*, 9:136, 1970.
- [84] John M Dawson. Particle simulation of plasmas. *Reviews of modern physics*, 55(2):403, 1983.
- [85] John P Verboncoeur. Particle simulation of plasmas: review and advances. *Plasma Physics and Controlled Fusion*, 47(5A):A231, 2005.
- [86] CK Birdsall and AB Langdon. Plasma physics via computer simulation. 1985.
- [87] A Friedman, AB Langdon, and BI Cohen. A direct method for implicit particle-in-cell simulation. *Comments on plasma physics and controlled fusion*, 6(6):225–236, 1981.
- [88] John Villasenor and Oscar Buneman. Rigorous charge conservation for local electromagnetic field solvers. *Computer Physics Communications*, 69(2-3):306–316, 1992.
- [89] John P Verboncoeur, A Bruce Langdon, and NT Gladd. An object-oriented electromagnetic pic code. *Computer Physics Communications*, 87(1-2):199–211, 1995.

REFERENCES

- [90] Vahid Vahedi and G DiPeso. Simultaneous potential and circuit solution for two-dimensional bounded plasma simulation codes. *Journal of Computational Physics*, 131(1):149–163, 1997.
- [91] Vahid Vahedi and Maheswaran Surendra. A monte carlo collision model for the particle-in-cell method: applications to argon and oxygen discharges. *Computer Physics Communications*, 87(1-2):179–198, 1995.
- [92] Yasuhiko Sentoku and Andreas J Kemp. Numerical methods for particle simulations at extreme densities and temperatures: Weighted particles, relativistic collisions and reduced currents. *Journal of Computational Physics*, 227(14):6846–6861, 2008.
- [93] Paulett C Liewer and Viktor K Decyk. A general concurrent algorithm for plasma particle-in-cell simulation codes. *Journal of Computational Physics*, 85(2):302–322, 1989.
- [94] Sergio Briguglio, GREGORIO VLAD, BENIAMINO DI MARTINO, and PIERO SGUAZZERÒ. *Parallel pic plasma simulation through particle decomposition techniques*. ENEA, 1997.
- [95] U Fahleson. Laboratory experiments with plasma flow past unmagnetized obstacles. *Planetary and Space Science*, 15(10):1489–1497, 1967.
- [96] RL Morse and CW Nielson. Numerical simulation of the weibel instability in one and two dimensions. *The Physics of Fluids*, 14(4):830–840, 1971.
- [97] Alan C Tribble. *The space environment: implications for spacecraft design*. Princeton University Press Princeton, NJ, 2003.

REFERENCES

- [98] Satoshi Hosoda, Takanobu Muranaka, Hitoshi Kuninaka, Jeongho Kim, Shinji Hatta, Naomi Kurahara, Mengu Cho, Hiroko O Ueda, Kiyokazu Koga, and Tateo Goka. Laboratory experiments for code validation of multiutility spacecraft charging analysis tool (muscat). *IEEE Transactions on Plasma Science*, 36(5):2350–2359, 2008.
- [99] JP Boris. Relativistic plasma simulation-optimization of a hybrid code. In *Proc. Fourth Conf. Num. Sim. Plasmas, Naval Res. Lab, Wash. DC*, pages 3–67, 1970.
- [100] Hong Qin, Shuangxi Zhang, Jianyuan Xiao, Jian Liu, Yajuan Sun, and William M Tang. Why is boris algorithm so good? *Physics of Plasmas (1994-present)*, 20(8):084503, 2013.
- [101] H. M. Mott-Smith and Irving Langmuir. The theory of collectors in gaseous discharges. *Phys. Rev.*, 28:727–763, Oct 1926.
- [102] J G Laframboise. *Theory of spherical and cylindrical Langmuir probes in a collisionless, Maxwellian plasma at rest*. PhD thesis, University of Toronto, 1966.
- [103] Jen-Shih Chang and JG Laframboise. Probe theory for arbitrary shape in a large debye length, stationary plasma. *The Physics of Fluids*, 19(1):25–31, 1976.
- [104] JG Laframboise and J Rubinstein. Theory of a cylindrical probe in a collisionless magnetoplasma. *The Physics of Fluids*, 19(12):1900–1908, 1976.
- [105] Francis F Chen. Numerical computations for ion probe characteristics in a collisionless plasma. *Journal of Nuclear Energy. Part C, Plasma Physics, Accelerators, Thermonuclear Research*, 7(1):47, 1965.

REFERENCES

- [106] A Bergmann. Two-dimensional particle simulation of Langmuir probe sheaths with oblique magnetic field. *Physics of Plasmas*, 1(11):3598–3606, 1994.
- [107] AR Hoskinson and N Hershkowitz. Effect of finite length on the current–voltage characteristic of a cylindrical Langmuir probe in a multidipole plasma chamber. *Plasma Sources Science and Technology*, 15(1):85, 2006.
- [108] J Burchill. personal communication, 2018.
- [109] M Förster. personal communication, 2018.
- [110] Dieter Bilitza, David Altadill, Yongliang Zhang, Chris Mertens, Vladimir Truhlik, Phil Richards, Lee-Anne McKinnell, and Bodo Reinisch. The international reference ionosphere 2012—a model of international collaboration. *Journal of Space Weather and Space Climate*, 4:A07, 2014.
- [111] WJ Raitt and DC Thompson. Thermal plasma measurements in space using direct measurements of derivatives of probe current-voltage characteristics. *GEOPHYSICAL MONOGRAPH-AMERICAN GEOPHYSICAL UNION*, 102:43–48, 1998.
- [112] Marco Chiaretta. Numerical modelling of langmuir probe measurements for the swarm spacecraft, 2011.

APPENDIX A

In the Orbital Motion Limited Theory, the following assumptions are made:

- Maxwellian distribution functions are assumed for the particles

$$f(\vec{v}) = n \left(\frac{m}{2\pi kT} \right)^{3/2} \exp \left(-\frac{m|\vec{v} - \vec{v}_d|^2}{2kT} \right), \quad (\text{A.1})$$

where m and q are the mass and charge of the particle respectively. n is the number of particle per unit volume, \vec{v}_d is the drift velocity, T is the temperature, and k is the Boltzmann constant.

- Collisions between particle are negligible.
- The electron Debye length is much larger than the radius of the probe.
- There is no magnetic field
- There are no objects near the probe which would intersect or deflect incoming particles.
- Energy and angular momentum are conserved.

To calculate the particles collected by a spherical Langmuir of radius a , we first determine the effective cross section b of the sphere for particles coming towards it from a large distance. The maximum impact parameter b , will depend on its initial velocity v_0 , far from the probe and the probe bias voltage. Recalling OML assumptions, and considering that with incidence at impact parameter b , the collected

particle would have a trajectory tangent to the sphere, we can write the conservation of energy as

$$\frac{1}{2}mv_0^2 = \frac{1}{2}mv_1^2 + qV, \quad (\text{A.2})$$

and

$$mv_0b = mv_1a \quad (\text{A.3})$$

for conservation of angular momentum. These two equations, can be solved for b , and the results is

$$b = a\sqrt{1 - \frac{2qV}{mv_0^2}} \quad (\text{A.4})$$

Current Associated with Attracted Species

The current collected associated to an attracted species in spherical coordinates is given by

$$I = q \int_0^{2\pi} d\phi \int_0^\pi \sin(\theta) d\theta \int_0^\infty dv v^2 f(\vec{v}) \pi b^2 v. \quad (\text{A.5})$$

Making use of the expression for $f(\vec{v})$ in Eq.A.1, and b in A.4, we find

$$I = qn\pi a^2 \left(\frac{m}{2\pi kT}\right)^{3/2} \int_0^{2\pi} d\phi \int_0^\pi \sin(\theta) d\theta \int_0^\infty dv v^2 v \exp\left(-\frac{m|\vec{v} - \vec{v}_d|^2}{2kT}\right) \left(1 - \frac{2qV}{mv^2}\right) \quad (\text{A.6})$$

If for simplicity, we assume a drift velocity along z axis, and use the following change of variables

$$\mu = \cos(\theta), \quad (\text{A.7})$$

$$x = \frac{v}{\sqrt{2kT/m}}, \quad (\text{A.8})$$

$$x_d = \frac{v_d}{\sqrt{2kT/m}}, \quad (\text{A.9})$$

after the ϕ , θ , and μ integrals are evaluated, A.6 becomes

$$I = qn2\pi a^2 \left(\frac{2kT}{\pi m}\right)^{1/2} \int_0^\infty dx x^2 \frac{e^{-(x-x_d)^2} - e^{-(x+x_d)^2}}{2x_d} \left(1 - \frac{qV}{kTx^2}\right). \quad (\text{A.10})$$

If we now make the change of variable $s = x - x_d$, the first integral involving exponentials in A.10 can be evaluated as follow

$$\begin{aligned} \int_0^\infty dx x^2 e^{-(x-x_d)^2} &= \int_{-x_d}^\infty ds (s^2 + 2sx_d + x_d^2) e^{-s^2} \\ &= \frac{x_d}{2} e^{-x_d^2} + \left(\frac{1}{2} + x_d^2\right) \frac{\sqrt{\pi}}{2} [1 + \text{erf}(x_d)], \end{aligned} \quad (\text{A.11})$$

and

$$\int_0^\infty dx \frac{qV}{kT} e^{-(x-x_d)^2} = \frac{qV}{kT} \int_{-x_d}^\infty ds e^{-s^2} = \frac{qV}{kT} \frac{\sqrt{\pi}}{2} [1 + \text{erf}(x_d)]. \quad (\text{A.12})$$

For the second exponential, we obtain

$$\begin{aligned} \int_0^\infty dx x^2 e^{-(x+x_d)^2} &= \int_{x_d}^\infty ds (s^2 - 2sx_d + x_d^2) e^{-s^2} \\ &= -\frac{x_d}{2} e^{-x_d^2} + \left(\frac{1}{2} + x_d^2\right) \frac{\sqrt{\pi}}{2} [1 - \text{erf}(x_d)], \end{aligned} \quad (\text{A.13})$$

and

$$\int_0^\infty dx \frac{qV}{kT} e^{-(x+x_d)^2} = \frac{qV}{kT} \int_{x_d}^\infty ds e^{-s^2} = \frac{qV}{kT} \frac{\sqrt{\pi}}{2} [1 - \text{erf}(x_d)]. \quad (\text{A.14})$$

In the evaluation of both integrals involving exponentials, use is made of the expression for the error function

$$\operatorname{erf}(s) = \frac{2}{\sqrt{\pi}} \int_0^s dt e^{-t^2}. \quad (\text{A.15})$$

With the evaluation of the integrals in A.10, we find the expression for the currents associated with the an attracted species

$$I = \pi a^2 q n \left(\frac{2kT}{\pi m} \right)^{1/2} \left[e^{-x_d} + \left(1 + 2x_d - \frac{2qV}{kT} \right) \frac{\sqrt{\pi} \operatorname{erf}(x_d)}{2 x_d} \right]. \quad (\text{A.16})$$

Current from Repelled Species

For a repulsive potential, the procedure to account for the current collected by the spherical probe is similar to one done for an attractive potential. The difference is that the integration over the radial speed v is only over speed which are larger enough to overcome the potential barrier qV . Then we define

$$v_m = \sqrt{\frac{2qV}{m}} \quad (\text{A.17})$$

and

$$x_m = \sqrt{\frac{qV}{kT}} \quad (\text{A.18})$$

The collected current then is given by

$$\begin{aligned} I &= \pi a^2 q n \left(\frac{m}{2\pi kT} \right)^{3/2} \left(\frac{2kT}{m} \right)^2 \int_0^{2\pi} d\phi \int_{-1}^1 d\mu \int_{x_m}^{\infty} dx x^3 e^{-(x^2 - 2xx_d\mu + s_d^2)} \\ &\times \left(1 - \frac{qV}{kTx^2} \right) \\ I &= \pi a^2 q n \left(\frac{2kT}{\pi m} \right)^{1/2} \int_{x_m}^{\infty} dx x^2 \frac{e^{-(x-x_d)^2} - e^{-(x+x_d)^2}}{x_d} \left(1 - \frac{qV}{kTx^2} \right). \end{aligned} \quad (\text{A.19})$$

Making use of A.15 again, integrals in A.19 can be evaluated as follow

$$\int_{x_m}^{\infty} dx x^2 e^{-(x-x_d)^2} = \frac{x_d + x_m}{2} e^{-(x_d-x_m)^2} + \left(\frac{1}{2} + x_d^2\right) \frac{\sqrt{\pi}}{2} [1 + \operatorname{erf}(x_d - x_m)] \quad \text{A.20}$$

$$\int_{x_m}^{\infty} dx e^{-(x-x_d)^2} = \frac{\sqrt{\pi}}{2} [1 + \operatorname{erf}(x_d - x_m)] \quad \text{(A.21)}$$

$$\int_{x_m}^{\infty} dx x^2 e^{-(x+x_d)^2} = \frac{x_d - x_m}{2} e^{-(x_d+x_m)^2} + \left(\frac{1}{2} + x_d^2\right) \frac{\sqrt{\pi}}{2} [1 - \operatorname{erf}(x_d + x_m)] \quad \text{A.22}$$

$$\int_{x_m}^{\infty} dx e^{-(x+x_d)^2} = \frac{\sqrt{\pi}}{2} [1 + \operatorname{erf}(x_d + x_m)] \quad \text{(A.23)}$$

$$\text{(A.24)}$$

Using the results above, the current collected by the spherical probe, associated with a repelled species is then given by

$$\begin{aligned} I = & \pi a^2 q n \left(\frac{2kT}{\pi m}\right)^{1/2} \left\{ \frac{x_d + x_m}{2x_d} e^{-(x_d-x_m)^2} + \frac{x_d - x_m}{2x_d} e^{-(x_d+x_m)^2} \right. \\ & \left. + \left[\frac{1}{2} + x_d^2 - \frac{qV}{kT}\right] \frac{\sqrt{\pi} \operatorname{erf}(x_d - x_m) + \operatorname{erf}(x_d + x_m)}{2x_d} \right\} \quad \text{(A.25)} \end{aligned}$$

Net Current collected by Spherical Probe

Finally, the net current collected by a spherical Langmuir probe biased to a potential V , is the result of the ion and electron collection. If $V < 0$, then

$$\begin{aligned} I_{net} = & \pi a^2 q n \left(\frac{2kT_i}{\pi m_i}\right)^{1/2} \left[e^{-x_{id}} + \left(1 + 2x_{id} - \frac{2qV}{kT_i}\right) \frac{\sqrt{\pi} \operatorname{erf}(x_{id})}{2x_{id}} \right] \\ & - \pi a^2 q n \left(\frac{2kT_e}{\pi m_e}\right)^{1/2} \left\{ \frac{x_{ed} + x_{em}}{2x_{ed}} e^{-(x_{ed}-x_{em})^2} + \frac{x_{ed} - x_{em}}{2x_{ed}} e^{-(x_{ed}+x_{em})^2} \right. \\ & \left. + \left[\frac{1}{2} + x_{ed}^2 - \frac{qV}{kT_e}\right] \frac{\sqrt{\pi} \operatorname{erf}(x_{ed} - x_{em}) + \operatorname{erf}(x_{ed} + x_{em})}{2x_{ed}} \right\}, \quad \text{(A.26)} \end{aligned}$$

and, if $V > 0$, then

$$\begin{aligned}
I_{net} &= \pi a^2 q n \left(\frac{2kT_i}{\pi m_i} \right)^{1/2} \left\{ \frac{x_{id} + x_{im}}{2x_{id}} e^{-(x_{id}-x_{im})^2} + \frac{x_{id} - x_{im}}{2x_{id}} e^{-(x_{id}+x_{im})^2} \right. \\
&+ \left. \left[\frac{1}{2} + x_{id}^2 - \frac{qV}{kT_i} \right] \frac{\sqrt{\pi} \operatorname{erf}(x_{id} - x_{im}) + \operatorname{erf}(x_{id} + x_{im})}{2 x_{id}} \right\} \\
&- \pi a^2 q n \left(\frac{2kT_e}{\pi m_e} \right)^{1/2} \left[e^{-x_{ed}} + \left(1 + 2x_{ed} - \frac{2qV}{kT_e} \right) \frac{\sqrt{\pi} \operatorname{erf}(x_{ed})}{2 x_{ed}} \right] \quad (\text{A.27})
\end{aligned}$$

APPENDIX B

n $10^{10}m^{-3}$	T_e eV	T_i eV	m_{eff} amu	λ_D mm	V_p V	I_{sim} nA	δI_{sim} $\%$	$\epsilon_{I_{OML}}$ $\%$	$\epsilon_{I_{OML16}}$ $\%$
3.16	0.070	0.070	7.4	11.1	-3.5	5.103	0.3	2.2	34.8
3.16	0.070	0.070	7.4	11.1	-4.5	5.988	0.4	2.2	37.8
3.16	0.070	0.070	7.4	11.1	-5.5	6.886	0.3	2.4	40.1
10.00	0.070	0.068	5.9	6.2	-3.5	18.608	0.3	1.9	43.4
10.00	0.070	0.068	5.9	6.2	-4.5	22.232	0.5	2.5	47.0
10.00	0.070	0.068	5.9	6.2	-5.5	25.703	0.3	2.3	49.2
31.6	0.070	0.070	4.1	3.5	-3.5	74.462	0.4	1.4	55.2
31.6	0.070	0.070	4.1	3.5	-4.5	90.428	0.6	1.8	58.8
31.6	0.070	0.070	4.1	3.5	-5.5	106.059	0.4	1.8	61.1
63.2	0.082	0.079	13.7	2.7	-3.5	73.020	0.7	2.0	8.8
63.2	0.082	0.079	13.7	2.7	-4.5	83.467	1.1	3.2	10.7
63.2	0.082	0.079	13.7	2.7	-5.5	92.387	0.7	2.5	10.7
1.00	0.156	0.116	8.3	29.4	-3.5	1.515	0.4	3.1	30.5
1.00	0.156	0.116	8.3	29.4	-4.5	1.770	0.4	3.5	33.4
1.00	0.156	0.116	8.3	29.4	-5.5	2.032	0.2	4.2	35.8
3.16	0.140	0.113	11.4	15.7	-3.5	3.999	0.3	2.3	16.8
3.16	0.140	0.113	11.4	15.7	-4.5	4.588	0.4	2.7	18.8
3.16	0.140	0.113	11.4	15.7	-5.5	5.175	0.3	3.1	20.3
10.0	0.140	0.112	13.0	8.8	-3.5	11.902	0.4	2.4	11.5
10.0	0.140	0.112	13.0	8.8	-4.5	13.520	0.5	2.6	12.8
10.0	0.140	0.112	13.0	8.8	-5.5	15.176	0.4	3.1	14.0
31.6	0.140	0.089	15.9	5.0	-3.5	34.381	0.5	2.3	3.2
31.6	0.140	0.089	15.9	5.0	-4.5	38.595	0.7	2.6	3.4
31.6	0.140	0.089	15.9	5.0	-5.5	42.745	0.5	2.7	3.5
3.16	0.210	0.120	12.6	19.2	-3.5	3.816	0.3	2.8	12.8
3.16	0.210	0.120	12.6	19.2	-4.5	4.356	0.5	3.4	14.5
3.16	0.210	0.120	12.6	19.2	-5.5	4.883	0.3	3.6	15.6
10.0	0.220	0.107	11.3	11.0	-3.5	12.761	0.3	2.5	17.4
10.0	0.220	0.107	11.3	11.0	-4.5	14.636	0.5	2.9	19.4
10.0	0.220	0.107	11.3	11.0	-5.5	16.521	0.3	3.3	21.0
10.0	0.280	0.121	16.0	12.4	-3.5	10.727	1.1	1.1	1.9
10.0	0.280	0.121	16.0	12.4	-4.5	12.093	1.0	1.7	2.5
10.0	0.280	0.121	16.0	12.4	-5.5	13.553	0.3	3.0	3.7

Table B.1: I_{sim} are the ion currents calculated from simulations. $\epsilon_{I_{OML}}$ and $\epsilon_{I_{OML16}}$ are the relative errors in currents from simulations with respect to those predicted with OML theory, Eq. 4.1 and 4.18, respectively. δI_{sim} is the relative uncertainty in the currents from simulations. Positive errors indicate an overestimation while negative signs an underestimation.

n $10^{10}m^{-3}$	T_e eV	T_i eV	m_{eff} amu	λ_D mm	ϵ_{n_I} %	δn_I %	ϵ_n %	$\epsilon_{n_{16}}$ %	$\delta_{n-n_{16}}$ %
3.16	0.070	0.070	7.4	11.1	2.2	0.4	3.1	55.4	1.4
10.00	0.070	0.068	5.9	6.2	2.5	0.5	3.3	64.6	1.5
31.6	0.070	0.070	4.1	3.5	1.8	0.6	2.6	74.9	1.7
63.2	0.082	0.079	13.7	2.7	3.2	1.1	4.3	18.0	4.3
1.00	0.156	0.116	8.3	29.4	3.5	0.4	7.2	51.4	1.5
3.16	0.140	0.113	11.4	15.7	2.7	0.5	5.8	32.4	1.6
10.0	0.140	0.112	13.0	8.8	2.6	0.7	5.8	23.2	2.2
31.6	0.140	0.089	15.9	5.0	2.6	0.5	4.3	5.0	3.2
3.16	0.210	0.120	12.6	19.0	3.4	0.5	6.6	25.6	1.8
10.0	0.220	0.107	11.3	11.0	2.9	0.5	5.7	33.1	1.8
10.0	0.280	0.121	16.0	12.4	1.7	1.0	10.3	10.6	4.4

Table B.2: Relative errors in the inferred density calculated from probe simulations results. ϵ_{n_I} are the relative errors when Eq. 4.1 is used to infer density. ϵ_n and $\epsilon_{n_{16}}$, correspond to relative errors in inferred density when Eq. 4.6 and 4.19 are used respectively. δ_{n_I} and δ_n represent the relative uncertainties in their respective inferred densities. Positive errors indicate that the calculated density is overestimated while negative signs refer to an underestimation. In all cases, the ram velocity is 7673 m/s.

n $10^{10}m^{-3}$	T_e eV	T_i eV	m_{eff}	λ_D mm	v_{\perp} m/s	V_f^{Swarm} mV	V_f^{LP} mV	V_f^{OML} mV
3.16	0.070	0.070	7.35	11.06	7673	-201	-205	-213
10.00	0.070	0.068	5.85	6.22	7673	-195	-203	-211
31.6	0.070	0.070	4.10	3.50	7673	-194	-198	-209
63.2	0.082	0.079	13.71	2.68	7673	-223	-209	-259
1.00	0.156	0.116	8.29	29.36	7673	-513	-504	-520
3.16	0.140	0.113	11.40	15.65	7673	-454	-451	-469
10.0	0.140	0.112	12.99	8.80	7673	-443	-456	-471
31.6	0.140	0.089	15.88	4.95	7673	-437	-457	-474
3.16	0.210	0.120	12.57	19.16	7673	-719	-706	-736
10.0	0.220	0.107	11.28	11.03	7673	-752	-746	-770
10.0	0.280	0.121	15.96	12.44	7673	-990	-990	-1017

Table B.3: Floating Potentials for several configurations.

SWARM LP ION SATURATION CURRENT C01

n	T_e	T_i	m_{eff}	λ_D	v_d	
$3.16 \times 10^{10} m^{-3}$	0.070 eV	0.070 eV	7.7 amu	11.1 mm	7673 m/s	
V_f	V_p	LP_x	I_{sim}	$\epsilon_{I_{OML}}$	$\epsilon_{I_{OML16}}$	δI_{sim}
V	V		nA	%	%	%
-0.201	-2.701	LP_1	4.311	3.1	32.1	1.3
-0.201	-2.701	LP_2	4.375	4.5	33.1	1.2
-0.201	-2.701	LP_A	4.343	3.8	32.6	0.9
-0.201	-3.701	LP_1	5.229	4.1	36.7	1.0
-0.201	-3.701	LP_2	5.333	5.9	37.9	1.0
-0.201	-3.701	LP_A	5.282	5.0	37.3	0.7
-1.0	-3.5	LP_1	4.468	-8.5	27.6	1.6
-1.0	-3.5	LP_2	4.589	-5.6	29.5	1.6
-1.0	-3.5	LP_A	4.529	-7.0	28.6	1.1
-1.0	-4.5	LP_1	5.324	-6.8	32.0	1.2
-1.0	-4.5	LP_2	5.412	-5.1	32.1	1.2
-1.0	-4.5	LP_A	5.368	-5.9	32.6	0.9
-2.0	-4.5	LP_1	4.453	-27.7	18.7	1.2
-2.0	-4.5	LP_2	4.507	-26.2	19.7	1.2
-2.0	-4.5	LP_A	4.480	-26.9	19.2	0.9
-2.0	-5.5	LP_1	5.134	-27.1	22.0	1.0
-2.0	-5.5	LP_2	5.230	-24.8	23.4	1.0
-2.0	-5.5	LP_A	5.182	-25.9	22.7	0.7

Table B.4: I_{sim} are the ion currents calculated from simulations. $\epsilon_{I_{OML}}$ and $\epsilon_{I_{OML16}}$ are the relative errors in currents from simulations with respect to those predicted with OML theory, Eq. 4.1 and 4.18, respectively. δI_{sim} is the relative uncertainty in the currents from simulations. Positive errors indicate overestimation while negative signs refer to an underestimation. $\delta_{mesh} = 1.6\%$

SWARM LP ION SATURATION CURRENT C02

n	T_e	T_i	m_{eff}	λ_D	v_d	
$10.0 \times 10^{10} m^{-3}$	0.070 eV	0.068 eV	5.9 amu	6.2 mm	7673 m/s	
V_f	V_p	LP_x	I_{sim}	$\epsilon_{I_{OML}}$	$\epsilon_{I_{OML16}}$	δI_{sim}
V	V		nA	%	%	%
-0.195	-2.695	LP_1	15.658	3.9	40.9	1.6
-0.195	-2.695	LP_2	15.770	4.6	41.4	1.6
-0.195	-2.695	LP_A	15.714	4.3	41.1	1.1
-0.195	-3.695	LP_1	19.038	3.5	45.0	1.3
-0.195	-3.695	LP_2	19.439	5.5	46.1	1.3
-0.195	-3.695	LP_A	19.238	4.5	45.6	0.9
-1.0	-3.5	LP_1	17.217	-3.0	40.6	1.9
-1.0	-3.5	LP_2	17.218	-3.0	40.6	2.0
-1.0	-3.5	LP_A	17.218	-3.0	40.6	1.4
-1.0	-4.5	LP_1	20.458	-2.9	44.0	1.5
-1.0	-4.5	LP_2	20.806	-1.2	45.0	1.5
-1.0	-4.5	LP_A	20.632	-2.1	44.5	1.1
-2.0	-4.5	LP_1	18.648	-12.9	38.6	2.5
-2.0	-4.5	LP_2	18.676	-12.9	38.7	2.6
-2.0	-4.5	LP_A	18.665	-12.8	38.6	1.1
-2.0	-5.5	LP_1	21.981	-11.0	42.3	1.6
-2.0	-5.5	LP_2	22.173	-10.0	42.8	1.5
-2.0	-5.5	LP_A	22.077	-10.5	42.6	1.1

Table B.5: I_{sim} are the ion currents calculated from simulations. $\epsilon_{I_{OML}}$ and $\epsilon_{I_{OML16}}$ are the relative errors in currents from simulations with respect to those predicted with OML theory, Eq. 4.1 and 4.18, respectively. δI_{sim} is the relative uncertainty in the currents from simulations. Positive errors indicate overestimation while negative signs refer to an underestimation. $\delta_{mesh} = 1.5\%$

SWARM LP ION SATURATION CURRENT C03

n	T_e	T_i	m_{eff}	λ_D	v_d	
$31.6 \times 10^{10} m^{-3}$	0.070 eV	0.070 eV	4.1 amu	3.5 mm	7673 m/s	
V_f	V_p	LP_x	I_{sim}	$\epsilon_{I_{OML}}$	$\epsilon_{I_{OML16}}$	δI_{sim}
V	V		nA	%	%	%
-0.195	-2.695	LP_1	60.311	1.0	51.2	1.4
-0.195	-2.695	LP_2	60.605	1.4	51.4	1.3
-0.195	-2.695	LP_A	60.458	1.2	51.3	1.0
-1.0	-3.5	LP_1	69.054	-4.1	52.8	2.0
-1.0	-3.5	LP_2	67.559	-6.4	51.8	2.0
-1.0	-3.5	LP_A	68.306	-5.2	52.3	1.4
-1.0	-4.5	LP_1	82.966	-4.8	56.0	1.1
-1.0	-4.5	LP_2	83.901	-3.6	56.5	1.0
-1.0	-4.5	LP_A	83.434	-4.2	56.3	0.7
-2.0	-4.5	LP_1	76.356	-13.9	52.2	1.4
-2.0	-4.5	LP_2	77.879	-11.6	53.2	1.4
-2.0	-4.5	LP_A	77.118	-12.7	52.7	1.0
-2.0	-5.5	LP_1	90.890	-12.2	55.6	1.1
-2.0	-5.5	LP_2	92.448	-10.3	56.3	1.1
-2.0	-5.5	LP_A	91.669	-11.3	56.0	0.8

Table B.6: I_{sim} are the ion currents calculated from simulations. $\epsilon_{I_{OML}}$ and $\epsilon_{I_{OML16}}$ are the relative errors in currents from simulations with respect to those predicted with OML theory, Eq. 4.1 and 4.18, respectively. δI_{sim} is the relative uncertainty in the currents from simulations. Positive errors indicate overestimation while negative signs refer to an underestimation. $\delta_{mesh} = 1.1\%$

SWARM LP ION SATURATION CURRENT C04

n	T_e	T_i	m_{eff}	λ_D	v_d	
$63.2 \times 10^{10} m^{-3}$	0.082 eV	0.079 eV	13.7 amu	2.7 mm	7673 m/s	
V_f	V_p	LP_x	I_{sim}	$\epsilon_{I_{OML}}$	$\epsilon_{I_{OML16}}$	δI_{sim}
V	V		nA	%	%	%
-0.223	-2.723	LP_1	64.079	1.6	7.7	1.9
-0.223	-2.723	LP_2	66.806	5.7	11.5	1.9
-0.223	-2.723	LP_A	65.443	3.7	9.6	1.3
-1.0	-3.5	LP_1	69.716	-0.5	6.5	2.1
-1.0	-3.5	LP_2	71.276	1.7	8.5	2.1
-1.0	-3.5	LP_A	70.496	0.6	7.5	1.5
-1.0	-4.5	LP_1	82.321	3.9	11.4	1.8
-1.0	-4.5	LP_2	80.172	1.3	9.0	1.8
-1.0	-4.5	LP_A	81.246	2.6	10.2	1.3
-2.0	-4.5	LP_1	76.197	-3.9	4.2	2.3
-2.0	-4.5	LP_2	79.652	0.6	8.4	2.2
-2.0	-4.5	LP_A	77.925	-1.6	6.4	1.6
-2.0	-5.5	LP_1	88.760	0.6	9.0	1.9
-2.0	-5.5	LP_2	87.962	-1.4	7.1	1.9
-2.0	-5.5	LP_A	87.861	-0.4	8.1	1.3

Table B.7: I_{sim} are the ion currents calculated from simulations. $\epsilon_{I_{OML}}$ and $\epsilon_{I_{OML16}}$ are the relative errors in currents from simulations with respect to those predicted with OML theory, Eq. 4.1 and 4.18, respectively. δI_{sim} is the relative uncertainty in the currents from simulations. Positive errors indicate overestimation while negative signs refer to an underestimation. $\delta_{mesh} = 3.0\%$

SWARM LP ION SATURATION CURRENT C05

n	T_e	T_i	m_{eff}	λ_D	v_d	
$10^{10} m^{-3}$	0.156 eV	0.116 eV	8.3 amu	29.4 mm	7673 m/s	
V_f	V_p	LP_x	I_{sim}	$\epsilon_{I_{OML}}$	$\epsilon_{I_{OML16}}$	δI_{sim}
V	V		nA	%	%	%
-0.513	-3.013	LP_1	1.217	-7.8	20.8	1.3
-0.513	-3.013	LP_2	1.222	-7.4	21.1	1.3
-0.513	-3.013	LP_A	1.220	-7.6	21.0	0.9
-0.513	-4.013	LP_1	1.448	-6.7	25.0	1.1
-0.513	-4.013	LP_2	1.443	-7.1	24.8	1.1
-0.513	-4.013	LP_A	1.446	-6.9	24.9	0.7
-1.0	-3.5	LP_1	1.191	-19.6	14.1	1.4
-1.0	-3.5	LP_2	1.211	-17.7	15.5	1.4
-1.0	-3.5	LP_A	1.201	-18.7	14.8	1.0
-1.0	-4.5	LP_1	1.392	-19.2	17.7	1.1
-1.0	-4.5	LP_2	1.399	-18.5	18.2	1.0
-1.0	-4.5	LP_A	1.396	-18.8	17.9	0.7
-2.0	-4.5	LP_1	1.136	-46.0	-0.8	1.7
-2.0	-4.5	LP_2	1.153	-43.9	0.6	1.7
-2.0	-4.5	LP_A	1.145	-44.9	0.0	1.2
-2.0	-5.5	LP_1	1.300	-45.5	2.5	1.1
-2.0	-5.5	LP_2	1.328	-42.4	4.6	1.1
-2.0	-5.5	LP_A	1.314	-44.0	3.6	0.8

Table B.8: I_{sim} are the ion currents calculated from simulations. $\epsilon_{I_{OML}}$ and $\epsilon_{I_{OML16}}$ are the relative errors in currents from simulations with respect to those predicted with OML theory, Eq. 4.1 and 4.18, respectively. δI_{sim} is the relative uncertainty in the currents from simulations. Positive errors indicate overestimation while negative signs refer to an underestimation. $\delta_{mesh} = 0.7\%$

SWARM LP ION SATURATION CURRENT C06

n	T_e	T_i	m_{eff}	λ_D	v_d	
$3.16 \times 10^{10} m^{-3}$	0.140 eV	0.113 eV	11.4 amu	15.7 mm	7673 m/s	
V_f	V_p	LP_x	I_{sim}	$\epsilon_{I_{OML}}$	$\epsilon_{I_{OML16}}$	δI_{sim}
V	V		nA	%	%	%
-0.454	-2.954	LP_1	3.497	-0.2	13.6	1.5
-0.454	-2.954	LP_2	3.545	1.2	14.7	1.5
-0.454	-2.954	LP_A	3.521	0.5	14.2	1.1
-1.0	-3.5	LP_1	3.647	-4.1	11.3	1.5
-1.0	-3.5	LP_2	3.680	-3.2	12.1	1.5
-1.0	-3.5	LP_A	3.663	-3.6	11.7	1.1
-1.0	-4.5	LP_1	4.187	-3.5	13.6	1.2
-1.0	-4.5	LP_2	4.256	-1.8	15.0	1.1
-1.0	-4.5	LP_A	4.222	-2.7	14.3	0.8
-2.0	-4.5	LP_1	3.771	-15.0	4.0	1.9
-2.0	-4.5	LP_2	3.809	-13.8	5.0	1.9
-2.0	-4.5	LP_A	3.790	-14.4	4.5	1.36
-2.0	-5.5	LP_1	4.245	-14.8	5.6	1.2
-2.0	-5.5	LP_2	4.304	-13.2	7.0	1.2
-2.0	-5.5	LP_A	4.275	-14.0	6.3	0.8

Table B.9: I_{sim} are the ion currents calculated from simulations. $\epsilon_{I_{OML}}$ and $\epsilon_{I_{OML16}}$ are the relative errors in currents from simulations with respect to those predicted with OML theory, Eq. 4.1 and 4.18, respectively. δI_{sim} is the relative uncertainty in the currents from simulations. Positive errors indicate overestimation while negative signs refer to an underestimation. $\delta_{mesh} = 1.3\%$

SWARM LP ION SATURATION CURRENT C07

n	T_e	T_i	m_{eff}	λ_D	v_d	
$10.0 \times 10^{10} m^{-3}$	0.140 eV	0.112 eV	13.0 amu	8.8 mm	7673 m/s	
V_f	V_p	LP_x	I_{sim}	$\epsilon_{I_{OML}}$	$\epsilon_{I_{OML16}}$	δI_{sim}
V	V		nA	%	%	%
-0.443	-2.943	LP_1	10.730	2.6	11.0	1.3
-0.443	-2.943	LP_2	10.902	4.2	12.4	1.3
-0.443	-2.943	LP_A	10.816	3.4	11.7	0.9
-1.0	-3.5	LP_1	11.106	-1.6	7.9	2.0
-1.0	-3.5	LP_2	11.518	2.0	11.2	2.0
-1.0	-3.5	LP_A	11.312	0.2	9.5	1.4
-1.0	-4.5	LP_1	12.949	1.3	11.6	1.5
-1.0	-4.5	LP_2	13.3	3.8	13.8	1.4
-1.0	-4.5	LP_A	13.116	2.5	12.7	1.0
-2.0	-4.5	LP_1	12.383	-3.2	7.5	2.2
-2.0	-4.5	LP_2	12.365	-3.4	7.4	2.2
-2.0	-4.5	LP_A	12.374	-3.3	7.4	1.5
-2.0	-5.5	LP_1	13.972	-2.2	9.3	1.4
-2.0	-5.5	LP_2	14.120	-1.1	10.2	1.3
-2.0	-5.5	LP_A	14.046	-1.7	9.8	1.0

Table B.10: I_{sim} are the ion currents calculated from simulations. $\epsilon_{I_{OML}}$ and $\epsilon_{I_{OML16}}$ are the relative errors in currents from simulations with respect to those predicted with OML theory, Eq. 4.1 and 4.18, respectively. δI_{sim} is the relative uncertainty in the currents from simulations. Positive errors indicate overestimation while negative signs refer to an underestimation. $\delta_{mesh} = 2.2\%$

SWARM LP ION SATURATION CURRENT C08

n	T_e	T_i	m_{eff}	λ_D	v_d	
$31.6 \times 10^{10} m^{-3}$	0.140 eV	0.089 eV	15.9 amu	5.0 mm	7673 m/s	
V_f	V_p	LP_x	I_{sim}	$\epsilon_{I_{OML}}$	$\epsilon_{I_{OML16}}$	δI_{sim}
V	V		nA	%	%	%
-0.437	-2.937	LP_1	31.629	3.0	3.9	1.5
-0.437	-2.937	LP_2	31.534	2.7	3.6	1.6
-0.437	-2.937	LP_A	31.581	2.9	3.7	1.1
-1.0	-3.5	LP_1	33.473	1.8	2.6	1.7
-1.0	-3.5	LP_2	33.097	0.7	1.5	1.6
-1.0	-3.5	LP_A	33.285	1.2	2.1	1.2
-1.0	-4.5	LP_1	37.917	3.0	3.8	1.7
-1.0	-4.5	LP_2	37.744	2.5	3.3	1.7
-1.0	-4.5	LP_A	37.830	2.7	3.5	1.2
-2.0	-4.5	LP_1	36.316	-1.3	-0.5	1.8
-2.0	-4.5	LP_2	36.057	-2.0	-1.2	1.8
-2.0	-4.5	LP_A	36.187	-1.7	-0.8	1.3
-2.0	-5.5	LP_1	41.0442	0.8	1.6	1.4
-2.0	-5.5	LP_2	40.900	0.5	1.3	1.4
-2.0	-5.5	LP_A	40.972	0.6	1.5	1.0

Table B.11: I_{sim} are the ion currents calculated from simulations. $\epsilon_{I_{OML}}$ and $\epsilon_{I_{OML16}}$ are the relative errors in currents from simulations with respect to those predicted with OML theory, Eq. 4.1 and 4.18, respectively. δI_{sim} is the relative uncertainty in the currents from simulations. Positive errors indicate overestimation while negative signs refer to an underestimation. $\delta_{mesh} = 1.1\%$

SWARM LP ION SATURATION CURRENT C09

n	T_e	T_i	m_{eff}	λ_D	v_d	
$3.16 \times 10^{10} m^{-3}$	0.210 eV	0.120 eV	12.6 amu	19.2 mm	7673 m/s	
V_f	V_p	LP_x	I_{sim}	$\epsilon_{I_{OML}}$	$\epsilon_{I_{OML16}}$	δI_{sim}
V	V		nA	%	%	%
-0.719	-3.219	LP_1	3.481	0.4	10.2	1.5
-0.719	-3.219	LP_2	3.466	0.0	9.8	1.5
-0.719	-3.219	LP_A	3.474	0.2	10.0	1.0
-1.0	-3.5	LP_1	3.514	-2.5	8.0	1.5
-1.0	-3.5	LP_2	3.522	-2.3	8.2	1.5
-1.0	-3.5	LP_A	3.518	-2.4	8.1	1.0
-1.0	-4.5	LP_1	4.059	-0.7	10.8	1.1
-1.0	-4.5	LP_2	4.002	-2.2	9.6	1.2
-1.0	-4.5	LP_A	4.031	-1.4	10.2	0.8
-2.0	-4.5	LP_1	3.621	-12.8	0.1	1.8
-2.0	-4.5	LP_2	3.624	-12.8	0.1	1.8
-2.0	-4.5	LP_A	3.623	-12.8	0.1	1.2
-2.0	-5.5	LP_1	4.067	-12.4	1.5	1.2
-2.0	-5.5	LP_2	4.100	-11.5	2.3	1.2
-2.0	-5.5	LP_A	4.084	-11.9	1.9	0.9

Table B.12: I_{sim} are the ion currents calculated from simulations. $\epsilon_{I_{OML}}$ and $\epsilon_{I_{OML16}}$ are the relative errors in currents from simulations with respect to those predicted with OML theory, Eq. 4.1 and 4.18, respectively. δI_{sim} is the relative uncertainty in the currents from simulations. Positive errors indicate overestimation while negative signs refer to an underestimation. $\delta_{mesh} = 1.2\%$

SWARM LP ION SATURATION CURRENT C10

n	T_e	T_i	m_{eff}	λ_D	v_d	
$10.0 \times 10^{10} m^{-3}$	0.220 eV	0.107 eV	11.3 amu	11.0 mm	7673 m/s	
V_f	V_p	LP_x	I_{sim}	$\epsilon_{I_{OML}}$	$\epsilon_{I_{OML16}}$	δI_{sim}
V	V		nA	%	%	%
-0.752	-3.252	LP_1	11.689	0.3	15.1	1.1
-0.752	-3.252	LP_2	11.884	2.0	16.5	1.1
-0.752	-3.252	LP_A	11.787	1.1	15.8	0.8
-1.0	-3.5	LP_1	12.012	-0.6	14.8	1.7
-1.0	-3.5	LP_2	11.977	-0.8	14.6	1.7
-1.0	-3.5	LP_A	11.995	-0.7	14.7	1.2
-1.0	-4.5	LP_1	13.768	-0.2	16.8	1.2
-1.0	-4.5	LP_2	13.754	-0.3	16.7	1.2
-1.0	-4.5	LP_A	13.761	-0.3	16.8	0.8
-2.0	-4.5	LP_1	13.043	-5.8	12.2	2.1
-2.0	-4.5	LP_2	13.125	-5.2	12.7	2.1
-2.0	-4.5	LP_A	13.084	-5.5	12.5	1.5
-2.0	-5.5	LP_1	14.753	-5.2	14.1	1.4
-2.0	-5.5	LP_2	14.761	-5.2	14.1	1.4
-2.0	-5.5	LP_A	14.757	-5.2	14.1	1.0

Table B.13: I_{sim} are the ion currents calculated from simulations. $\epsilon_{I_{OML}}$ and $\epsilon_{I_{OML16}}$ are the relative errors in currents from simulations with respect to those predicted with OML theory, Eq. 4.1 and 4.18, respectively. δI_{sim} is the relative uncertainty in the currents from simulations. Positive errors indicate overestimation while negative signs refer to an underestimation. $\delta_{mesh} = 1.0\%$

SWARM LP ION SATURATION CURRENT C11

n	T_e	T_i	m_{eff}	λ_D	v_d	
$10.0 \times 10^{10} m^{-3}$	0.280 eV	0.121 eV	16.0 amu	12.4 mm	7673 m/s	
V_f	V_p	LP_x	I_{sim}	$\epsilon_{I_{OML}}$	$\epsilon_{I_{OML16}}$	δI_{sim}
V	V		nA	%	%	%
-0.990	-3.490	LP_1	10.583	2.5	3.4	1.3
-0.990	-3.490	LP_2	10.607	2.7	3.7	1.3
-0.990	-3.490	LP_A	10.595	2.6	3.5	0.9
-1.0	-3.5	LP_1	10.616	2.7	3.6	1.8
-1.0	-3.5	LP_2	10.402	0.7	1.6	1.8
-1.0	-3.5	LP_A	10.509	1.7	2.6	1.3
-1.0	-4.5	LP_1	11.948	3.2	4.1	1.3
-1.0	-4.5	LP_2	12.001	3.7	4.6	1.3
-1.0	-4.5	LP_A	11.974	3.4	4.4	0.9
-2.0	-4.5	LP_1	11.482	-0.7	0.3	2.2
-2.0	-4.5	LP_2	11.723	1.4	2.3	2.2
-2.0	-4.5	LP_A	11.603	0.4	1.3	1.6
-2.0	-5.5	LP_1	12.723	-0.5	0.4	1.6
-2.0	-5.5	LP_2	12.787	0.0	0.9	1.6
-2.0	-5.5	LP_A	12.755	-0.3	0.6	1.1

Table B.14: I_{sim} are the ion currents calculated from simulations. $\epsilon_{I_{OML}}$ and $\epsilon_{I_{OML16}}$ are the relative errors in currents from simulations with respect to those predicted with OML theory, Eq. 4.1 and 4.18, respectively. δI_{sim} is the relative uncertainty in the currents from simulations. Positive errors indicate overestimation while negative signs refer to an underestimation. $\delta_{mesh} = 2.0\%$

SWARM LP ION SATURATION CURRENT C12

n	T_e	T_i	m_{eff}	λ_D	v_d	
$3.16 \times 10^{10} m^{-3}$	0.070 eV	0.070 eV	7.4.0 amu	11.1 mm	8173 m/s	
V_f	V_p	LP_x	I_{sim}	$\epsilon_{I_{OML}}$	$\epsilon_{I_{OML16}}$	δI_{sim}
V	V		nA	%	%	%
-1.0	-4.5	LP_1	5.182	-7.7	29.8	2.2
-1.0	-4.5	LP_2	5.424	-2.9	33.0	2.1
-1.0	-4.5	LP_A	5.303	-5.2	31.4	1.5
-2.0	-5.5	LP_1	5.105	-24.7	21.7	2.1
-2.0	-5.5	LP_2	5.278	-20.6	24.3	2.2
-2.0	-5.5	LP_A	5.192	-22.7	23.0	1.5

Table B.15: I_{sim} are the ion currents calculated from simulations. $\epsilon_{I_{OML}}$ and $\epsilon_{I_{OML16}}$ are the relative errors in currents from simulations with respect to those predicted with OML theory, Eq. 4.1 and 4.18, respectively. δI_{sim} is the relative uncertainty in the currents from simulations. Positive errors indicate overestimation while negative signs refer to an underestimation. $\delta_{mesh} = 3.9\%$

SWARM LP ION SATURATION CURRENT C13

n	T_e	T_i	m_{eff}	λ_D	v_d	
$10.0 \times 10^{10} m^{-3}$	0.070 eV	0.068 eV	5.9 amu	6.2 mm	8173 m/s	
V_f	V_p	LP_x	I_{sim}	$\epsilon_{I_{OML}}$	$\epsilon_{I_{OML16}}$	δI_{sim}
V	V		nA	%	%	%
-1.0	-4.5	LP_1	20.403	-0.7	43.6	2.6
-1.0	-4.5	LP_2	20.457	-0.4	43.8	2.6
-1.0	-4.5	LP_A	20.430	-0.5	43.7	1.9
-1.0	-5.5	LP_1	21.680	-9.2	41.6	2.6
-1.0	-5.5	LP_2	21.985	-7.6	42.5	2.6
-1.0	-5.5	LP_A	21.832	-8.4	42.1	1.8

Table B.16: I_{sim} are the ion currents calculated from simulations. $\epsilon_{I_{OML}}$ and $\epsilon_{I_{OML16}}$ are the relative errors in currents from simulations with respect to those predicted with OML theory, Eq. 4.1 and 4.18, respectively. δI_{sim} is the relative uncertainty in the currents from simulations. Positive errors indicate overestimation while negative signs refer to an underestimation. $\delta_{mesh} = 0.8\%$

SWARM LP ION SATURATION CURRENT C14

n	T_e	T_i	m_{eff}	λ_D	v_d	
$10^{10} m^{-3}$	0.156 eV	0.116 eV	8.3 amu	29.4 mm	8173 m/s	
V_f	V_p	LP_x	I_{sim}	ϵ_{IOML}	ϵ_{IOML16}	δI_{sim}
V	V		nA	%	%	%
-1.0	-4.5	LP_1	1.389	-17.8	17.2	1.7
-1.0	-4.5	LP_2	1.399	-18.0	17.8	1.8
-1.0	-4.5	LP_A	1.394	-17.4	17.5	1.2
-2.0	-5.5	LP_1	1.318	-40.8	4.0	2.9
-2.0	-5.5	LP_2	1.309	-41.7	3.4	3.0
-2.0	-5.5	LP_A	1.314	-41.3	3.7	2.1

Table B.17: I_{sim} are the ion currents calculated from simulations. ϵ_{IOML} and ϵ_{IOML16} are the relative errors in currents from simulations with respect to those predicted with OML theory, Eq. 4.1 and 4.18, respectively. δI_{sim} is the relative uncertainty in the currents from simulations. Positive errors indicate overestimation while negative signs refer to an underestimation. $\delta_{mesh} = 1.0\%$

SWARM LP ION SATURATION CURRENT C15

n	T_e	T_i	m_{eff}	λ_D	v_d	
$10.0 \times 10^{10} m^{-3}$	0.280 eV	0.121 eV	16.0 amu	12.4 mm	8173 m/s	
V_f	V_p	LP_x	I_{sim}	ϵ_{IOML}	ϵ_{IOML16}	δI_{sim}
V	V		nA	%	%	%
-1.0	-4.5	LP_1	12.167	4.8	5.4	3.2
-1.0	-4.5	LP_2	11.810	1.9	2.6	3.2
-1.0	-4.5	LP_A	11.989	3.3	4.0	2.3
-2.0	-5.5	LP_1	12.725	-0.1	0.6	2.1
-2.0	-5.5	LP_2	12.794	0.4	1.1	2.1
-2.0	-5.5	LP_A	12.759	0.2	0.8	1.5

Table B.18: I_{sim} are the ion currents calculated from simulations. ϵ_{IOML} and ϵ_{IOML16} are the relative errors in currents from simulations with respect to those predicted with OML theory, Eq. 4.1 and 4.18, respectively. δI_{sim} is the relative uncertainty in the currents from simulations. Positive errors indicate overestimation while negative signs refer to an underestimation. $\delta_{mesh} = 1.3\%$

SWARM LP ION SATURATION CURRENT C16

n	T_e	T_i	m_{eff}	λ_D	v_d	
$3.16 \times 10^{10} m^{-3}$	0.070 eV	0.070 eV	7.4 amu	11.1 mm	7173 m/s	
V_f	V_p	LP_x	I_{sim}	ϵ_{IOML}	ϵ_{IOML16}	δI_{sim}
V	V		nA	%	%	%
-1.0	-4.5	LP_1	5.366	-8.5	32.6	1.8
-1.0	-4.5	LP_2	5.360	-8.6	32.5	1.8
-1.0	-4.5	LP_A	5.363	-8.6	32.5	1.3
-2.0	-5.5	LP_1	5.193	-29.4	22.4	2.2
-2.0	-5.5	LP_2	5.167	-30.8	22.0	2.2
-2.0	-5.5	LP_A	5.180	-29.7	22.2	1.6

Table B.19: I_{sim} are the ion currents calculated from simulations. ϵ_{IOML} and ϵ_{IOML16} are the relative errors in currents from simulations with respect to those predicted with OML theory, Eq. 4.1 and 4.18, respectively. δI_{sim} is the relative uncertainty in the currents from simulations. Positive errors indicate overestimation while negative signs refer to an underestimation. $\delta_{mesh} = 0.3\%$

SWARM LP ION SATURATION CURRENT C17

n	T_e	T_i	m_{eff}	λ_D	v_d	
$10.0 \times 10^{10} m^{-3}$	0.070 eV	0.068 eV	5.9 amu	6.2 mm	7173 m/s	
V_f	V_p	LP_x	I_{sim}	ϵ_{IOML}	ϵ_{IOML16}	δI_{sim}
V	V		nA	%	%	%
-1.0	-4.5	LP_1	21.069	-3.0	45.7	2.6
-1.0	-4.5	LP_2	21.591	-0.5	47.0	2.6
-1.0	-4.5	LP_A	21.330	-1.7	46.3	1.8
-2.0	-5.5	LP_1	22.216	-13.7	42.6	2.4
-2.0	-5.5	LP_2	22.428	-12.6	43.1	2.4
-2.0	-5.5	LP_A	22.322	-13.1	42.9	1.7

Table B.20: I_{sim} are the ion currents calculated from simulations. ϵ_{IOML} and ϵ_{IOML16} are the relative errors in currents from simulations with respect to those predicted with OML theory, Eq. 4.1 and 4.18, respectively. δI_{sim} is the relative uncertainty in the currents from simulations. Positive errors indicate overestimation while negative signs refer to an underestimation. $\delta_{mesh} = 1.7\%$

SWARM LP ION SATURATION CURRENT C18

n	T_e	T_i	m_{eff}	λ_D	v_d	
$10^{10} m^{-3}$	0.156 eV	0.116 eV	8.3 amu	29.4 mm	7173 m/s	
V_f	V_p	LP_x	I_{sim}	$\epsilon_{I_{OML}}$	$\epsilon_{I_{OML16}}$	δI_{sim}
V	V		nA	%	%	%
-1.0	-4.5	LP_1	1.401	-20.5	18.3	1.6
-1.0	-4.5	LP_2	1.410	-19.7	18.8	1.6
-1.0	-4.5	LP_A	1.405	-20.1	18.5	1.1
-2.0	-5.5	LP_1	1.303	-48.6	2.1	2.0
-2.0	-5.5	LP_2	1.322	-46.4	3.5	2.0
-2.0	-5.5	LP_A	1.313	-48.5	2.9	1.4

Table B.21: I_{sim} are the ion currents calculated from simulations. $\epsilon_{I_{OML}}$ and $\epsilon_{I_{OML16}}$ are the relative errors in currents from simulations with respect to those predicted with OML theory, Eq. 4.1 and 4.18, respectively. δI_{sim} is the relative uncertainty in the currents from simulations. Positive errors indicate overestimation while negative signs refer to an underestimation. $\delta_{mesh} = 1.1\%$

SWARM LP ION SATURATION CURRENT C19

n	T_e	T_i	m_{eff}	λ_D	v_d	
$10.0 \times 10^{10} m^{-3}$	0.280 eV	0.121 eV	16.0 amu	12.4 mm	7173 m/s	
V_f	V_p	LP_x	I_{sim}	$\epsilon_{I_{OML}}$	$\epsilon_{I_{OML16}}$	δI_{sim}
V	V		nA	%	%	%
-1.0	-4.5	LP_1	11.850	2.6	3.4	2.4
-1.0	-4.5	LP_2	12.114	4.7	5.5	2.5
-1.0	-4.5	LP_A	11.982	3.7	4.5	1.7
-2.0	-5.5	LP_1	12.573	-2.2	-1.4	2.5
-2.0	-5.5	LP_1	12.907	0.4	1.2	2.5
-2.0	-5.5	LP_1	12.740	-0.9	-0.1	1.7

Table B.22: I_{sim} are the ion currents calculated from simulations. $\epsilon_{I_{OML}}$ and $\epsilon_{I_{OML16}}$ are the relative errors in currents from simulations with respect to those predicted with OML theory, Eq. 4.1 and 4.18, respectively. δI_{sim} is the relative uncertainty in the currents from simulations. Positive errors indicate overestimation while negative signs refer to an underestimation. $\delta_{mesh} = 2.4\%$

INFERRED PLASMA DENSITY FROM SWARM LP

n $10^{10}m^{-3}$	Te eV	Ti eV	m_{eff} amu	λ_D mm	V_f V	LP_x	ϵ_{n_I} %	δ_{n_I} %	ϵ_n %	$\epsilon_{n_{16}}$ %	δ_n %
3.16	0.070	0.070	7.4	11.1	-0.201	LP_1	3.1	1.8	8.7	58.0	8.3
					-0.201	LP_2	4.5	1.8	12.5	59.7	8.0
					-0.201	LP_A	3.8	1.2	10.6	58.9	5.7
					-1.0	LP_1	-8.5	2.2	2.0	54.9	11.4
					-1.0	LP_2	-5.6	2.1	-2.0	53.1	12.0
					-1.0	LP_A	-7.0	1.5	0.0	54.0	8.3
					-2.0	LP_1	-27.7	1.6	-23.0	43.4	10.7
					-2.0	LP_2	-26.2	1.6	-16.0	46.6	10.2
					-2.0	LP_A	-26.9	1.2	-19.4	45.1	7.4
10.00	0.070	0.068	5.9	6.2	-0.195	LP_1	3.9	2.2	1.5	63.9	10.3
					-0.195	LP_2	4.6	2.2	9.2	66.7	9.7
					-0.195	LP_A	4.2	1.6	5.5	65.4	7.0
					-1.0	LP_1	-3.0	2.7	-2.8	62.3	14.2
					-1.0	LP_2	-3.0	2.7	7.2	66.0	12.9
					-1.0	LP_A	-3.0	1.9	2.5	64.2	9.6
					-2.0	LP_1	-12.9	3.1	0.1	63.4	17.6
					-2.0	LP_2	-12.8	3.1	4.8	65.1	16.8
					-2.0	LP_A	-12.8	2.2	2.5	64.2	12.2
31.6	0.070	0.070	4.1	3.5	-1.0	LP_1	-4.1	2.4	-8.3	72.0	11.9
					-1.0	LP_2	-6.4	2.4	7.8	76.2	9.9
					-1.0	LP_A	-5.2	1.7	-0.4	74.3	7.6
					-2.0	LP_1	-13.9	1.9	-3.6	73.2	10.1
					-2.0	LP_2	-11.6	1.9	-3.4	73.3	10.3
					-2.0	LP_A	-12.7	1.4	-3.5	73.3	7.2
63.2	0.082	0.079	13.7	2.7	-1.0	LP_1	-0.5	3.0	28.0	38.3	16.5
					-1.0	LP_2	1.7	2.9	-2.0	12.6	23.3
					-1.0	LP_A	0.6	2.1	15.6	27.6	13.6
					-2.0	LP_1	-3.8	3.1	27.8	38.1	19.0
					-2.0	LP_2	0.6	3.0	-24.1	-6.4	32.4
					-2.0	LP_A	-1.5	2.2	8.7	21.7	16.9

n $10^{10}m^{-3}$	Te eV	Ti eV	m_{eff} amu	λ_D mm	V_f V	LP_x	ϵ_{nI} %	δ_{nI} %	ϵ_n %	ϵ_{n16} %	δ_n %
1.00	0.156	0.116	8.3	29.4	-0.513	LP_1	-7.8	1.8	-1.1	47.1	9.7
					-0.513	LP_2	-7.4	1.8	-5.3	44.9	10.0
					-0.513	LP_A	-7.6	1.3	-3.1	46.0	7.0
					-1.0	LP_1	-19.6	1.9	-16.4	39.0	11.1
					-1.0	LP_2	-17.7	1.8	-23.3	35.4	11.8
					-1.0	LP_A	-17.7	1.3	-19.8	37.3	8.1
					-2.0	LP_1	-46.0	2.1	-42.5	25.4	14.8
					-2.0	LP_2	-43.9	2.1	-32.7	30.5	14.0
					-2.0	LP_A	-44.9	1.5	-37.5	28.0	10.2
3.16	0.140	0.113	11.4	15.7	-1.0	LP_1	-4.1	2.0	0.5	28.7	13.6
					-1.0	LP_2	-3.2	2.0	6.7	33.1	12.8
					-1.0	LP_A	-3.6	1.4	3.7	30.9	9.3
					-2.0	LP_1	-15.0	2.3	-13.5	18.6	18.6
					-2.0	LP_2	-13.8	2.4	-8.7	22.1	18.1
					-2.0	LP_A	-14.4	1.7	-11.1	20.4	13.0
10.0	0.140	0.112	13.0	8.8	-1.0	LP_1	-1.6	2.6	18.7	33.8	15.8
					-1.0	LP_2	2.0	2.6	15.2	30.9	16.8
					-1.0	LP_A	0.2	1.8	17.0	32.4	11.5
					-2.0	LP_1	-3.2	2.7	5.7	23.2	20.7
					-2.0	LP_2	-3.4	2.7	14.7	30.4	18.7
					-2.0	LP_A	-3.3	1.9	10.4	27.0	13.9

n $10^{10}m^{-3}$	Te eV	Ti eV	m_{eff} amu	λ_D mm	V_f V	LP_x	ϵ_{n_I} %	δ_{n_I} %	ϵ_n %	ϵ_{n16} %	δ_n %
31.6	0.140	0.089	15.9	5.0	-1.0	LP_1	1.8	2.6	11.8	12.5	19.2
					-1.0	LP_2	0.7	2.6	15.7	16.3	18.3
					-1.0	LP_A	1.2	1.8	13.8	14.4	13.2
					-2.0	LP_1	-1.3	2.4	17.1	17.8	18.8
					-2.0	LP_2	-2.0	2.4	19.1	19.7	18.1
					-2.0	LP_A	-1.7	1.7	18.1	18.7	13.0
3.16	0.210	0.120	12.6	19.2	-1.0	LP_1	-2.5	2.0	11.2	29.2	12.6
					-1.0	LP_2	-2.3	2.0	-1.0	19.6	14.4
					-1.0	LP_A	-2.4	1.4	5.5	24.7	9.5
					-2.0	LP_1	-12.8	2.2	-8.6	13.5	18.2
					-2.0	LP_2	-12.8	2.2	-1.6	19.1	16.9
					-2.0	LP_A	-12.8	1.6	-5.0	16.4	12.4
10.0	0.220	0.107	11.3	11.0	-1.0	LP_1	-0.6	2.2	1.9	30.5	15.0
					-1.0	LP_2	-0.8	2.2	3.0	31.3	14.8
					-1.0	LP_A	-0.7	1.6	2.5	30.9	10.5
					-2.0	LP_1	-5.8	2.7	-0.7	28.6	20.2
					-2.0	LP_2	-5.2	2.6	-5.3	25.4	21.3
					-2.0	LP_A	-5.5	1.9	-2.9	27.0	14.7
10.0	0.280	0.121	16.0	12.4	-1.0	LP_1	2.8	2.3	8.0	8.3	18.5
					-1.0	LP_2	0.8	2.4	23.4	23.6	15.4
					-1.0	LP_A	1.8	1.7	16.4	16.7	11.9
					-2.0	LP_1	-0.5	2.8	1.4	1.6	25.7
					-2.0	LP_2	1.5	2.8	-15.0	-14.7	30.9
					-2.0	LP_A	0.5	2.0	-6.2	-5.9	19.9

Table B.23: Relative errors in the inferred density calculated from probe simulations results. ϵ_{n_I} is the relative error when Eq. 4.1 is used to infer density. ϵ_n and ϵ_{n16} , correspond to relative error in inferred density when Eq. 4.6 and 4.19 are used respectively. δ_{n_I} and δ_n represents the relative uncertainties in their respective inferred densities. Positive errors indicate that calculated density is overestimated while negative signs refer to an underestimation. In all cases, ram velocity is 7673 m/s.

ELECTRON LINEAR AND RETARDATION CURRENTS C05

n	Te	T_i	m_{eff}	λ_D	v_d		
$10^{10} m^{-3}$	0.156 eV	0.116 eV	8.3	29.4 mm	7673 m/s		
LP_x	Swarm Bus Included	$ \vec{B} $ μT	V_p V	I_p nA	ϵ_{I_p} %	δ_{I_p} %	
LP1	No	0	0.196	-45.267	1.2	0.1	
LP1	No	0	0.496	-86.456	1.4	0.1	
LP1	No	0	-0.168	-6.044	4.3	0.3	
LP1	No	0	-0.138	-7.498	4.5	0.3	
LP1	No	0	-0.109	-9.214	4.9	0.2	
LP1	No	37.6	0.197	-40.871	-9.4	0.1	
LP1	No	37.6	0.497	-71.750	-18.9	0.1	
LP1	No	37.6	-0.236	-3.615	4.2	0.4	
LP1	No	37.6	-0.207	-4.508	4.2	0.3	
LP1	No	37.6	-0.178	-5.597	4.5	0.3	
LP1	Yes	0	0.186	-36.179	-20.4	0.4	
LP2	Yes	0	0.186	-35.535	-22.6	0.4	
LPA	Yes	0	0.186	-35.857	-21.5	0.4	
LP1	Yes	0	0.485	-72.408	-14.5	0.3	
LP2	Yes	0	0.485	-73.237	-13.2	0.3	
LPA	Yes	0	0.485	-72.822	-13.9	0.3	
LP1	Yes	0	-0.136	-6.872	-10.4	0.8	
LP2	Yes	0	-0.136	-6.965	-9.0	0.8	
LPA	Yes	0	-0.136	-6.918	-9.7	0.8	
LP1	Yes	0	-0.107	-8.577	-8.2	0.7	
LP2	Yes	0	-0.107	-8.498	-9.2	0.7	
LPA	Yes	0	-0.107	-8.537	-8.7	0.7	
LP1	Yes	0	-0.078	-10.332	-9.4	0.6	
LP2	Yes	0	-0.078	-10.379	-8.9	0.6	
LPA	Yes	0	-0.078	-10.355	-9.2	0.6	

Satellite floating potential $V_f = -1$ V.

n	Te	T_i	m_{eff}	λ_D	v_d		
$10^{10} m^{-3}$	0.156 eV	0.116 eV	8.3	29.4 mm	7673 m/s		
LP_x	Swarm Bus Included	$ \vec{B} $ μT	V_p V	I_p nA	ϵ_{I_p} %	δ_{I_p} %	
LP1	Yes	0	0.186	-24.033	-81.2	1.8	
LP2	Yes	0	0.186	-23.920	-82.1	1.8	
LPA	Yes	0	0.186	-23.976	-81.6	1.8	
LP1	Yes	0	0.485	-51.631	-60.6	1.3	
LP2	Yes	0	0.485	-50.668	-63.7	1.3	
LPA	Yes	0	0.485	-51.149	-62.1	1.3	
LP1	Yes	0	-0.136	-6.018	-26.1	1.8	
LP2	Yes	0	-0.136	-6.017	-26.1	1.6	
LPA	Yes	0	-0.136	-6.018	-26.1	1.7	
LP1	Yes	0	-0.107	-7.173	-29.3	1.6	
LP2	Yes	0	-0.107	-7.287	-30.1	1.5	
LPA	Yes	0	-0.107	-7.151	-29.7	1.6	
LP1	Yes	0	-0.078	-8.404	-34.5	1.5	
LP2	Yes	0	-0.078	-8.339	-35.6	1.5	
LPA	Yes	0	-0.078	-8.372	-35.0	1.5	

Satellite floating potential $V_f = -2$ V.

n	Te	T_i	m_{eff}	λ_D	v_d		
$10^{10} m^{-3}$	0.156 eV	0.116 eV	8.3	29.4 mm	7673 m/s		
LP_x	Swarm Bus Included	$ \vec{B} $ μT	V_p V	I_p nA	ϵ_{I_p} %	δ_{I_p} %	
LP1	Yes	0	0.186	-7.398	-488.7	4.3	
LP2	Yes	0	0.186	-7.287	-497.6	4.4	
LPA	Yes	0	0.186	-7.342	-493.1	4.3	
LP1	Yes	0	0.485	-15.289	-442.4	2.8	
LP2	Yes	0	0.485	-14.887	-457.1	2.9	
LPA	Yes	0	0.485	-15.088	-449.7	2.8	
LP1	Yes	0	-0.136	-2.535	-199.3	3.6	
LP2	Yes	0	-0.136	-2.462	-208.3	3.9	
LPA	Yes	0	-0.136	-2.498	-203.7	3.7	
LP1	Yes	0	-0.107	-2.866	-223.6	3.4	
LP2	Yes	0	-0.107	-2.784	-233.2	3.8	
LPA	Yes	0	-0.107	-2.825	-228.3	3.6	
LP1	Yes	0	-0.078	-3.242	-248.8	3.4	
LP2	Yes	0	-0.078	-3.125	-261.7	3.8	
LPA	Yes	0	-0.078	-3.183	-255.1	3.6	

n	Te	T_i	m_{eff}	λ_D	v_d		
$10^{10}m^{-3}$	0.156 eV	0.116 eV	8.3	29.4 mm	7673 m/s		
LP_x	Swarm Bus Included	$ \vec{B} $ μT	V_p V	I_p nA	ϵ_{I_p} %	δ_{I_p} %	
LP1	Yes	-37.6	0.235	-43.127	-1.3	1.0	
LP2	Yes	-37.6	0.235	-40.534	-7.8	1.1	
LPA	Yes	-37.6	0.235	-41.830	-4.4	1.0	
LP1	Yes	-37.6	0.534	-76.634	-8.4	0.9	
LP2	Yes	-37.6	0.534	-73.951	-12.3	0.9	
LPA	Yes	-37.6	0.534	-75.293	-10.3	0.9	
LP1	Yes	-37.6	-0.171	-5.644	26.0	1.9	
LP2	Yes	-37.6	-0.171	-4.888	14.6	2.0	
LPA	Yes	-37.6	-0.171	-5.266	20.7	1.9	
LP1	Yes	-37.6	-0.142	-7.029	26.5	1.6	
LP2	Yes	-37.6	-0.142	-6.031	14.3	1.8	
LPA	Yes	-37.6	-0.142	-6.530	20.8	1.7	
LP1	Yes	-37.6	-0.113	-8.597	26.0	1.5	
LP2	Yes	-37.6	-0.113	-7.366	13.6	1.6	
LPA	Yes	-37.6	-0.113	-7.982	20.3	1.6	
LP1	Yes	+37.6	0.236	-40.708	-7.3	0.8	
LP2	Yes	+37.6	0.236	-40.890	-6.8	0.8	
LPA	Yes	+37.6	0.236	-40.799	-7.1	0.8	
LP1	Yes	+37.6	0.535	-74.345	-11.7	0.6	
LP2	Yes	+37.6	0.535	-75.426	-10.1	0.6	
LPA	Yes	+37.6	0.535	-74.886	-10.9	0.6	
LP1	Yes	+37.6	-0.154	-5.242	10.3	1.7	
LP2	Yes	+37.6	-0.154	-5.912	20.5	1.6	
LPA	Yes	+37.6	-0.154	-5.575	15.7	1.7	
LP1	Yes	+37.6	-0.125	-6.518	11.0	1.5	
LP2	Yes	+37.6	-0.125	-7.574	23.4	1.4	
LPA	Yes	+37.6	-0.125	-7.046	17.7	1.4	
LP1	Yes	+37.6	-0.096	-8.078	11.8	1.4	
LP2	Yes	+37.6	-0.096	-9.342	23.7	1.3	
LPA	Yes	+37.6	-0.096	-8.710	18.2	1.3	

Table B.24: Electron linear and retardation currents calculated from simulations for configuration cases considered. ϵ_{I_p} is the relative error in the calculated current from simulations compared to predicted with OML theory Eq. 4.2, while δ_{I_p} is the relative uncertainty. Positive errors indicate overestimation while negative signs refer to an underestimation.

ELECTRON LINEAR AND RETARDATION CURRENTS C11

n	Te	T_i	m_{eff}	λ_D	v_d		
$10^{11} m^{-3}$	0.280 eV	0.121 eV	16.0	12.4 mm	7673 m/s		
LP_x	Swarm Bus Included	$ \vec{B} $ μT	V_p V	I_p nA	ϵ_{I_p} %	δ_{I_p} %	
LP1	No	0	-0.290	-86.9	2.9	0.3	
LP1	No	0	0.010	-274.3	12.2	0.2	
LP1	No	0	-0.469	-41.7	1.2	0.4	
LP1	No	0	-0.440	-47.1	1.5	0.3	
LP1	No	0	-0.411	-53.2	1.7	0.3	
LP1	No	37.6	-0.285	-88.4	2.7	0.3	
LP1	No	37.6	0.015	-274.4	3.8	0.1	
LP1	No	37.6	-0.467	-42.1	1.4	0.3	
LP1	No	37.6	-0.438	-47.7	1.8	0.3	
LP1	No	37.6	-0.409	-53.7	1.9	0.3	
LP1	Yes	0	-0.291	-73.9	-10.7	1.1	
LP2	Yes	0	-0.291	-75.1	-9.0	1.1	
LPA	Yes	0	-0.291	-74.5	-9.8	1.1	
LP1	Yes	0	0.008	-239.1	-4.8	0.6	
LP2	Yes	0	0.008	-237.9	-5.3	0.6	
LPA	Yes	0	0.008	-238.5	-5.1	0.6	
LP1	Yes	0	-0.467	-35.1	-15.3	1.4	
LP2	Yes	0	-0.467	-35.6	-13.7	1.4	
LPA	Yes	0	-0.467	-35.3	-14.5	1.4	
LP1	Yes	0	-0.438	-40.2	-13.6	1.3	
LP2	Yes	0	-0.438	-40.2	-13.6	1.4	
LPA	Yes	0	-0.438	-40.2	-13.6	1.3	
LP1	Yes	0	-0.410	-44.6	-14.8	1.3	
LP2	Yes	0	-0.410	-4.0	-11.2	1.3	
LPA	Yes	0	-0.410	-45.3	-13.0	1.3	

n	Te	T_i	m_{eff}	λ_D	v_d	
$10^{11} m^{-3}$	0.280 eV	0.121 eV	16.0	12.4 mm	7673 m/s	
LP_x	Swarm Bus Included	$ \vec{B} $ μT	V_p V	I_p nA	ϵ_{I_p} %	δ_{I_p} %
LP1	Yes	-37.6	-0.213	-104.607	21.5	1.7
LP2	Yes	-37.6	-0.213	-96.506	14.9	1.7
LPA	Yes	-37.6	-0.213	-100.557	18.3	1.7
LP1	Yes	-37.6	0.086	-313.017	19.6	0.9
LP2	Yes	-37.6	0.086	-294.718	14.6	0.9
LPA	Yes	-37.6	0.086	-303.868	17.2	0.9
LP1	Yes	-37.6	-0.395	-48.783	18.5	1.9
LP2	Yes	-37.6	-0.395	-44.561	10.7	1.9
LPA	Yes	-37.6	-0.395	-46.672	14.8	1.9
LP1	Yes	-37.6	-0.365	-55.635	19.3	1.8
LP2	Yes	-37.6	-0.365	-50.284	10.7	1.9
LPA	Yes	-37.6	-0.365	-52.960	15.3	1.8
LP1	Yes	-37.6	-0.336	-63.136	20.0	1.6
LP2	Yes	-37.6	-0.336	-57.028	11.4	1.7
LPA	Yes	-37.6	-0.336	-60.082	15.9	1.7
LP1	Yes	+37.6	-0.210	-94.592	12.8	1.4
LP2	Yes	+37.6	-0.210	-101.242	18.5	1.4
LPA	Yes	+37.6	-0.210	-97.917	15.8	1.4
LP1	Yes	+37.6	0.088	-292.430	14.0	0.9
LP2	Yes	+37.6	0.088	-304.611	17.4	0.8
LPA	Yes	+37.6	0.088	-298.520	15.7	0.8
LP1	Yes	+37.6	-0.388	-42.764	5.4	1.7
LP2	Yes	+37.6	-0.388	-46.757	13.5	1.6
LPA	Yes	+37.6	-0.388	-44.760	9.6	1.6
LP1	Yes	+37.6	-0.359	-48.622	6.2	1.6
LP2	Yes	+37.6	-0.359	-54.105	15.7	1.5
LPA	Yes	+37.6	-0.359	-51.363	11.2	1.5
LP1	Yes	+37.6	-0.330	-55.373	7.3	1.7
LP2	Yes	+37.6	-0.330	-60.972	15.8	1.6
LPA	Yes	+37.6	-0.330	-58.172	11.7	1.7

Table B.25: Electron linear and retardation currents calculated from simulations for configuration cases considered. ϵ_{I_p} is the relative error in the calculated current from simulations compared to predicted with OML theory Eq. 4.2, while δ_{I_p} is the relative uncertainty. Positive errors indicate overestimation while negative signs refer to an underestimation.

INFERRED ELECTRON TEMPERATURE

n $10^{10}m^{-3}$	T_e eV	T_i eV	m_{eff} amu	λ_D mm	V_f mV	$ \vec{B} $ μT	Swarm Bus Included	LP_x	ϵ_{T_e} %	δ_{T_e} %
1.00	0.156	0.116	8.3	29.4	-504	0	No	LP1	-3.8	0.5
1.00	0.156	0.116	8.3	29.4	-503	37.6	No	LP1	-1.9	0.7
1.00	0.156	0.116	8.3	29.4	-514	0	Yes	LP1	-1.4	1.0
								LP2	-0.6	1.0
								LPA	-1.0	1.0
1.00	0.156	0.116	8.3	29.4	-1000	0	Yes	LP1	17.1	1.3
								LP2	19.4	1.2
								LPA	18.3	1.2
1.00	0.156	0.116	8.3	29.4	-2000	0	Yes	LP1	43.0	3.9
								LP2	44.6	3.8
								LPA	43.8	3.8
1.00	0.156	0.116	8.3	29.4	-466	-37.6	Yes	LP1	-4.1	1.8
								LP2	0.0	1.6
								LPA	-2.2	1.7
1.00	0.156	0.116	8.3	29.4	-465	+37.6	Yes	LP1	-7.2	1.7
								LP2	-12.4	1.9
								LPA	-10.0	1.8
10.0	0.280	0.121	16.0	12.4	-990	0	No	LP1	-2.7	1.0
10.0	0.280	0.121	16.0	12.4	-985	37.6	No	LP1	-2.3	1.0
10.0	0.280	0.121	16.0	12.4	-990	0	Yes	LP1	3.2	2.0
								LP2	-8.9	2.3
								LPA	-2.8	2.2
10.0	0.280	0.121	16.0	12.4	-913	-37.6	Yes	LP1	-10.8	2.0
								LP2	-7.1	1.9
								LPA	-9.0	2.0
10.0	0.280	0.121	16.0	12.4	-911	+37.6	Yes	LP1	-9.7	2.0
								LP2	-14.4	2.1
								LPA	-12.1	2.1

Table B.26: Relative errors in the inferred electron temperature from probe currents calculated from simulations. The relative errors in the inferred electron temperature calculated from Eq. 4.17, are labeled as ϵ_{T_e} , while δ_{T_e} is the relative uncertainty in the estimated temperature. Positive errors indicate overestimation while negative signs refer to an underestimation. In all cases the drifting plasma speed is equal to the satellite ram velocity, $v_{\perp} = 7673$ m/s.